



University of Kentucky
UKnowledge

Theses and Dissertations--Mechanical
Engineering

Mechanical Engineering

2012

TRANSPORT PHENOMENA ASSOCIATED WITH LIQUID METAL FLOW OVER TOPOGRAPHICALLY MODIFIED SURFACES

WEN LIU

University of Kentucky, liuwenzz@gmail.com

[Right click to open a feedback form in a new tab to let us know how this document benefits you.](#)

Recommended Citation

LIU, WEN, "TRANSPORT PHENOMENA ASSOCIATED WITH LIQUID METAL FLOW OVER TOPOGRAPHICALLY MODIFIED SURFACES" (2012). *Theses and Dissertations--Mechanical Engineering*. 16.
https://uknowledge.uky.edu/me_etds/16

This Doctoral Dissertation is brought to you for free and open access by the Mechanical Engineering at UKnowledge. It has been accepted for inclusion in Theses and Dissertations--Mechanical Engineering by an authorized administrator of UKnowledge. For more information, please contact UKnowledge@lsv.uky.edu.

STUDENT AGREEMENT:

I represent that my thesis or dissertation and abstract are my original work. Proper attribution has been given to all outside sources. I understand that I am solely responsible for obtaining any needed copyright permissions. I have obtained and attached hereto needed written permission statements(s) from the owner(s) of each third-party copyrighted matter to be included in my work, allowing electronic distribution (if such use is not permitted by the fair use doctrine).

I hereby grant to The University of Kentucky and its agents the non-exclusive license to archive and make accessible my work in whole or in part in all forms of media, now or hereafter known. I agree that the document mentioned above may be made available immediately for worldwide access unless a preapproved embargo applies.

I retain all other ownership rights to the copyright of my work. I also retain the right to use in future works (such as articles or books) all or part of my work. I understand that I am free to register the copyright to my work.

REVIEW, APPROVAL AND ACCEPTANCE

The document mentioned above has been reviewed and accepted by the student's advisor, on behalf of the advisory committee, and by the Director of Graduate Studies (DGS), on behalf of the program; we verify that this is the final, approved version of the student's dissertation including all changes required by the advisory committee. The undersigned agree to abide by the statements above.

WEN LIU, Student

Dr. Dusan P. Sekulic, Major Professor

Dr. James M. McDonough, Director of Graduate Studies

TRANSPORT PHENOMENA ASSOCIATED WITH LIQUID METAL FLOW OVER
TOPOGRAPHICALLY MODIFIED SURFACES

DISSERTATION

A dissertation submitted in partial fulfillment of the
requirements for the degree of Doctor of Philosophy in the
College of Engineering
at the University of Kentucky

By
Wen Liu

Lexington, Kentucky

Director: Dr. Dusan P. Sekulic, Professor of University of Kentucky

Lexington, Kentucky

2012

Copyright © Wen Liu 2012

ABSTRACT OF DISSERTATION

TRANSPORT PHENOMENA ASSOCIATED WITH LIQUID METAL FLOW OVER TOPOGRAPHICALLY MODIFIED SURFACE

Brazing and soldering, as advanced manufacturing processes, are of significant importance to industrial applications. It is widely accepted that joining by brazing or soldering is possible if a liquid metal wets the solids to be joined. Wetting, hence spreading and capillary action of liquid metal (often called filler) is of significant importance. Good wetting is required to distribute liquid metal over/between the substrate materials for a successful bonding.

Topographically altered surfaces have been used to exploit novel wetting phenomena and associated capillary actions, such as imbibitions (a penetration of a liquid front over/through a rough, patterned surface). Modification of surface roughness may be considered as a venue to tune and control the spreading behavior of the liquids. Modeling of spreading of liquids on rough surface, in particular liquid metals is to a large extent unexplored and constitutes a cutting edge research topic.

In this dissertation the imbibitions of liquid metal has been considered as pertained to the metal bonding processes involving brazing and soldering fillers. First, a detailed review of fundamentals and the recent progress in studies of non-reactive and reactive wetting/capillary phenomena has been provided. An imbibition phenomenon has been experimentally achieved for organic liquids and molten metals during spreading over topographically modified intermetallic surfaces. It is demonstrated that the kinetics of such an imbibition over rough surfaces follows the Washburn-type law during the main spreading stage. The Washburn-type theoretical modeling framework has been established for both isotropic and anisotropic non-reactive imbibition of liquid systems over rough surfaces. The rough surface domain is considered as a porous-like medium and the associated surface topographical features have been characterized either theoretically or experimentally through corresponding permeability, porosity and tortuosity. Phenomenological records and empirical data have been utilized to verify the constructed model. The agreement between predictions and empirical evidence appears to be good. Moreover, a reactive wetting in a high temperature brazing process has been studied for both polished and rough surfaces. A linear relation between the propagating

triple line and the time has been established, with spreading dominated by a strong chemical reaction.

KEYWORDS: Metal Joining, Wetting and Capillarity,
Rough Surface, Imbibition, Modeling

Wen Liu

Nov, 27th, 2012

TRANSPORT PHENOMENA ASSOCIATED WITH LIQUID METAL FLOW
OVER TOPOGRAPHICALLY MODIFIED SURFACES

By

Wen Liu

Dr. Dusan P. Sekulic

Director of Dissertation

Dr. James M. McDonough

Director of Graduate Studies

Nov, 27th, 2012

DEDICATION
I DEDICATE MY DISSERTATION TO MY PARENTS AND MY WIFE

ACKNOWLEDGEMENTS

I would first like to sincerely thank my advisor Professor Dusan P. Sekulic for his continuous guidance and support throughout my graduate study. It is because of his encouragement that I could successfully complete my research work.

Additional thanks to my committee members and outside examiner: Drs. Kozo Saito, Y-T Cheng, Yuming Zhang and Christine Trinkle, Zhongwei Shen. I would like to thank all of you for your time and advice during the defense process.

I am also grateful to Professor Yulong Li from Key Lab of Robot & Welding Automation of Jiangxi Province, Nanchang University (China) for his valuable discussion and help in the field of materials science.

In addition, I would like to thank all the Faculty members and the staff of the Department of Mechanical Engineering and the Institute for Sustainable Manufacturing for their continued support and cooperation. I would like to thank my research team members for their continued support.

Last but not the least, I want to express my deep gratitude to my parents, Jiaxin Liu and Yuping Liu for their unconditional love and support. Special thanks to my wife, Yizi Yang, without whom I would not have accomplished my goals in life.

TABLE OF CONTENTS

ACKNOWLEDGEMENTS	iii
LIST OF TABLES	vi
LIST OF FIGURES	vii
CHAPTER 1: INTRODUCTION	1
1.1 Background Overview.....	1
1.2 Research Objectives	3
1.3 Organization of the Dissertation	4
CHAPTER 2: REVIEW OF THE RELATED EXISTING WORK.....	7
2.1 Wetting.....	7
2.1.1 Surface Tension	8
2.1.2 Wetting of a Smooth Surface.....	9
2.1.3 Kinetics of Wetting on a Smooth Surface	11
2.1.4 Wetting of a Rough Surface	14
2.1.4.1 Wenzel’s Model	14
2.1.4.2 The Cassie-Baxter Model.....	17
2.1.4.3 Composite Rough Surfaces	18
2.2 Capillarity.....	23
2.2.1 Capillary Length and Menisci	24
2.2.2 Capillary Flow through a Single Cylindrical Tube	26
2.2.3 Capillary Flow through a Single Open Surface Groove.....	30
2.2.4 Capillary Flow over Rough Surfaces.....	33
2.3 Flow through Porous Media.....	36
2.4 Wetting and Capillarity in Soldering and Brazing.....	38
2.4.1 Soldering and Brazing	38
2.4.2 Importance of good wetting and capillarity.....	40
2.4.3 Reactive Wetting	42
2.4.3.1 Brief Introduction of Reactive Wetting.....	42
2.4.3.2 Kinetics of Reactive Wetting	45
CHAPTER 3: CAPILLARY RISE OF LIQUIDS OVER A MICROSTRUCTURED SOLID SURFACE.....	48
3.1 Overview	48
3.2 Materials and Experimental Procedures.....	49
3.2.1 Fabrication of the IMC Surface	49
3.2.2 Surface Characterization.....	53
3.2.3 Properties of Liquids, Contact Angle Measurements.....	59
3.2.4 Capillary Rise of Liquids through the IMC Rough Surface: Experimental Data	62
3.3 Theoretical Model	65
3.4 Results and Discussion.....	74
3.5 Summary	78
CHAPTER 4: CAPILLARY DRIVEN MOLTEN METAL FLOW OVER TOPOGRAPHICALLY COMPLEX SUBSTRATES.....	80
4.1 Overview	80
4.2 Problem Formulation.....	81

4.3	Materials and Experimental Procedures.....	86
4.4	Experimental Results and Phenomenological Observations.....	91
4.5	Characterization of the Surface Topography.....	95
4.6	Building the Theoretical Model.....	98
4.7	Results and Discussion.....	104
4.8	Summary.....	107
CHAPTER 5: PREFERENTIAL SPREADING OF MOLTEN METAL OVER AN ANISOTROPICALLY MICROSTRUCTURED SURFACE.....		109
5.1	Overview.....	109
5.2	Experimental Observation and Results.....	110
5.2.1	Preferential Spreading (Directional Spreading).....	111
5.2.2	Surface Characterization.....	114
5.2.3	Spreading Kinetics.....	119
5.3	Theoretical Analysis.....	122
5.4	Results and Discussion.....	128
5.5	Summary.....	131
CHAPTER 6: EXPERIMENTAL STUDY OF REACTIVE WETTING OF AgCgTi FILLER METAL ON TOPOGRAPHICALLY MODIFIED TiAl – BASED ALLOY SUBSTRATES.....		133
6.1	Overview.....	133
6.2	Materials and Experimental Procedure.....	134
6.2.1	Materials Selection.....	134
6.2.2	Experimental Procedures.....	135
6.3	Results and Discussions.....	139
6.3.1	Phenomenological Observation and Experimental Data.....	139
6.3.2	Microstructure Analysis.....	146
6.3.3	Phenomenological Analysis of Wetting Kinetics.....	148
6.4	Summary.....	151
CHAPTER 7: CONCLUSIONS AND FUTURE WORK.....		153
7.1	Main Conclusions.....	153
7.2	Future Work.....	159
APPENDICES.....		161
Appendix A.....		161
Appendix B.....		163
Appendix C.....		165
Appendix D.....		167
Appendix E.....		168
Appendix F.....		171
Appendix G.....		174
Appendix H.....		176
Appendix I.....		184
REFERENCES.....		185
VITA.....		193

LIST OF TABLES

Table 2.1: Contact angle values and associated solderability/brazability (Data adopted from (Moser et al., 2008)).....	42
Table 3.1: Fabrication details of IMC rough surfaces	51
Table 3.2: Data of roughness measurements for an IMC0 substrate	55
Table 3.3: Properties of liquids (Data collected from (Landesberg, 2004))	59
Table 4.1: Substrate/solder sample sizes	87
Table 4.2: Physical properties and porous surface characteristics (Data are adopted from (Yost et al., 1997; Howie and Hondoros, 1982; White, 1971; Ejima et al., 1990))	103
Table 4.3: Average Relative Error of Triple Line Location Prediction	105
Table 5.1: The initial size of the source material, the final spreading radius and the ratios of the final radii x / y	130
Table 5.2: Selected filling factors, a prediction range and associated average relative errors of the prediction.....	130

LIST OF FIGURES

Figure 2.1: A molecule in a “happy” state and an “unhappy” molecule at the surface. The latter is missing a half of its cohesive interaction energy, modified from (de Gennes et al., 2004).	8
Figure 2.2: A droplet over a horizontal smooth surface in equilibrium: (a), (b) indicate the case of partial wetting, (c) represents the case of complete wetting with $\theta_E = 0$	10
Figure 2.3: A small droplet over a horizontal smooth surface in equilibrium.....	11
Figure 2.4: (a) A small droplet spreading on a substrate (Non-reactive case). (b) The domain within the red dotted block in (a) indicating the edge domain of the droplet	13
Figure 2.5: (a) A small droplet wetting on a physically rough substrate with an apparent contact angle θ^* . (b) The displacement within the domain of the right edge in (a).	16
Figure 2.6: A small droplet wetting on a chemically heterogeneous substrate composed of different material characterized with the area fractions f_1 and f_2	17
Figure 2.7: A droplet over a horizontal rough surface in equilibrium: (a) Wenzel’s model and (b) the penetration case (Cassie-Baxter model)	19
Figure 2.8: A droplet over a horizontal rough surface in equilibrium: (a) Wenzel’s model and (b) the air-pockets case (Cassie-Baxter model)	21
Figure 2.9: Apparent contact angle as a function of Young’s contact angle (via their cosines) for a liquid on a rough surface (Figure adopted from (de Gennes et al., 2004)).....	22
Figure 2.10: Experimental data showing the apparent contact angle as a function of Young’s contact angle (measured on a planar surface) for various substrates with a random roughness that is increasing from left to right (Figures adopted from (Shibuichi et al., 1996; de Gennes et al., 2004)).....	23
Figure 2.11: A small droplet with $r \ll \kappa^{-1}$ (left) and a large droplet with $r \gg \kappa^{-1}$ (right) over a horizontal smooth surface in equilibrium	25
Figure 2.12: Meniscus of a liquid facing a solid vertical wall associated with “mostly wetting” condition.....	26
Figure 2.13: A liquid flowing through a cylindrical capillary tube (Washburn, 1921)...	27
Figure 2.14: (a) capillary flow through a single open surface groove, (b) a cross sectional view of the open triangular groove.	32
Figure 2.15: A cross sectional metallographic view of good wetting case in (a) soldering of a chip resistor to a PWB (image adopted from (AWS Brazing Handbook, 1991)), (b) a good brazing joint (courtesy from Brazing Research Lab at the University of Kentucky)	41
Figure 2.16: Dissolutive wetting: (a) wetting configuration (b) details at the triple line .	43
Figure 2.17: Possible configurations of a reacting system at triple line when equilibrium contact angle is reached (a) stable configuration and (b) metastable configuration	44
Figure 3.1: (a) SEM image of the fabricated IMC0 surface showing its topography. (b) SEM images of a cross section view of an IMC0 surface at two different random locations.	54

Figure 3.2: Characterization of surface roughness by Zygo optical profilometer. The roughness profile (right) associated with the scan line (left) is indicated.....	55
Figure 3.3: (a) Surface topography presented by 3D AFM scanning image of the fabricated IMC surface. Spatial scale bar is given on the right. (b) Area ratios between porous or solid domains and the total scanned area at various height levels.	57
Figure 3.4: (a) Histogram for the height distribution of IMC topographic features. (b) A randomly selected surface profile showing cross section of a groove formed between Cu_6Sn_5 grains	58
Figure 3.5: Measurement of apparent advancing contact angle of liquids on the rough IMC surface with a magnification of $40\times$ (A bar of $50\ \mu m$ is indicated in the figure).....	61
Figure 3.6. Experimental configuration for capillary rise upward an IMC rough surface	63
Figure 3.7: Image sequence of capillary rise fronts of Tetradecane wicking over an IMC surface (0 – 200 seconds).....	64
Figure 3.8: Model of the macro configuration of capillary wicking upward a rough IMC surface	66
Figure 3.9: Geometric Details of Cross sections of V- Groove	69
Figure 3.10: Kinetics data of liquids presented in z vs. $t^{1/2}$ coordinate.....	75
Figure 3.11: Kinetics data of liquids in presented with a scaled time $(\sigma t/\mu)^{1/2}$	76
Figure 3.12: Average relative errors of theoretical prediction with various filling conditions	77
Figure 4.1: Surface topography of a $Cu_6Sn_5/Cu_3Sn/Cu$ (IMC-1) substrate	82
Figure 4.2: Instantaneous frames extracted from a real time in situ monitoring of Pb-Sn eutectic spreading over IMC1 ($Cu_6Sn_5/Cu_3Sn/Cu$) (Images associated with Test-2 in Table 4.1)	84
Figure 4.3: (a) SEM image at a location of the spreading front; (b) SEM image illustrates cross section of a sample after the test.....	85
Figure 4.4: Heating cycle that consists of a ramp up, dwell and quench for spreading tests (a) for Test-1 and 2 for 63Sn-37Pb solder (b) Test-3 and 4 for 80Sn-20Pb solder. (Note that heating cycle in Figure 4.4 (a) is also used for tests studied in Chapter 5)	88
Figure 4.5: (a) Configuration of the hotstage microscopy system, (b) hotstage microscopy setup in the Brazing Research Laboratory of the University of Kentucky	89
Figure 4.6: Time t vs. spreading front for Test-1, 2, 3 and 4.....	92
Figure 4.7: (a) Real surface topography of IMC1. (b) A simplified topography: a collection of regular hexagonal elements. (c) Cross-sectional view of IMC surface with marking an IMC layer. (d) Cross-sectional view of the simplified topography.	96
Figure 4.8: A regular hexagonal element which is used to simplify the IMC surface.	96
Figure 4.9. (a) Simplified surface topography of IMC1: (a) A collection of joined regular hexagonal elements. (b) Details of the topography. (c) Cross sectional view of an open triangular groove. (d) Details of the geometric configuration of a single merging zone.....	97
Figure 4.10: The control volume within the domain of a two dimensional porous medium	100

Figure 4.11: Prediction of the triple line location for Tests 1 and 2	104
Figure 4.12: Prediction of the triple line location for Tests 3 and 4	105
Figure 5.1: (a) (b) and (c): SEM images showing topographical features of an IMC1, IMC2 and IMC3 substrate respectively; (d): a final circle pattern for eutectic Pb-Sn solder spreading on an IMC1 substrate; (e) and (f): elliptical patterns for eutectic Pb-Sn solder spreading on an IMC2 and IMC3 substrate, respectively	112
Figure 5.2: Ratios of the length of long axis to short axis for IMC1, IMC2 and IMC3 substrates.....	113
Figure 5.3: (a) The final ellipse-like spreading pattern with x (preferential) and y axis, (b) Source material residue and the parallel traces of grains associated with the x axis, (c) Small amount of re-solidified solder material present in grooves between parallel traces of grains after spreading. Note x and y directions are consistent in (a) (b) and (c).	115
Figure 5.4: (a) Parallel traces of the larger grains showing peaks and valleys, (b) Chains of peaks identified from a view along the parallel traces of larger grains, (c) No chains of peaks noticed from a view along the direction perpendicular to the chain of peaks identified in (b).....	116
Figure 5.5: AFM scanning results indicate the topographical features of (a) IMC3 and (b) IMC2 substrates. (The scanning area is 50×50um)	117
Figure 5.6: (a) SEM image of the surface topography of an IMC1 surface, (b) An image sequence of the Sn-Pb eutectic spreading on IMC1 surface, (c) SEM image of an anisotropic topography featured by the IMC3 surface topography, (d) Image sequence of the Sn-Pb eutectic spreading on IMC3 surface.....	120
Figure 5.7: Kinetics of spreading on IMC1, IMC2 and IMC3 in a log-log scale, respectively.	121
Figure 5.8: Configuration of the model of an open triangular groove with a liquid phase within it (Rye et al., 1996)	124
Figure 5.9: Kinetics data of Sn-Pb alloy spreading on IMC3 substrates at ~486 K featuring two different kinetics power laws and an asymptotic ending.....	129
Figure 6.1: Microstructure of a cross-section of the AgCuTi brazing filler metal, showing a AgCu/Ti/AgCu sandwich structure. (Li et al, 2012).....	136
Figure 6.2: (a) Topographical details of a polished TiAl surface. (b) Topographical details of a rough TiAl surface.	137
Figure 6.3: Heating cycle for spreading tests for AgCuTi – TiAl reactive wetting system	138
Figure 6.4: A sequence of instantaneous frames during AgCuTi braze spreading on the polished TiAl substrate: (a) before melting (b) after the onset of melting (c) after the onset of spreading (d) an advanced period of spreading (e) initial re-solidification (f) complete re-solidification	140
Figure 6.5: A sequence of instantaneous frames during AgCuTi braze spreading on the polished TiAl substrate. Insets represented the same set of events as in Figure 6.4.	140
Figure 6.6: Kinetics data in a logarithmic scale of the triple line for the AgCuTi filler metal spreading on: (a) a polished TiAl substrate, (b) a rough TiAl substrate (from melting through solidification). Note: the temperature associated with the origin of the abscissa is 1043 K (before the onset of melting)	141

Figure 6.7: (a) Top view of a re-solidified AgCuTi filler metal. (b) The line scan analysis of the main elements, distribution across the radial direction of the re-solidified braze Microstructure of the interface of the AgCuTi filler metal brazed on TiAl (c) the cross section within the central domain of the re-solidified filler metal (d) the cross section within the edge domain of the resolidified filler metal. 148

Figure 6.8: (a) solidified AgCu filler sits on the production of chemical reaction at the interface, (b) a wetting configuration for reactive wetting system described in Chapter 2 (Figure 6.6 (b) is extracted from Figure 2.17 (b))..... 150

CHAPTER 1: INTRODUCTION

1.1 Background Overview

Spreading of liquids over solids, i.e., wetting and capillarity phenomena, have been a subject of a long lasting interest (de Gennes, 1985; de Gennes et al., 2004; Bonn et al., 2009). The associated engineering relevance has been related to industrial and natural processes, including: materials joining – e.g., soldering and brazing (AWS Brazing Handbook, 1991; AWS Soldering Handbook, 1999), material deposition – e.g., painting (Patton, 1979) and coating (Marrion, 2004), biological phenomena – e.g., hummingbird tongue and shorebird beak biological functions (Rico-Guevara and Rubega, 2011; Prakash et al., 2008), geology – e.g., molten lava flows (Lezzi and Ventura, 2005) and many others.

More specifically, a low temperature soldering, and a high/ultra-high temperature brazing of metals and nonmetals play a significant role in multitude of applications, including: electronics (commercial, medical and military), automotive, and aerospace industries (AWS Brazing Handbook, 1991). The quality of the bond between materials, in any of those applications created by the soldering/brazing process, depends critically on the wetting/capillary kinetics of the molten metal filler (molten solder or braze).

The wetting/capillary kinetics during soldering/brazing process has a strong influence on the subsequently formed microstructure of the joint and consequently, on the strength and durability of the bond between joined materials (Pan and Sekulic, 2002; Qian et al., 2003; Saiz et al., 2000). A quantitative prediction of capillary action and wetting kinetics of a molten metal is always desired for designing a bonding process. For example, brazing of dissimilar metals such as stainless steel and aluminum alloy requires

tight scheduling of the process, because wetting and the associated capillary action of a molten Al-Si filler over aluminum alloy is more pronounced than over stainless steel. The processing time is limited by the need to reduce the time available for the formation of brittle Al-Fe intermetallic phases (Roulin et al., 1999; Liu et al., 2005). Often, the inability to predict and control spreading kinetics is mitigated by adapting the mechanical design to the needs of joining (Shapiro and Sekulic, 2008). Such is the case of an excessive spreading of Ni-Mo fillers over Molybdenum and/or porous tungsten (Busbahr and Sekulic, 2009). In soldering case, the formation of the intermetallic layer at the interface, which plays an important role in bonding integrity, greatly depends on the dwell time at the peak soldering temperature (Suh et al., 2008). Moreover, lead-free solders feature a poor spreading and the kinetics is further complicated by strong interface reactions (Zhao et al., 2009). A satisfactory control of liquid metal wetting as well as the associated modeling needs to be explored further.

In recent decades, owing to the extensive development and use of micro/nano technology, thus due to the development of refined methods for setting very well-controlled micro- or nanostructures on solid substrates, wetting and capillarity have been exploited so to promote novel material properties, such as spontaneous filmification, superhydrophobicity, superoleophobicity, and interfacial slip. These phenomena require well controlled surface roughness (tuning surface topography) in such a way that could not be achieved before (Quere, 2008). Such novel properties have already brought a number of potential technical improvements in few fields, i.e., superoleophobic surfaces for oil transportation (Tuteja et al., 2007), superhydrophobic paper and textiles (Ogihara et al., 2012; Wang et al., 2011), and, for example, a capillary force induced whitening

method (Chandra et al., 2009). Few studies, however, have been reported for materials joining, say soldering and brazing, in particular at the elevated temperatures, and the existing models of wetting/capillary spreading of liquid metals may fail to predict experimental results in a satisfactory manner.

The research interest in this dissertation therefore would be directly related to exploring, explaining and modeling wetting or/and capillary phenomena involving interface reaction and surface topography modifications. The focus is on an ability to control the spreading/imbibition of the liquid phase (molten metal or in the benchmark tests the organic liquids) during soldering or brazing processes at various temperature levels. The major difficulties in modeling attempts will include: (i) the presence of diffusion/chemical reactions between molten solder/braze and the substrates, (ii) the adequate characterization of the spreading surface topography, and (iii) modeling of the physical mechanism by which the triple line propagates over topographically altered and/or reactive substrate.

1.2 Research Objectives

The main objectives of this dissertation are to (i) explain and model a liquid metal wetting/capillary phenomenon – the liquid phase imbibition induced by surface tension over topographical alterations of an intermetallic substrate, (ii) study experimentally isotropic/anisotropic imbibition of soldering materials over rough intermetallic surfaces at elevated temperatures but without chemical reactions, and (iii) explore a possible impact of surface alterations on a high temperature brazing with a strong chemical reaction.

The following objectives were accomplished:

- Providing the empirical evidence and a fundamental physical understanding of wetting/capillary phenomena of liquids on rough intermetallic surfaces: isotropic and preferential imbibitions (the case of low temperature soldering).
- Establishing theoretical models that describe the planar, radial and anisotropic imbibition of molten solders and organic liquids over intermetallic surfaces featuring various types of roughness composed of microsize grains.
- Establishing theoretical and experimental methods for characterizing different types of surface roughness in order to support the modeling.
- Establishing experimentally what kind of impact may topographical alterations have in a chemical reaction-dominated reactive wetting case (the case of high temperature brazing).

1.3 Organization of the Dissertation

The following chapter, Chapter 2, provides a detailed review of the fundamentals and recent progress in study of non-reactive wetting/capillary phenomena on both smooth and rough surfaces, and a brief introduction of soldering/brazing involving reactive wetting.

The main contribution of this dissertation is summarized in Chapters 3, 4, 5 and 6. Chapter 3 offers a study of a non-reactive case of a capillary raise of a set of organic liquids upwards a microstructured intermetallic surface in a planar fashion and at room temperature. This set of experiments has been performed as benchmarking theoretical model beyond the materials parameters studied in Chapter 4 (i.e., a verification of the

validity of the Washburn-type model of spreading to be subsequently studied). The intermetallic substrate is prepared following the procedure used for subsequent experiments. Details about experiments, theoretical modeling process and the validation of the Washburn-type model are included.

Chapter 4 focuses on phenomenological observation and modeling of a radial imbibition of molten solders on an intermetallic surface with a roughness composed of uniformly distributed grains. A Washburn-type kinetics has been registered empirically and theoretically. The chemical reaction has been minimized by using an intermetallic substrate in an attempt to simplify the problem.

In light of the Chapter 4, Chapter 5 demonstrates a non-reactive preferential spreading of a molten solder over an anisotropically microstructured intermetallic substrate. In addition to an experimental examination of the correlation between the preferential spreading direction and the anisotropic features of the intermetallic grains, a theoretical model that describes the anisotropic imbibition has also been established. It is indicated that the preferential imbibition could be tuned by preferential formation of the intermetallic grains.

In Chapter 6 a reactive wetting in a high temperature brazing process has been studied for both polished and rough surfaces. A linear relation between the propagating triple line and the time has been registered and the wetting is therefore proved to be dominated by a strong chemical reaction. In such a case, it is demonstrated that the topographical alterations of the substrates have a minimal impact on wetting kinetics.

Conclusions and recommendations for the future research work have been addressed in the last chapter of this dissertation – Chapter seven.

The main body of the dissertation text is followed by a series of appendices. The material distributed in appendices, Appendix A - I, includes description of capillary length, determination of Bond number, criteria for no chemical reaction between Cu-Sn IMC and Pb-Sn solder, details for measurements of IMC grain features, description of parameters associated with porous media theory, raw kinetics data for all spreading tests studied in this dissertation and symbolism.

CHAPTER 2: REVIEW OF THE RELATED EXISTING WORK

This chapter offers a general overview of relevant research work in connection with the scope of this dissertation. The review involves the broader fields of wetting phenomena and capillarity, as well as their specifics through engineering significance for liquid metals spreading in brazing and soldering. The content is split into four sections. The first section (Section 2.1) describes fundamentals of a wetting phenomenon and modeling of wetting kinetics for both smooth and rough surfaces. Subsequently, in addition to basic concepts about capillarity, Section 2.2 provides information on the kinetics of a liquid flowing in a single capillary channel and an open surface groove. A review of the capillary phenomena involving liquids spreading over various rough surfaces and the associated kinetics is included. A brief introduction of the fundamentals of the theory of flow through porous media is given in the following section, Section 2.3. Finally, Section 2.4 introduces two practical manufacturing processes: soldering and brazing, and then the reason why a good wetting/capillarity is of importance and desired. Moreover, a consideration of reactive wetting is introduced by offering a review of basic types of reactive wetting cases and the models which describe them.

2.1 Wetting

Wetting refers to interface phenomena of how a liquid maintains contact with a solid surface (in the scope of this dissertation). Surface chemistry (Durian and Franck, 1987a) and surface forces such as van der Waals or electrostatic forces (de Gennes, 1985) play key roles for determining whether or not a liquid will wet a given surface (Durian and Franck, 1987b; Bonn et al., 2009; Vrij, 1966). There are multiple studies based on a

search involving molecular/atomic level beyond Yount’s equation (Webb et al, 2002; Webb and Grest, 2005; Benhassine et al, 2010). In addition, in recent decades, new concepts, such as patterned surfaces and surfactants, are being introduced to influence both the statics and dynamics of wetting. In general, Wetting phenomena are an area where chemistry, physics and engineering intersect, and are of key importance to numerous applications, i.e., manufacturing, chemical industry, glass, food, soil science, biology and so on (de Gennes, 1985; de Gennes et al., 2004; Bonn et al., 2009; Nalwa, 2001)

2.1.1 Surface Tension

A solid or liquid is considered as a condensed state in which molecules attract each other (Bonn et al. 2009). A molecule in the midst of a solid or liquid interacts with all its neighbors around and it is in a “happy ☺” state (de Gennes et al., 2004). On the other hand, a molecule that locates on the surface loses half its cohesive interactions and becomes “unhappy ☹”, as indicated in Figure 2.1.

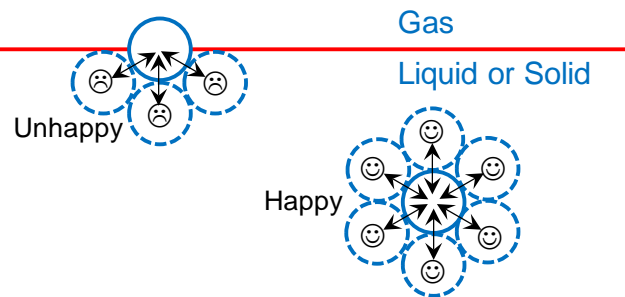


Figure 2.1: A molecule in a “happy” state and an “unhappy” molecule at the surface. The latter is missing a half of its cohesive interaction energy, modified from (de Gennes et al., 2004).

When moved to the surface, a solid or liquid molecule is in an unfavorable energy state. If the cohesion energy per molecule is U inside the liquid, a molecule sitting at the

surface has the cohesion energy of approximately $U / 2$ (Rowlingson and Widom, 1982). The surface tension is a direct measure of such an energy difference per unit surface area. For the liquids with molecular interactions of the van der Waals type, the magnitude of the quantity of the surface tension is approximated as follows (Rowlington and Widom, 1982)

$$\gamma \cong k(T) / (2a^2) \quad (2.1)$$

where a is the approximated characteristic size of a molecule, and $k(T)$ represents the thermal energy. For a silicone oil at room temperature ($\sim 25^\circ\text{C}$), $k(T)$ is about $1/40$ eV and the molecule size is in the order of 10^{-10} m, therefore the surface tension of a silicone oil is estimated to be 20 mN/m (de Gennes et al., 2004). And for mercury, which is a strongly cohesive liquid metal, the surface tension is about 500 mN/m (Bircumshaw, 1931; Kernaghan, 1931). A liquid spontaneously minimizes its surface energy and that explains that liquids adjust their shape in attempt to expose the smallest possible surface area, i.e., a spherical water drop (Bonn et al., 2009).

2.1.2 Wetting of a Smooth Surface

When a small liquid droplet is positioned in contact with a flat solid non-reactive surface, two distinct equilibrium states may be noticed: partial wetting, or complete wetting. In cases of partial wetting, the wetted part of the solid substrate is delimited by a certain contact line that is usually called triple line, where three phases meet each other. The angle formed at the contact line, between the solid surface and the tangent to the

liquid surface at the line of contact with the solid, is known as a contact angle which is usually designated as θ (θ_E for an equilibrium state) as indicated in Figure. 2.2.

Figure 2.2 offers three conditions for a solid smooth surface wetted by a liquid (de Gennes, 1985). Figure 2.2 (a) shows a “mostly non-wetting” situation in which the contact angle is larger than 90° . Figure 2.2 (b) gives an example of “mostly wetting” as the contact angle is smaller than 90° but larger than 0° . Figure 2.2 (c) indicates an extreme case for the contact angle equal to 0° , which is called complete wetting. Note that the cases shown in Figure 2.2 (a) and (b) are generally called partial wetting comparing to a complete wetting. For water, Figure 2.2 (a) and (b) are referred to as hydrophobic and hydrophilic, respectively. Note that the case with the contact angle larger than 150° is registered as superhydrophobic state, which is also known as lotus effect (Bonn et al., 2009; Quere, 2008).

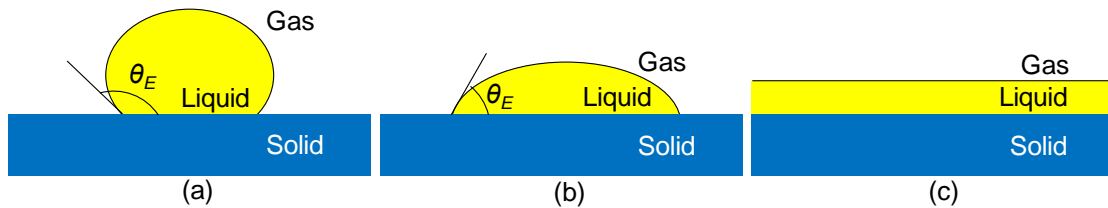


Figure 2.2: A droplet over a horizontal smooth surface in equilibrium: (a), (b) indicate the case of partial wetting, (c) represents the case of complete wetting with $\theta_E = 0$.

If a droplet on a solid smooth surface reaches its equilibrium as shown in Figure 2.3, which means the energy must be stationary with respect to any infinitesimal shift of the triple line position (de Gennes, 1985), the relation between the surface tensions of

three phases and equilibrium contact angle can be described as Young's Equation (Young, 1805)

$$\gamma_{SG} - \gamma_{SL} - \gamma_{LG} \cos \theta_E = 0 \quad (2.2)$$

where γ_{SG} represents the surface tension for solid-gas interface, γ_{SL} is the surface tension for solid-liquid interface and γ_{LG} is the surface tension for liquid-gas interface (γ is used in the later text as a short form and phases will be identifiable from the context). θ_E is contact angle in the equilibrium. Note that the surface tension is also determined by the chemical composition of each phase, which will be discussed in Section 2.1.4.

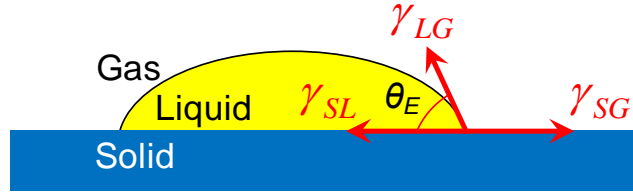


Figure 2.3: A small droplet over a horizontal smooth surface in equilibrium

2.1.3 Kinetics of Wetting on a Smooth Surface

If a droplet wets the substrate, thus experiences spreading, the wetting kinetics is considered as an important issue. Note that in the scope of this dissertation, wetting kinetics is defined as the relation between the triple line advancement and associated elapsed time. As indicated in Figure 2.4 (a), a droplet spreads on a solid substrate and the spreading radius increases as a function of time. Such a time evolution of the triple line movement (or spreading radius r) was studied by L. H. Tanner in 1979 and a theoretical model was established (Tanner, 1979) based on the earlier contributions for the study of

moving contact liquid-solid lines (Huh and Scriven, 1971; Lopez et al., 1976; Dussan and Davis, 1974; Dussan, 1976).

With the edge configuration illustrated in Figure 2.4 (b), Navier-Stokes equations for slow viscous flow in two dimensions can be written as Equation (2.3) based on (Tanner, 1979),

$$\frac{\partial P}{\partial x} = \mu \left(\frac{\partial^2 u}{\partial x^2} + \frac{\partial^2 u}{\partial y^2} \right) \quad \frac{\partial P}{\partial y} = \mu \left(\frac{\partial^2 v}{\partial x^2} + \frac{\partial^2 v}{\partial y^2} \right) \quad (2.3)$$

As dy_s / dx is sufficiently small, the spreading can be considered as one-dimensional. The pressure gradient is provided by the surface tension associated with surface curvature of the droplet. With an assumption that the front of the edge advances with a velocity U with a constant profile shape, a relation between U and contact angle can be obtained from Equation (2.3) and expressed as follows (Tanner, 1979)

$$U \sim \frac{\gamma}{\mu} \left(\frac{dy_s}{dx} \right)^3 \sim \frac{\gamma}{\mu} \theta^3 \quad (2.4)$$

Note that the approximation $dy_s / dx = \tan \theta \approx \theta$ is applied when θ is small enough.

The same expression can also be derived by balancing the viscous dissipation and surface tension associated with the droplet spreading (Biance, 2004). The surface tension driving force of the droplet spreading can be expressed as $F_\gamma = (1/2)\gamma\theta^2$, (Biance, 2004). The retarding force which is the viscous force can be approximated as $F_\mu \sim (\mu/\gamma)U$,

(Biance, 2004). Therefore balancing those two forces could lead to the same relation between U and contact angle as indicated in Equation (2.4), (Hui, 2005).

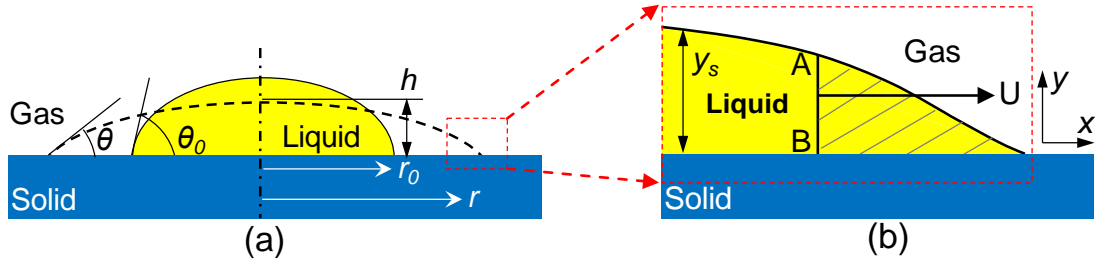


Figure 2.4: (a) A small droplet spreading on a substrate (Non-reactive case). (b) The domain within the red dotted block in (a) indicating the edge domain of the droplet

Supposing the droplet can be considered as a sphere cap with a volume of Ω , a relation between spreading radius r and spreading time t would be obtained as follows

$$r^{10} \sim \frac{\gamma}{\mu} \Omega^3 t \quad (2.5)$$

The tenth power law relation between the spreading radius and associated time (also known as Tanner's law) is registered for a droplet spreading on a smooth substrate without considering a presence of any types of reactions.

It should be noticed that for a droplet whose base radius is much larger than the associated capillary length, in which case the gravity is dominated and must be considered, the wetting kinetics can be described by a theoretically established seventh or eighth power law relation (Dodge, 1998; Brochard-Wyart et al., 1991). Recently Zhao and Sekulic (Zhao and Sekulic, 2008) found that Tanner's law can be applied to the

wetting kinetics of a molten Al-Si alloy (AA4343) on an aluminum alloy (AA3003) substrate at elevated temperatures.

2.1.4 Wetting of a Rough Surface

The wetting behavior of an ideal smooth solid surface is controlled by its chemical composition which the surface tension depends on (see Young's equation). But real solid surfaces are rough and associated wettability is affected by such a surface roughness as well. In this section, we first present the basic wetting models for the surfaces that are roughened/textured either physically (Wenzel's model (Wenzel, 1936)) or chemically (Cassie-Baxter model (Cassie and Baxter, 1944)). Next, we will show how those two models can be combined in a hybrid case (a composite rough surface).

2.1.4.1 Wenzel's Model

One of the earliest attempts to understand the influence of roughness on wetting behavior is due to R. N. Wenzel (Wenzel, 1936). In Wenzel's study it is assumed that (i) the local contact angle is given by Young's equation (Equation 2.2), (ii) the surface is physically rough but chemically homogeneous, and (iii) the roughness scale is much smaller compared to the size of the liquid drop.

The roughness of the substrate, which is designated as r , is defined as the ratio of the real surface area ($A_{surface}$) to the apparent surface area that is the projection of the real surface area ($A_{surface}$) over the surface plane (Wenzel, 1936)

$$r = \frac{A_{surface}}{A_{projected}} \geq 1 \quad (2.6)$$

The apparent contact angle θ^* , which is the contact angle observed above the rough features on the virtual surface plane, can be evaluated by considering a small displacement dx of the triple line in a direction that is parallel to the base substrate, as indicated in Figure 2.5. Therefore the surface energies variation dE can be expressed as (Wenzel, 1936)

$$dE = r(\gamma_{SL} - \gamma_{SG})dx + \gamma_{LG}dx \cos \theta^* \quad (2.7)$$

where r is the roughness of the solid. The zero gradient of surface energy E ($dE/dx = 0$) defines equilibrium (de Gennes et al., 2004; Quere, 2008; Eustathopoulos et al, 1999). Note that the first term on the right hand side describes the surface energy change associated with replacement of solid-gas interface by solid-liquid one; the second term on the right hand side defines the surface energy change caused by the variation of liquid-gas interface.

The purpose of our analysis is to model the wetting equilibrium in terms of surface roughness and contact angles, i.e. the apparent contact angle θ^* and the Young's contact angle θ_E .

In the case that the surface is considered as smooth, namely $r = 1$, the Young's equation (Equation 2.2) is recovered at the equilibrium state from Equation 2.7.

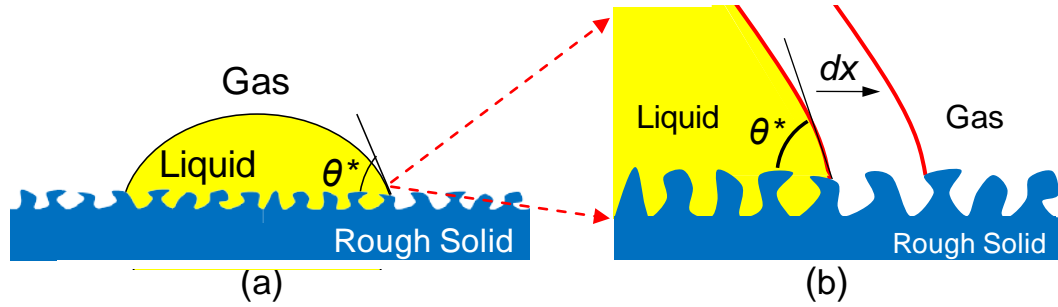


Figure 2.5: (a) A small droplet wetting on a physically rough substrate with an apparent contact angle θ^* . (b) The displacement within the domain of the right edge in (a).

If the surface is rough, when $r > 1$, the equilibrium condition leads to the Wenzel's relation

$$\cos \theta^* = r \cos \theta_E \quad (2.8)$$

where θ_E is Young's contact angle defined by Equation 2.2.

The Wenzel relation (Equation 2.8) predicts that the roughness plays a role of enhancing the wettability (Wenzel, 1936). If the roughness factor r is larger than 1, a hydrophilic solid (associated with “mostly wetting” condition with $\theta_E < 90^\circ$) becomes more hydrophilic ($\theta^* < \theta_E$), and conversely, a hydrophobic solid (associated with “mostly non-wetting” condition with $\theta_E > 90^\circ$) shows an increased hydrophobicity ($\theta^* > \theta_E$). The Wenzel relation, however, is limited to some extent if the Young's contact angle of the liquid is within certain ranges (Quere, 2008). The domain of validity of Wenzel relation will be specified for different contact angle ranges in the discussion in “Composite rough surfaces” later in Section 2.1.4.3.

2.1.4.2 The Cassie-Baxter Model

The Cassie-Baxter model (Cassie and Baxter, 1944) is dealing with a chemically heterogeneous surface. It is assumed that the surface is composed of two distinct materials (Figure 2.5), each characterized by its own contact angle θ_1 and θ_2 , respectively. The fractional surface areas occupied by each of these materials are designated by f_1 and f_2 thus $f_1 + f_2 = 1$. It is also assumed that the individual areas of each material are significantly smaller than the size of a liquid drop.

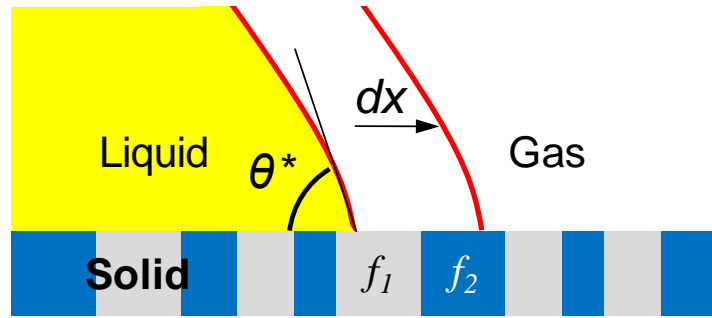


Figure 2.6: A small droplet wetting on a chemically heterogeneous substrate composed of different material characterized with the area fractions f_1 and f_2 .

The apparent contact angle, which is observed above the surface, is again designated as θ^* . The surface energy variation due to the displacement dx indicated in Figure 2.6 will be expressed by Equation 2.9 in accordance with (Cassie and Baxter, 1944)

$$dE = f_1(\gamma_{SL} - \gamma_{SG})_1 + f_2(\gamma_{SL} - \gamma_{SG})_2 + \gamma_{LG} dx \cos \theta^* \quad (2.9)$$

where the indices 1 and 2 refer to those two material fractions swept by the liquid during the displacement, respectively. The minimum of surface energy E , combined with Young's equation will lead to the Cassie-Baxter relation (Cassie and Baxter, 1944)

$$\cos \theta^* = f_1 \cos \theta_1 + f_2 \cos \theta_2 \quad (2.10)$$

Therefore, the apparent angle is indeed restricted to the interval $[\theta_1, \theta_2]$. The Cassie-Baxter model can be applied to the air-pocket regime and penetration regime that we will discuss in the subsequent section about "Composite rough surfaces".

2.1.4.3 Composite Rough Surfaces

The domain of validity of the Wenzel relation will be examined now in a more detail. The transition between Wenzel relation and Cassie-Baxter relation is discussed.

If a substrate is hydrophilic ($\theta_E < 90^\circ$), under a certain pre-defined condition the liquid would start to penetrate the topographical features of the roughness. This process is similar to a thin porous medium penetrated by a liquid phase. Bico and Quere (Bico et al., 2001) purposed a concept of a critical contact angle, which is designated as θ_C , for such a hydrophilic solid rough surface liquid penetration/imbibition. That critical contact angle is considered as the threshold for the wetting transition between Wenzel and Cassie-Baxter conditions, Figure 2.7 (Bico et al., 2001). In the recent decades, a series of studies by Quere et al were devoted to analyze this wetting transition (Lafuma and Quere, 2003; Ishino et al., 2004; Quere, 2002; Bonn and Ross, 2001; Quere and Reyssat, 2008).

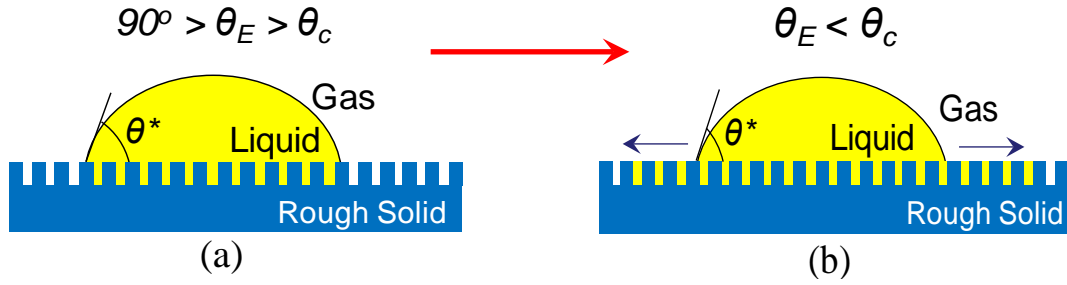


Figure 2.7: A droplet over a horizontal rough surface in equilibrium: (a) Wenzel's model and (b) the penetration case (Cassie-Baxter model)

For the purpose of simplicity of the penetration the surface roughness is assumed to be composed of an array of well-defined pillars or a network of grooves. The predefined surface roughness is penetrated and filled by a liquid and the top of the roughness remain dry. One of the objective is to calculate the apparent contact angle θ^* in the configuration depicted in Figure 2.7 (b). Note that in this case the liquid will penetrate the surface roughness and the associated kinetics of such a triple line movement will be discussed in Section 2.2.4. The relative fractions of the solid remaining dry and the liquid/gas interface area are designated as ϕ_s and $(1 - \phi_s)$ respectively. The drop is in fact sitting on a wetted substrate considered as a patchwork of a solid and a liquid. The Cassie-Baxter relation (Equation 2.9) can be applied to such a mixed surface, with contact angle θ_E (liquid/solid) and 0 (liquid/liquid), respectively. The apparent contact angle can be expressed by using Cassie-Baxter relation as follows (Bico et al., 2001; de Gennes et al., 2004)

$$\cos \theta^* = 1 - \phi_s + \phi_s \cos \theta_E \quad (2.11)$$

The condition for this description to be valid is that a penetrating film of liquid is to develop. Therefore a criterion for a liquid to penetrate into the surface roughness is expected. As a wetting film advances/penetrates by a distance dx on such a surface, the corresponding energy variation per unit length is given by (Bico et al., 2001)

$$dE = (r - \phi_s)(\gamma_{SL} - \gamma_{SG})dx + (1 - \phi_s)\gamma_{LG}dx \quad (2.12)$$

It is clearly that the movement of the film is energetically favorable if $dE < 0$, therefore the cosine of the Young's contact angle involves the following inequality (Bico et al., 2001)

$$\cos \theta_E > \cos \theta_C, \text{ with } \cos \theta_C = \frac{1 - \phi_s}{r - \phi_s} \quad (2.13)$$

Therefore when $\theta_E < \theta_C$, a film of liquid will penetrate the surface roughness and θ_C is always between 0 and 90° as expected. The physical phenomenon and associated kinetics of such a penetration will be discussed in later section 2.2.4 which focuses on a capillary flow over a rough surface.

When Young's contact angle is between θ_C and 90° , the solid remains dry ahead of the drop and the Wenzel relation describes wetting condition correctly. When it is between 0° and θ_C , a film will penetrate the surface roughness and the drop rests on solid/liquid composite, in which case modified Cassie-Baxter model (Equation 2.11) offers a correct description of wetting (Quere, 2008; Bico et al, 2001).

If a substrate is hydrophobic ($\theta_E > 90^\circ$) then it is not expected that the solid/liquid interface to conform to the topographical features of the solid surface, which is contrary to the case described by the Wenzel relation (Quere, 2008; de Gennes et al., 2004).

In such a case, air can actually remain trapped under the liquid drop. Therefore the drop rests on a composite surface made of both solid and air. Figure 2.8 (a) shows a Wenzel condition and Figure 2.8 (b) offers the configuration of the air-pocket case.

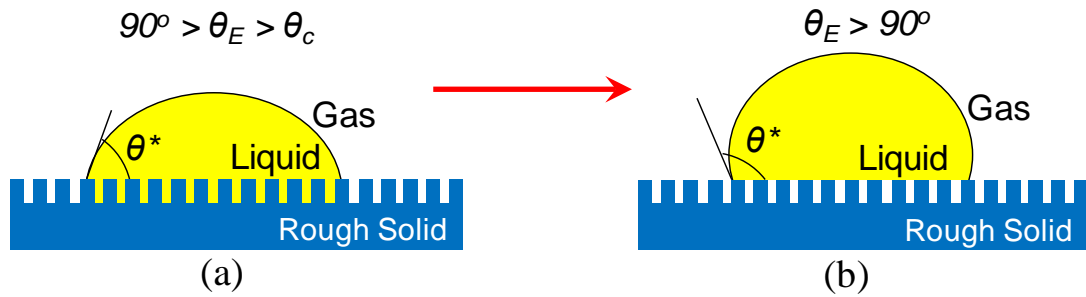


Figure 2.8: A droplet over a horizontal rough surface in equilibrium: (a) Wenzel's model and (b) the air-pockets case (Cassie-Baxter model)

The fraction of liquid/solid interface is designated as ϕ_s and the fraction of the liquid/gas interface on the top of roughness should be $(1 - \phi_s)$. Again, the surface is a mixed surface and the Cassie-Baxter relation can be applied to determine the apparent contact angle indicated in Figure 2.8 (b).

The relation between the apparent contact angle and Young's contact angle is given as follows

$$\cos \theta^* = -1 + \phi_s (\cos \theta_E + 1) \quad (2.14)$$

Similar to the hydrophilic case, a criterion for the air-pocket case should be devised. Johnson and Dettre (Johnson and Dettre, 1964) established a threshold surface roughness, denoted as r , for the formation of the air-pockets.

$$r = 1 + \frac{\tan^2 \theta_E}{4} \quad (2.15)$$

Beyond such a threshold r , the air/gas pockets are trapped and Equation 2.11 must be used to evaluate the apparent θ^* .

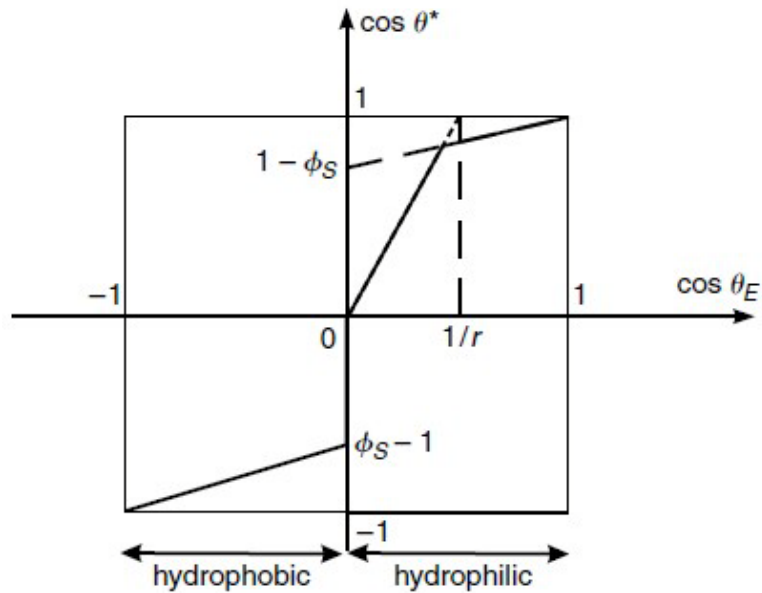


Figure 2.9: Apparent contact angle as a function of Young's contact angle (via their cosines) for a liquid on a rough surface (Figure adopted from (de Gennes et al., 2004))

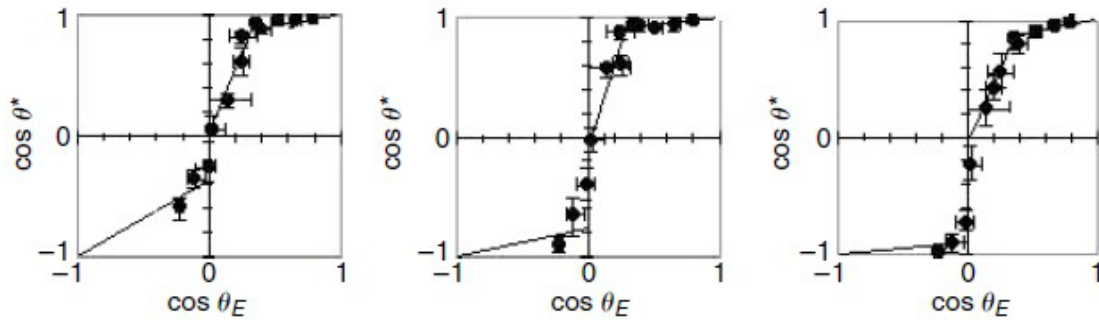


Figure 2.10: Experimental data showing the apparent contact angle as a function of Young's contact angle (measured on a planar surface) for various substrates with a random roughness that is increasing from left to right (Figures adopted from (Shibuichi et al., 1996; de Gennes et al., 2004))

In conclusion, as indicated in Figure 2.9, the wetting of a rough surface in a hydrophilic regime can be described by Equation 2.8 and Equation 2.11 and that in a hydrophobic regime obeys Equation 2.13. In order to model a certain wetting state, the proper wetting equations should be determined by the range of the value of the associated contact angle, as summarized in Figure 2.9. Experimental data indicated in Figure 2.10 were obtained with various complex rough surfaces in the study of Shibuchi et al (Shibuichi et al., 1996). These data clearly match the main features displayed in Figure 2.9 and illustrate the validity of theoretical models to a significant degree.

2.2 Capillarity

Capillarity is a fluid kinetics phenomenon associated with the two immiscible phases featuring deformable interface, thus minimizing its energy (Bonn et al., 2009; Nalwa, 2001) The driving force for such a phenomenon is surface tension and thus

capillarity is also known as surface tension effects (Barnes and Gentle, 2011). The occurrence of a capillarity requires a good wetting between the liquids and the material of which the capillary (or similar structure) is made. Herein the good wetting is defined by an equilibrium contact angle smaller than 90° as described in Section 2.1.2 (Milldeman, 1995; Barnes and Gentle, 2011).

The field was created in early 19th century by Pierre Simon de Laplace and Thomas Young. Capillarity plays a significantly important role in nature for millions of years and the study about it facilitates people's modern life in many ways (de Gennes, 1985; de Gennes et al., 2004; Bonn et al., 2008).

2.2.1 Capillary Length and Menisci

The capillary length is a particular length beyond which gravity cannot be negligible in a surface tension driven phenomenon, Appendix A. It is often designated as κ^{-1} and defined as follows (Barnes and Gentle, 2011)

$$\kappa^{-1} = \sqrt{\gamma / \rho g} \quad (2.16)$$

where ρ represents the density of the liquid and g is the gravity acceleration. The surface tension for liquid-gas interface is denoted as γ . The capillary length is generally of the order of a few millimeters (Barnes and Gentle, 2011; de Gennes, 1985; de Gennes et al., 2004; Bonn et al., 2008). Note that the physical range of this length is the maximum rise of a liquid on a perfectly wetted vertical plate. Some literature sources define this quantity as $lc = (2\gamma / \rho g)^{1/2}$, (Eustathopoulos et al, 1999).

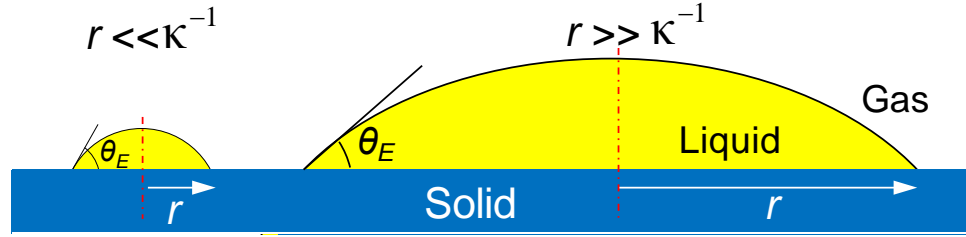


Figure 2.11: A small droplet with $r \ll \kappa^{-1}$ (left) and a large droplet with $r \gg \kappa^{-1}$ (right) over a horizontal smooth surface in equilibrium

As indicated in Figure 2.11 (left), for a droplet with a radius less than κ^{-1} , the capillary force is the dominant factor (see Appendix A). Therefore, in accordance with Laplace’s equation (Laplace, 1805; Defay and Prigogine, 1996; Eustathopoulos et al, 1999), such a droplet deposited on a horizontal surface has the shape of a spherical cap whose edges intersect the substrate at an angle of θ_E . For a large drop whose radius exceeds κ^{-1} , as shown in Figure 2.11 (right), gravitational effects dominate. Such a drop is flattened by gravity. At equilibrium the drop possesses the shape of a liquid “pancake” with a thickness which is dependent on the capillary length and the equilibrium contact angle (de Gennes et al., 2004).

When a liquid is in contact with a vertical solid wall, the surface of the liquid is distorted or curved in the domain near the walls whereas elsewhere is horizontal in a gravity field (and no other forces present) due to gravity effects. The meniscus [often a liquid/gas interface in equilibrium, forming a curvy shape (often called an “elastic curve”) that minimizes the potential energy of the surface] is the region where the liquid surface is curved. A typical example is offered in Figure 2.12 illustrating a meniscus facing a vertical plate for a liquid-solid system associated with the “mostly wetting” condition ($\theta_E < 90^\circ$).

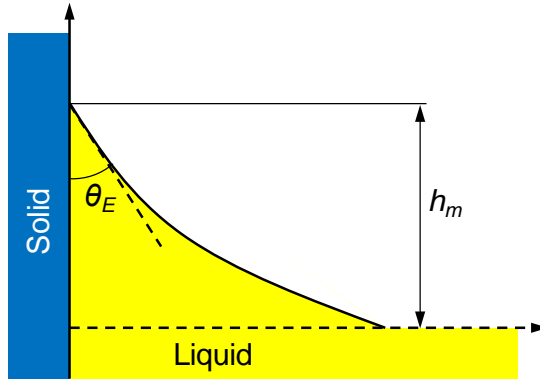


Figure 2.12: Meniscus of a liquid facing a solid vertical wall associated with “mostly wetting” condition

The equilibrium height of the meniscus is associated with the capillary length of the liquid and the equilibrium contact angle (de Gennes et al., 2004)

$$h_m = \sqrt{2\kappa^{-1}(1 - \sin \theta_E)^{1/2}} \quad (2.17)$$

Usually the typical dimension of the meniscus for water, organic liquids and molten metals, i.e., ethanol, Al-Si alloy and so on, is of the order of a millimeter (Barnes and Gentle, 2011; de Gennes, 1985; de Gennes et al., 2004; Bonn et al., 2008).

2.2.2 Capillary Flow through a Single Cylindrical Tube

The dynamics of the penetration of liquids into cylindrical capillaries were studied by E. W. Washburn in 1921 (Washburn, 1921). It was found in Washburn’s study that the distance penetrated by a liquid flowing under capillary pressure alone into either a horizontal capillary or one with small internal surface is proportional to the square root of time.

As indicated in Figure 2.13, the problem is simplified by assuming that one is dealing with a single capillary tube with a uniform internal circular cross-section throughout and the radius being r . The tube topography along its arbitrary length may be of any shape. The tube is represented by its AB segment. The open end A of the tube is placed in contact with a liquid in a reservoir with a depth h above the center of its A-port opening. The end B of the tube is closed at the end and the tube is evacuated prior to establishing the connection with the reservoir at the port A. A point M represents a random location between both ends, A and B. The tube length from A to M is designated as l and the associated linear distance is l_s (defined within the dotted box), and ψ is the angle formed between the horizontal line and the line AM. Note the direction of gravity field is marked associated with gravitational acceleration g in Figure 2.13.

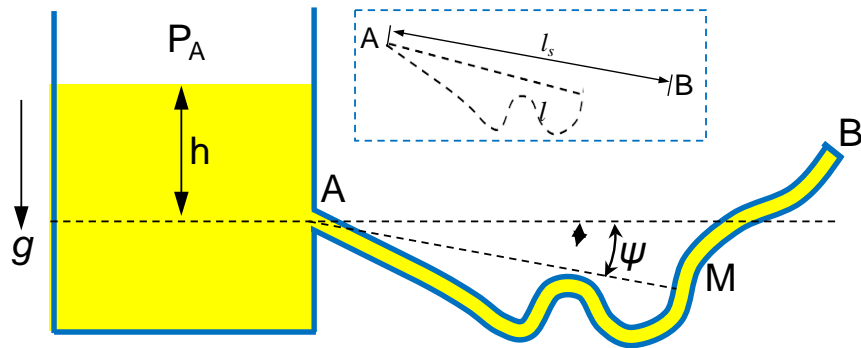


Figure 2.13: A liquid flowing through a cylindrical capillary tube (Washburn, 1921)

It is noted that in Washburn's study an assumption was made that the capillary is small enough that the Poiseuille law (Milldeman, 1995) may be applicable to the entire domain of the flow. Therefore for such a capillary tube the Poiseuille's law may take the following form as in Equation 2.18 (Washburn, 1921)

$$dV = \frac{\pi \Sigma P}{8 \mu l} (r^4 + 4 \varphi r^3) dt \quad (2.18)$$

where dV is the elemental (differential) volume of the liquid which flows through any circular (r) cross-section of the capillary in the time interval dt and l is the tube length in connection with points A and M. This equation offers an expression for the volumetric flow rate of a liquid flowing through a capillary. Note that l represents the column of liquid in the capillary at the time t . The quantity μ is the viscosity of the liquid and φ is slip coefficient which was assumed to be zero for all liquids that wet the capillary, and ΣP is the total effective pressure which is acting to drive the liquid through the capillary.

The total driving pressure is composed of atmospheric pressure P_A , the hydrostatic pressure P_h and the capillary pressure P_C . The hydrostatic pressure can be expressed as (Washburn, 1921)

$$P_h = h \rho g - l_s \rho g \sin \psi \quad (2.19)$$

where ρ is the density of the liquid and g is the gravitational acceleration. The capillary pressure has the expression as follows (Washburn, 1921)

$$P_c = \frac{2\gamma}{r} \cos \theta \quad (2.20)$$

where γ represents the liquid-gas surface tension and θ is the contact angle.

Therefore with $dV = \pi r^2 dl$ combination of Equations (2.18 – 2.20) gives the expression of the velocity of the liquid penetration (Washburn, 1921)

$$\frac{dl}{dt} = \frac{[P_A + g\rho(h - l_s \sin \psi) + (2\gamma/r) \cos \theta](r^2 + 4\varphi r_c)}{8\eta l} \quad (2.21)$$

In case the penetration of a single closed capillary tube is dominated by only the capillary pressure, which is also known as wicking (Quere, 2008). The atmospheric pressure P_A and the hydrostatic pressure P_h could be neglected in comparison with the capillary pressure P_c . It is also noticed that the coefficient of slip φ is equal to zero, which is the case for all liquids which wet the capillary. Therefore for a ψ ranging from 0 to 90° Equation 2.21 will lead to (Washburn, 1921)

$$\frac{dl}{dt} = \frac{\gamma}{\eta} \frac{r}{4l} \cos \theta \quad (2.22)$$

Equation 2.22 offers the Washburn-type kinetics: the rate at which a liquid penetrates any capillary with a small cross sectional surface under its own capillary pressure is directly proportional to the radius of the capillary, to the cosine of the contact angle, to the ratio of the surface tension to the viscosity of the liquid and inversely proportional to the penetration length.

Equation 2.22 will evolve into its final form after the integration [with $t \in [0, t]$ and $l \in [0, l]$] (Washburn, 1921)

$$l^2 = \left(\frac{\gamma \cos \theta}{\eta} \right) \frac{rt}{2} \quad (2.23)$$

Equation 2.23 indicates that *the penetration distance is directly proportional to the square root of the associated time*. The quantity $(\gamma / \eta) \cos \theta / 2$ is called coefficient of penetration which measures the penetrating “power” of a liquid.

It should be noticed that Richard Lucas et al. (Lucas et al., 1918) have studied the same problem and obtained the similar results around three years earlier and therefore this square root relation for a capillary penetration is also known as Lucas-Washburn law.

2.2.3 Capillary Flow through a Single Open Surface Groove

The capillary driven flow of liquids in a single open surface channel (also called hemiwicking by Quere (Quere, 2008)) was studied extensively in the last decade of the last century. A Washburn-type model for the capillary flow through a single open groove was established and verified by empirical data for a wide selection of liquids (Rye et al., 1996; Yost et al., 1997; Rye et al., 1998; Mann et al., 1995; Romero and Yost, 1996). The model was built by balancing the dominant driving and retarding forces (capillary force and viscous force, respectively) in the capillary flow process. In what follows, we will review a straightforward approach to the derivation of the model.

Figure 2.14 (a) depicts the experimental configuration of a liquid flowing through a single straight open surface groove from a single source. The flowing distance which is

a function of time is designated as $z(t)$. Figure 2.14 (b) offers a cross sectional view and geometrical details of the open triangular groove. In Figure 2.14 (b), R_c represents the radius of curvature of the liquid free surface, θ is the contact angle, α and β are groove angles, h_0 is the height of the surface groove and h is the the vertical distance between the groove bottom and the triple line of the liquid within the groove.

During the spreading process, the capillary driving force associated with the surface energy change can be defined by (Rye et al., 1996)

$$F_\gamma = \frac{2h_0\gamma}{dz} \left[\cos(\theta) - \frac{(\alpha - \theta)\cos(\alpha)}{\sin(\alpha - \theta)} \right] \quad (2.24)$$

Equation (2.23) was obtained by considering the variation of surface energy caused by the changes of the interfaces among gas, liquid and solid phases.

Assuming the flow through a single open triangular groove as satisfying the conditions of the Poiseuille flow, the viscous dissipation force, which is established by multiplying the pressure drop associated with viscous effects and its exerted area, can be expressed as follows (Rye et al., 1996)

$$F_\mu = 8\pi\mu z \frac{dz}{dt} \quad (2.25)$$

Note that the viscous force is for a cylindrical capillary with an equivalent cross sectional area of an open triangular groove. Balancing the capillary driving force and the

viscous force with a negligible gravity force would lead a Washburn-type kinetics model (Rye et al., 1996)

$$z^2(t) = K(\alpha, \theta) \frac{\gamma h_0}{\mu} t \quad (2.26)$$

where

$$K(\alpha, \theta) = \frac{1}{2\pi \sin(\alpha)} \left[\cos(\theta) - \frac{(\alpha - \theta) \cos(\alpha)}{\sin(\alpha - \theta)} \right] \quad (2.27)$$

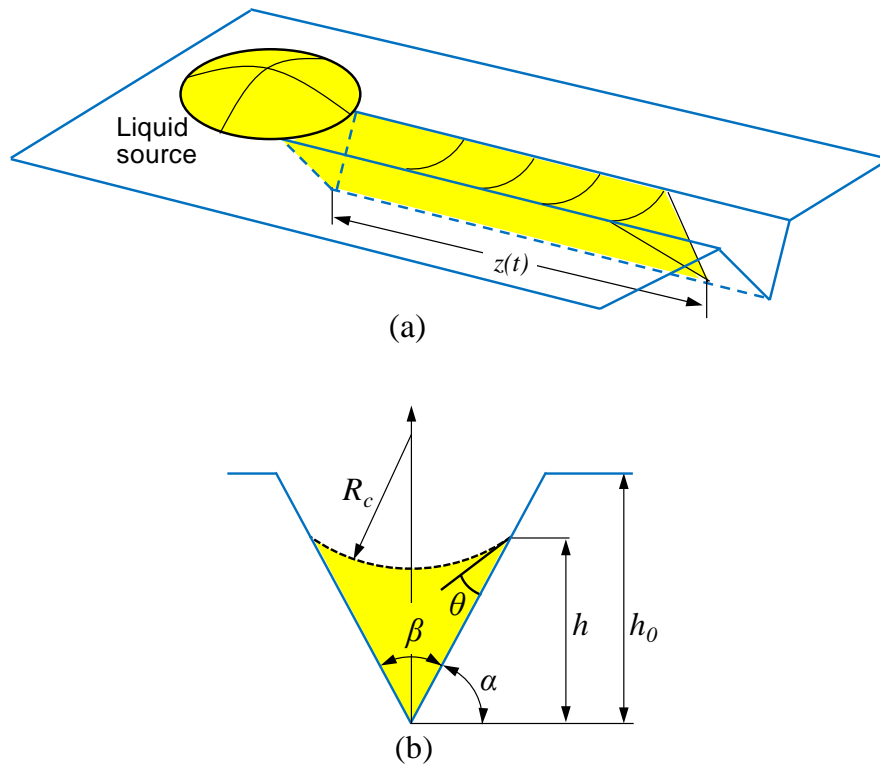


Figure 2.14: (a) capillary flow through a single open surface groove, (b) a cross sectional view of the open triangular groove.

The theoretical model Equation (2.25) offers a good match with the empirical data obtained with various types of organic liquids. Therefore the established Washburn-type model for liquids flowing through a single open triangular surface groove was proved to be valid (Rye et al., 1996; Yost et al., 1997; Rye et al., 1998; Mann et al., 1995; Romero and Yost, 1996).

2.2.4 Capillary Flow over Rough Surfaces

Spreading liquid over a topographically complex rough surface requires a more elaborate study. A rough surface can be considered as a two dimensional porous medium and likely to be penetrated by a liquid. When a on the surface positioned sessile drop is in contact with the rough features of the surface interface, it can be imagined that a liquid film propagates within the domain of the roughness features so that the drop eventually would be exhausted at the source location. The criterion for such a penetration will be discussed in section 2.1.4, devoted specifically to wetting of a rough surface. Such a phenomenon is in literature termed variously, i.e., penetration, invasion, imbibition or impregnation. It should be noticed that in this dissertation, we prefer to use the term imbibition. This phenomenon has been of a high interest, and has been studied extensively primarily in the last decade and mostly for polymers and organic liquids systems (Bico et al, 2001; Hay et al., 2008; Dussaud et al., 2003; Ishino et al., 2007; Chen et al., 2009; Courbin et al., 2007; Zhao et al., 2009; Bico et al., 2002; Apel-Paz and Marmur, 1999; Cazabat and Stuart, 1986; Courbin et al., 2009; Blow et al, 2009).

As emphasized by Quere (Quere, 2008), a well controlled micro- or nanotextures on a solid may induce roughness effects on wetting. One may take an advantage of this

effect in order to induce preferable wetting properties, such as spontaneous filmification, superhydrophobicity, superoleophobicity, and interfacial slip (Quere, 2008).

Bico et al (Bico et al, 2001) studied wicking of a silicone oil over a microstructured surface with regular micron-sized spikes composed of a silicon wafer and a sol-gel silicate coating. A theoretical Washburn-type model was established by balancing the surface energy change due to the liquid spreading and associated viscous dissipation. The model works well but requires a specific empirical numerical parameter inclusion. Note that this numerical parameter is without clear physical meaning, and it is also proved to be of the same value for a various liquid systems stated by the authors. A few years later, the same phenomenon was modeled by Hay et al (Hay et al., 2008). In that study, wicking over a microstructured surface was considered as a spreading over a surface with a series of parallel channels. The model for wicking in a collection of parallel channels was established by balancing frictional resistance against capillary driving force and assuming different channel cross sections. A Washburn type relation was also confirmed. The model of a channel having vertical walls and a specific tapering angle gave an excellent agreement with the experimental data.

Dussand et al (Dussaud et al., 2003) analyzed the role of skin texture in the passive transport of liquids on human skin by characterizing the advance of Newtonian liquids following controlled fluid deposition. The liquid drop with constant shape (infinite drop reservoir maintained by constant pressure syringes) was deposited on a replica of human skin. The topographical features of the skin were characterized as a network of open triangular surface grooves. The analytical model established in that study recovered the Washburn-type kinetics for the early stage of the spreading process.

The experiments indicated that most of the oils would penetrate within the fine surface grooves and the associated liquid fronts advanced with obeying a relation close to the established theoretical model.

Ishino et al (Ishino et al., 2007) proved that wicking kinetics within forests of micropillars (regularly distributed) may behave differently depending on the ratio between the height of the pillar and the pitch of the network. Silicon surfaces serving as substrates were decorated with micropillars having different pillar heights, radius and pitches. Various silicon oils were used as spreading liquids for the wicking experiments on such manufactured substrates. A distance of the spreading front from the origin of the liquid mass vs. square root of time ($z \sim t^{1/2}$) relation was established for the wicking kinetics. A theoretical model for estimating the viscous force that the liquid experienced within the micropillars and the substrate bottom was established. Chen et al (Chen et al., 2009) manufactured various structured surfaces with several uniformly distributed micropatterns of distinct but regular geometric shapes, i.e., squares, regular hexagons and octagons. Methanol was used as the wicking liquid. The structured surfaces are fabricated using Bosch deep reactive ion etching and a potassium hydroxide wet etching process. All the kinetics data confirm that wicking over such porous surfaces obeys Washburn law.

Recently, Courbin et al (Courbin et al., 2007) studied imbibition of various liquids over surfaces (made of polydimethylsiloxane transparent elastomers) with the same microstructures. Drops of the same size ended up with distinct wetted areas and shapes. The main conclusions of this study can be summarized as (i) different imbibition shapes (of the triple line locust of points) can be obtained by changing the liquid, (ii) the drop

volume controls the size of the wetted area, and (iii) the kinetics of the imbibition along either the diagonal or axial direction follows Washburn relation.

2.3 Flow through Porous Media

In the study within the scope of this dissertation, one of main hypotheses is that surface roughness domain of a rough surface would be treated as a porous medium domain (the detailed interpretation will be provided later in Chapter 3, 4 and 5). Therefore the main theories associated with porous media, i.e., Darcy's law, would be included in this consideration.

Henry Darcy's investigations in 1856 (Darcy, 1856) into the hydrology of the water supply of Dijon and his experiments on steady-state unidirectional flow in a uniform medium revealed a proportionality between flow rate and the applied pressure difference. What Darcy stated was that when water flows vertically downward through a bulk of sand, the volume of water Q passing through the system in unit time is given by $Q = -KA(h_2 - h_1)/l$, where K is a factor of proportionality, A the area of cross section and l the thickness of the sand, and h_1 and h_2 the heights above a standard reference elevation of water.

In modern notation Darcy's law is expressed in three dimensions in a refined general form as (Hubbert and Willis, 1957)

$$\mathbf{v} = \mu^{-1} \mathbf{K} \cdot \nabla P \quad (2.28)$$

Here ∇P is the pressure gradient in the flow direction, \mathbf{v} represents the velocity of the fluid and μ is the dynamic viscosity of the fluid. The coefficient \mathbf{K} is independent of the nature of the fluid but it depends on the geometry of the medium. It has dimensions of (Length)² and is called the specific permeability or intrinsic permeability of the medium. In the case of single phase flow, we abbreviate this to permeability. Note that the permeability \mathbf{K} is in general a second-order tensor for a non-isotropic three dimensional porous domain and a multidimensional movement of the associated liquid (De Wiest et al., 1969; Scheidegger, 1974).

For the case of a single dimensional isotropic (or axi-symmetric) medium the permeability is a scalar and the Darcy's law is simplified as (Hubbert and Willis, 1957)

$$u = -\frac{K}{\mu} \frac{\partial P}{\partial x} \quad (2.29)$$

The values of K for natural materials vary widely. The typical value for clean sands is within the range of 10^{-9} to 10^{-12} with a unit of m^2 (Hubbert and Willis, 1957).

It should be pointed out that Darcy's law has been widely used in numerous fields of inquire, including hydrology (Fetter, 1994), geology (Clarke et al., 1993) and heat transfer (Bejan, 2004). In this study, Darcy's law will be utilized as a momentum equation, combined with the mass conservation principle.

2.4 Wetting and Capillarity in Soldering and Brazing

A significant complexity is associated with the study of surface tension driven phenomena of liquid metals at elevated temperatures. These phenomena are important for real manufacturing processes, i.e., soldering and brazing.

An effort was made to offer a full blown set of transport equations involving continuity, momentum, energy and concentration, by Boettinger's et al. (Moon et al., 1996; Compell and Boettinger, 2000). A serious consideration of the constitutive equations involving capillarity, reactions, Marangoni effect etc. has been offered (Braun et al., 1995). A series of studies of surface tension phenomena at high temperatures has been conducted by Eustathopoulos et al (Landry and Eustathopoulos, 1996; Eustathopoulos et al., 1998; Dervet et al., 1996; Landry et al., 1996; Espie et al., 1994; Eustathopoulos, 2005) during the recent decades. These studies include wetting of various systems, i.e., metal/metal and metal/ceramic, with an objective to provide a better understanding, and to explore a realistic model for wetting at high temperatures.

This section offers (i) a brief introduction of processes associated with soldering and brazing, (ii) a brief account of the importance of wetting and capillarity in soldering and brazing, and (iii) a discussion of basic concepts of reactive wetting and associated wetting kinetics.

2.4.1 Soldering and Brazing

In accordance with American Welding Society (AWS) (AWS Brazing Handbook, 1991; AWS Soldering Handbook, 1999), joining processes can be considered as coming under one of two generalized bonding techniques/methodologies: filler material joining,

or fusion joining. Filler material joining refers to the use of a third material to form a bond between two base materials, and includes the processes of soldering, brazing, and adhesive bonding. The filler material must adhere to both base materials in order to obtain an adequate bond. Although the bonding mechanism in such cases may cause chemical changes at the substrate material surfaces in order to facilitate adhesion, the temperature of substrates does not exceed their respective melting point at any time. Fusion joining refers to the bonding process when the temperature of the substrate materials exceeds their melting temperature. In that case, two base materials are joined by the intermixing of their mutually molten segments. A third material (also referred as a filler material) may be simultaneously melted and added to the molten base materials.

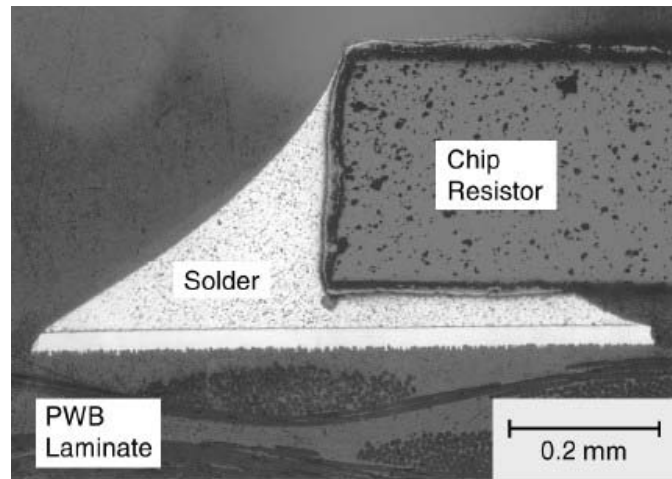
Soldering at low temperature and brazing at high/ultra high temperatures are used in many engineering applications. The difference between soldering and brazing is formally defined by the melting temperature of the filler metal. A filler metal which has a liquidus temperature below 450 °C / 842 °F is referred to as a solder material, or simply a “solder”; a filler metal with a liquidus temperature exceeding 450 °C / 842 °F is a brazing filler metal (AWS Brazing Handbook, 1991; AWS Soldering Handbook, 1999). The distinction between those two processes is primarily semantic, determined solely by a melting property of a filler metal. The process parameters changes such as different temperature ranges, however, lead to numerous specifics involving various mating systems, so the manufacturing processes involved may be quite distinct (AWS Brazing Handbook, 1991; AWS Soldering Handbook, 1999).

2.4.2 Importance of good wetting and capillarity

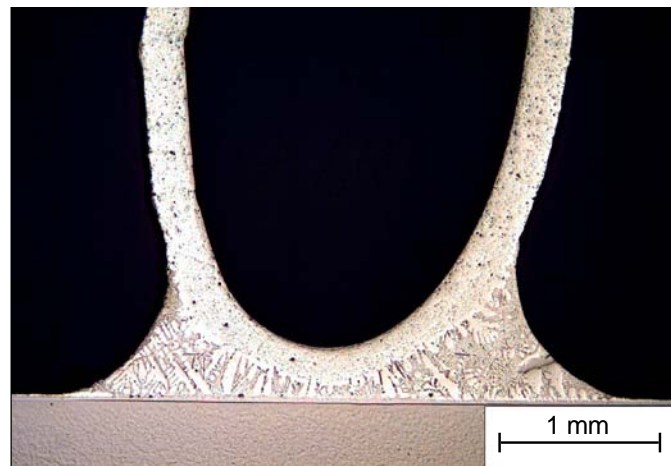
It is widely known that joining by brazing or soldering is possible if the liquid filler metals wet the solids to be joined. The most frequently used criterion to quantify this condition is a liquid melt - substrate contact angle magnitude. In general, it is stated that the contact angle well below 90° (Eustathopoulos et al., 1999) would be required.

Wetting, hence liquid metal (often called filler) spreading is required to distribute the solder/braze over/between the substrate materials (often called mating surfaces) so that upon solidification, the filler metal will bond those surfaces together. Failure of the solder/braze to completely spread on those surface areas will result in the appearance of nonwetted regions of the mating surfaces which, in turn, are in most structural applications unable to support mechanical loads (AWS Brazing Handbook, 1991). It is for this very reason that mechanical strength of a solder/brazing joint relies directly upon the ability of the molten solder/braze to wet and spread over the mating surfaces. Solderability/brazability therefore has become a remarkably crucial aspect of soldering/brazing technology. It is also necessary that the solder/braze, after melting, be able to completely fill the confined clearances. The process by which a molten solder/braze spontaneously fills a confined space such as a hole or a gap is also referred to, in a technical lingo, as capillarity, i.e., capillary flow or capillary filling (AWS Brazing Handbook, 1991). Solderability/brazability describes the capacity of the solder to make the joint between given two substrates. Therefore satisfactory solderability/brazability requires that (i) suitable wettability exists between the solder/braze and the substrates, and (ii) the solder/braze has the capacity to spread over the base materials mating surfaces (AWS Brazing Handbook, 1991).

Figure 2.15 offers metallographic images of bonded samples with satisfied joints which are attributed to the good wetting for a soldering case, Figure 2.15 (a), and a brazing case, Figure 2.15 (b), respectively.



(a)



(b)

Figure 2.15: A cross sectional metallographic view of good wetting case in (a) soldering of a chip resistor to a PWB (image adopted from (AWS Brazing Handbook, 1991)), (b) a good brazing joint (courtesy from Brazing Research Lab at the University of Kentucky)

Table 2.1: Contact angle values and associated solderability/brazability (Data adopted from (Moser et al., 2008))

Contact angle (Degree)	20-30	20-30	30-40	40-55	55-70	70-90
Solderability Brazability	Excellent	Very good	Good	Adequate	Poor	Very poor

The smaller the value of the contact angle, the better is the wetting condition for the soldering and brazing system. Different contact angle ranges within the “wetting” category domain have been identified with qualitative scales of solderability or brazability in Table 2.1 (Moser et al., 2008).

2.4.3 Reactive Wetting

Most of the wetting cases in soldering and brazing, between metal/metal or metal/ceramic at high temperature, are actually reactive wetting cases. In this section, a basic concept of reactive wetting and associated kinetics will be introduced.

2.4.3.1 Brief Introduction of Reactive Wetting

Reactive wetting is generally categorized into two cases (Warren et al., 1998; Eustathopoulos et al., 1999): (i) the case dominated by dissolution of solid in the liquid (dissolutive wetting) (Yin et al., 2006), and (ii) the case that is controlled by the formation a 3D compound by chemical reaction at the solid and liquid interface (Dezellus et al., 2002).

In a dissolutive wetting, when the dissolution of the solid into the liquid is assumed not to change significantly the surface and interfacial energies, the dissolution

modifies only the geometry at the triple line, Figure 2.16. The apparent contact angle is designated as θ_A and true contact angle for a dissolution wetting is referred to as Φ_1 (Eustathopoulos et al., 1999).

Young's equation was derived by considering only displacements of the triple line parallel to a solid/gas interface that is assumed to be undeformable. In dissolutive wetting, deformation of the solid close to the triple line will be considered.

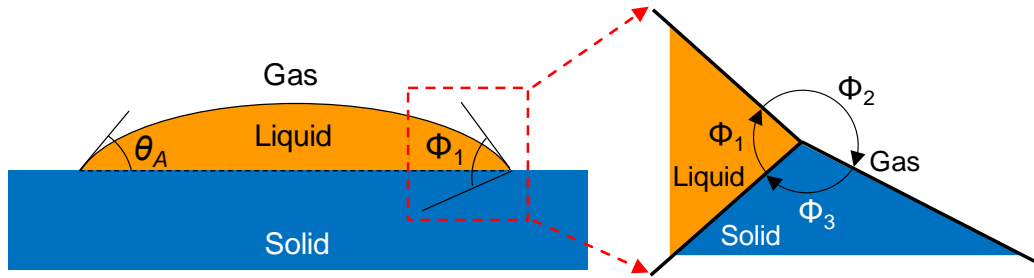


Figure 2.16: Dissolutive wetting: (a) wetting configuration (b) details at the triple line

The local stable equilibrium shown in Figure 2.16 (b) therefore can be described in terms of surface tension at each interface and three dihedral angles Φ_1 , Φ_2 and Φ_3 (Smith, 1948). The exact relation was first given by C.S. Smith (Smith, 1948) as Smith equation:

$$\frac{\gamma_{SG}}{\sin \Phi_1} = \frac{\gamma_{SL}}{\sin \Phi_2} = \frac{\gamma_{LG}}{\sin \Phi_3} \quad (2.30)$$

where Φ_1 is the “true” (i.e., between solid and liquid) contact angle with a relation $\Phi_1 + \Phi_2 + \Phi_3 = 360^\circ$.

Moreover, when the interfacial energies are modified due to dissolution of a small amount of tensio-active species (species that may cause the change of surface tension) of the solid but the solid/liquid interface is assumed to remain nearly flat (Eustathopoulos et

al., 1999). In the case that the wetting is dominated by chemical reaction, two states configurations can be reached as indicated in Figure 2.17 (Eustathopoulos et al., 1999).

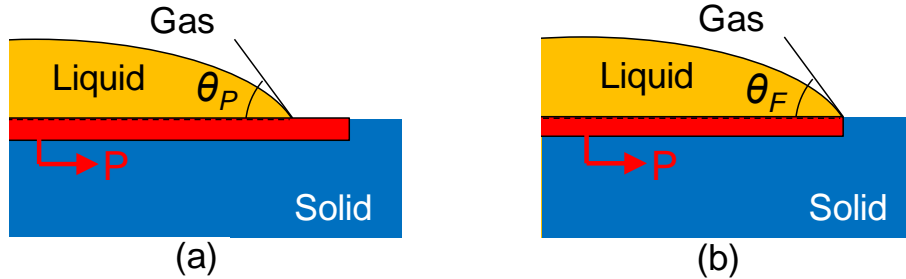


Figure 2.17: Possible configurations of a reacting system at triple line when equilibrium contact angle is reached (a) stable configuration and (b) metastable configuration

In stable configuration, Figure 2.17 (a), the wetting depends on a layer of reaction product P extending on the free surface of the solid substrate in front of the triple line location. Neglecting any effect of roughness of the reaction layer, the wetting condition in this case can be described by (Eustathopoulos et al., 1999).

$$\cos \theta_p \cong \frac{\gamma_{PG} - \gamma_{PL}}{\gamma_{LG}} \quad (2.31)$$

in which θ_p represents the equilibrium contact angle on the reaction product P. (Note that this is identical to the Young's equation, Equation (2.2), but for product P replacing solids designation.)

In metastable configuration, the reaction product layer does not extend beyond the edge of the drop (Figure 2.17 b). Therefore the wetting condition can be described in

terms of final equilibrium contact angle θ_F and associated interfacial energies (Eustathopoulos et al., 1999).

$$\cos \theta_F \cong \frac{\gamma_{SG} - (\gamma_{SP} + \gamma_{PL})}{\gamma_{LG}} \quad (2.32)$$

It is noticed that reactive wetting is governed by the final interfacial chemistry at the triple line rather than by the intensity of interfacial reactions. The challenge is to determine the final contact angle of the system using Equation (2.31) and (2.32)

2.4.3.2 Kinetics of Reactive Wetting

A reactive wetting kinetics is affected by numerous factors such as diffusion, convection, deoxygenation, interfacial reaction and so on. It is difficult to develop a theoretical model for the actual spreading process. Hence, the empirical models haven't been established by fitting experimental data by various functions, i.e., $r(t)$ or $\theta(t)$.

In non-reactive systems, the spreading rate is controlled by the viscous flow and described by a power function of drop base radius, r versus time, t , for angles less than 60° (Eustathopoulos, 1998)

$$r^n \approx t \quad (2.33)$$

where n is determined to be 10 which is consistent with Tanner's law (Tanner, 1979), see also Equations (2.5), (2.23) and (2.26).

In recent decades, Eustathopoulos et al. (Landry and Eustathopoulos, 1996; Eustathopoulos et al., 1998; Drevet et al., 1996; Landry et al., 1996; Espie et al., 1994; Eustathopoulos, 2005) have investigated extensively various reactive systems in an attempt to develop a reaction product control (RPC) model for reactive metal/ceramic

systems, i.e., Cu-Si alloy on SiO₂, Ni on SiC and Cu-Pd-Ti on Al₂O₃. These studies found that in a reactive system, the spreading kinetics is mainly dominated by (i) chemical reactions at the interface within the triple line domain and (ii) transport of reactive elements from the drop bulk to the triple line. There are two limiting cases in such a configuration: diffusion-limited spreading as indicated in Figure 2.16, and reaction-limited spreading as shown in Figure 2.17.

In the diffusion-limited spreading (dissolutive wetting), the local reaction rates are relatively rapid and the extent of local reaction which drives spreading is limited by the diffusive supply of reactants from the drop bulk to the triple line. If the controlling process is dominated by diffusion, a simple diffusion model which neglects convection in a drop and reaction at the interface yields a kinetic model as follows (Eustagopoulos et al., 1999)

$$r^4 - r_0^4 = KVt \quad (2.34)$$

where V is the drop volume and K is a constant.

In the reaction-limited spreading, the kinetics of the chemical at the triple line is controlling since the diffusion within the droplet is comparatively rapid. It may be noted that the impact of diffusion can be considered to be minimal if the drop is made of a reactive metal. It is also assumed that the reaction does not change the global drop composition significantly and a steady configuration is established at the triple line during wetting. Therefore, the rate of chemical reaction and thus the velocity of the triple line advancement is constant with time (Landry and Eustagopoulos, 1996; Dezellus et al., 2002)

$$r - r_0 = Kt \quad (2.35)$$

where K is a constant independent of drop volume. It can be noticed that the wetting kinetics has a linear behavior on r vs t plot. Such a linear wetting can occur in various systems and for different types of reactions, i.e., the Al/vitreous carbon system (Landry and Eustathopoulos, 1996), the reactive CuAg-Ti/Al₂O₃ system (Eustathopoulos et al., 1999), and the AgCuTi/TiAl system (Li et al, 2012). For a system exhibiting linear wetting, it is expected that the spreading rate will be sensitive to the structure of the solid (Eustathopoulos et al., 1999; Drevet et al., 1996).

Kinetics of reactive wetting in a given system is significantly influenced by the experimental conditions. The same system exhibits different kinetics features under different conditions, i.e., temperatures and atmospheres. The temperature may influence the viscosity of a molten metal and change the rate of a chemical reaction between molten metal and base material (Bouche et al., 1998). Moreover atmosphere may have an impact on the formation of the oxide layer on the surface of base materials, which usually prevents the wetting of a molten filler metal (Gale et al., 1999; Shen et al., 2001).

Therefore it is quite difficult to understand the underlying mechanism thus establishing a reliable mathematical model in order to describe the kinetics of reactive spreading. Moreover, in reactive systems the effects of interfacial reactions, diffusion of constituents, and dissolution of substrate on the evolution of contact angle and wetting kinetics are of great importance and need to be explored and quantified (Kumar and Prabhu, 2007).

CHAPTER 3: CAPILLARY RISE OF LIQUIDS OVER A MICROSTRUCTURED SOLID SURFACE*

3.1 Overview

In this chapter, Chapter 3, experimental study is conducted for the capillary rise of five various organic liquids on a microstructured/rough intermetallic surface (IMC0) and a penetration/imbibition phenomenon is registered for all liquids. A theoretical model for a capillary rise of liquids over rough surfaces in a planar fashion is established based on Darcy's law and mass conservation. A validity of the interpretation of a rough surface as a reduced dimensions porous medium is demonstrated. The capillary spreading of liquids in this study is at room temperature and considered to be without any chemical reaction. The modeling methods and procedures for a non-reactive planar penetration/imbibition of liquids, validated in this chapter, provide a theoretical framework for the studies in later chapters, i.e., Chapter 4 and 5, which deal the with spreading of molten solders on rough surfaces at elevated temperatures without reactions.

In this chapter, the location of the triple-line as a function of time has been recorded for a series of organic liquids, with various surface tension to viscosity ratios, wicking upward a rough $\text{Cu}_6\text{Sn}_5/\text{Cu}$ intermetallic (IMC) substrate. The complex topographical features of such an IMC rough surface are characterized by surface porosity and surface roughness. A theoretical model for wicking upward a rough surface in a planar fashion has been established by treating the rough IMC surface as a two dimensional porous medium featuring a network of open micro triangular grooves. The model is verified against experimental data.

* This chapter includes detailed account of material summarized in *Langmuir* (2011), Vol. 27(11), pp. 6720 – 6730

Hence, the study in this chapter (Liu et al., 2011) confirms that the kinetics of capillary rise of organic liquids in a non-reactive flow regime over a porous surface having arbitrary but uniformly distributed topographical features involves (i) surface topography metrics (i.e., permeability, tortuosity/porosity and geometry of the micro-channel cross section); (ii) wicking features (i.e., contact angle and filling factor); and (iii) physical properties of liquids (i.e., surface tension and viscosity). An excellent agreement (i.e., a relative error of 4% – 8%) between theoretical predictions and experimentally obtained data proves, for a selected filling factor η , validity of the analytically established model. Scaled data sets show that, for a given rough surface topography, (i) wicking kinetics of considered liquids depend on properties of liquids, i.e., surface tension to viscosity ratios and contact angles; (ii) the filling factor for all tested liquids is an invariant, offering good prediction within the range of $\sim 0.9 - 1.0$. The distance of the wicking front vs. square root of time relationship was well established throughout the whole considered wicking evolution time.

3.2 Materials and Experimental Procedures

3.2.1 Fabrication of the IMC Surface

The substrate was manufactured from a virgin Cu sheet. A Cu plate was dipped into the molten Sn at 260°C, then the re-solidified Sn coating was etched away to expose the IMC layer formed at the interface. The procedure offered in our previous work (Zhao et al., 2009) has been modified for the fabrication of the intermetallic surface used in this investigation. The modification includes: (a) in step (ii), the dipping time is prolonged to 10s, and (b) in steps (v) and (vii), the etching time and cycles are adjusted according to

the real time experimental observation of the amount of Sn residue. The procedures of manufacturing steps were as follows:

- (i) The Cu substrate of a high purity (99.9%) with thickness of 0.5 mm was cut into a $3.3 \text{ mm} \times 45 \text{ mm}$ plates, ultrasonically cleaned with ethanol and then etched in a mild acid (95% ethanol + 3% HCl + 2% H₂O) for 30 seconds.
- (ii) Subsequently, a plate with deposited rosin flux [182 Mildly Activated Rosin Liquid Flux, Kester®], was dipped into a crucible with pure molten Sn at the temperature of 260°C for 10 s, and quickly pulled out.
- (iii) Each so prepared coupon was subjected to an aging process at 127°C in air for 10 days, to obtain the Cu₆Sn₅/Cu₃Sn/Cu ternary layer.
- (iv) Each so prepared coupon was subjected to an aging process at 150°C in air for 10 days, to obtain the grown Cu₆Sn₅/Cu₃Sn/Cu ternary layer.
- (v) In order to remove the remaining Sn residue from the plate surface, the sample was suspended in a vertical position and immersed in a solution of 1% HCl in methanol, for approximately 20 min at the room temperature in air.
- (vi) The sample was ultrasonically cleaned in a soapy water, rinsed with water, and ultrasonically cleaned again in ethanol for 2 minutes.
- (vii) The steps (v) were repeated for about 3-5 times depending on the amount of Sn residue, the plate was rinsed in methanol and ultimately dried in air at room temperature in free convection.

Four types of IMC rough surfaces are manufactured with following different combinations of those procedures. Note that fabrication details for various IMC rough surfaces are summarized in Table 3.1.

Table 3.1: Fabrication details of IMC rough surfaces

Designation	Aging	Etching	Topographical Features
IMC0	No	Additional 20 mins after removal of Sn	Irregular grains; Randomly/Uniformly distributed
IMC1	No	Stops etching after removal of Sn	Regular polyhedral grains; Randomly/Uniformly distributed
IMC2	127°C 10 days	Stops etching after removal of Sn	Polyhedral grains; Directionally distributed
IMC3	150°C 10 days	Stops etching after removal of Sn	Polyhedral grains; Directionally distributed

The sample treated with steps (i), (ii), (v), (vi) and (vii) with an intentionally over-etching (etching for additional 20 minutes after all Sn residue on the surface is removed) is designated as IMC0 and used in the study stated in this chapter. The dimension of the obtained sample is about 3.3 mm × ~20 mm. Such a surface has a random and complex rough intermetallic interface. Subsequently, the so manufactured substrate was exposed to an experimental procedure aimed at establishing the kinetics of capillary rise of a set of different liquids.

The sample treated with the steps procedures (i), (ii), (v), (vi) and (vii) with no over-etching [etching terminates once the Sn residue (which is in lighter color than the intermetallic) on the surface is removed] is designated as IMC1. Such a surface features a uniform distribution of scallop-like grains, which is studied in the following chapter – Chapter 4.

The sample manufactured by following (i), (ii), (iii), (v), (vi) and (vii) is designated as IMC2. The one with (i), (ii), (iv), (v), (vi) and (vii) is designated as IMC3.

IMC2 and IMC3 both feature parallel traces of the larger grown grains which constitute a set of grooves with preferential direction of topographical features, but with slight different, i.e., different grain sizes. Those two IMC surfaces are examined in Chapter 5.

The reasons that the Cu_6Sn_5 intermetallic surface is considered are listed as follows:

1. The Cu_6Sn_5 intermetallic featuring the scallop like grains on the surface can be considered as a topographically complex surface with microscale roughness. The tunable morphology of Cu_6Sn_5 has been studied by Suh et al. and Zou et al. (Suh et al., 2008a; Suh et al., 2008b; Suh et al., 2007; Zou et al., 2008). The possible impacts on wetting/capillary properties in connection with such a surface roughness have been noticed recently (Zuruzi et al., 1999), and by our laboratory teams more recently (Wang et al., 2006; Zhao et al., 2009a and b)
2. The Cu_6Sn_5 is one of the most critical intermetallic compounds formed during the soldering process (Tu, 2007). It is of a high interest in electronic industry and widely studied during last decades (Chada et al., 1999; Nguyen et al., 2008; Yang et al, 2010)
3. Cu_6Sn_5 has a minimal reaction with PbSn solders at normal soldering temperatures (Appendix B). Therefore in the later chapters it is applied to decouple the chemical reactions from the wetting/capillary problems thus focusing on relevant physical phenomena and modeling establishment.

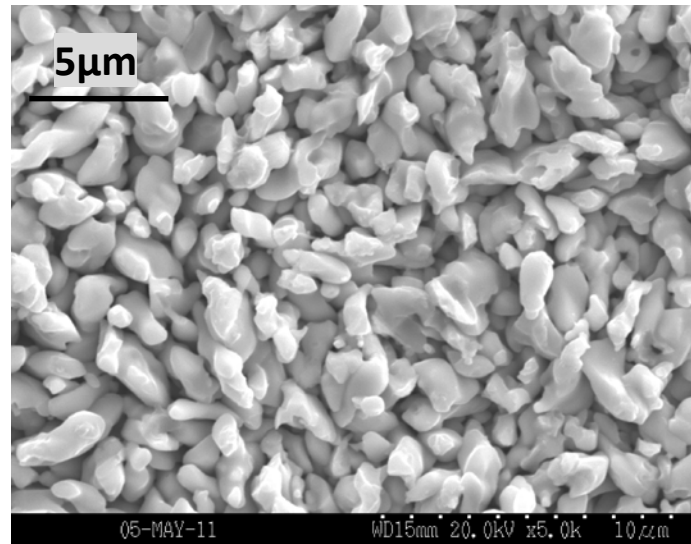
The study summarized in this chapter is intended to explore whether (i) an imbibition (or a hemiwicking as described in Section 2.2.4 in Chapter 2) can be noticed by using rough intermetallic surface in contact with various types of organic liquids to

serve as a benchmark testing of the modeling approach, and (ii) a universal model can be established for the wicking kinetics of liquids over a rough surface with locally non-uniform surface structures but homogeneously distributed, in assumed absence of chemical reaction, and over a vertical substrate in a planar fashion but with a negligible gravity influence or with a non-dominant gravity influence.

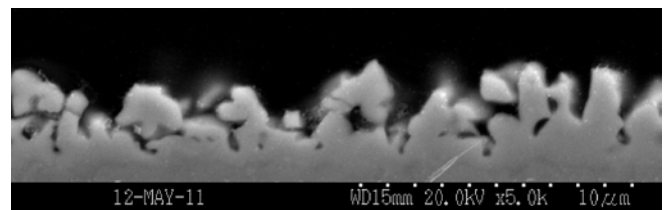
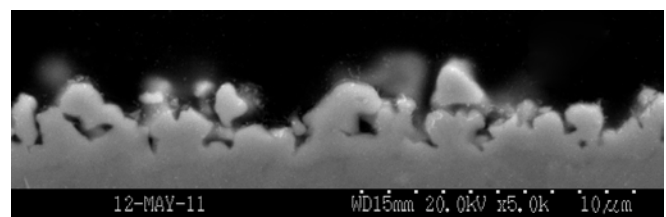
3.2.2 Surface Characterization

Figure 3.1 offers scanning electron microscopy (SEM) images of the topography, Figure 3.1 (a), and cross sections of an IMC0 substrate used for capillary rise tests, Figure 1 (b). A random but uniform distributed roughness composed of grains can be noticed.

In order to obtain reliable data about surface roughness parameters, the IMC0 surface was scanned by Zygo 3D optical surface profiler over an area of $\sim 1.447 \text{ mm} \times 1.085 \text{ mm}$, with a magnification of $200\times$ as indicated in Figure 3.2. The scanning was repeated four times at four different locations. The average surface area and the projected area were 1.947 mm^2 and 1.567 mm^2 , respectively. Therefore, for the IMC surface, the surface roughness r defined as the ratio of surface area across all the surface topographical features to its projected area (Wenzel, 1936), $r = A_{\text{surface}} / A_{\text{projected}}$, is determined to be 1.24 with the standard deviation of 0.03. (Note that the associated projection is onto the horizontal base plane.) The Zygo optical profilometer has a vertical resolution of 0.1 nm and the field of view of 0.04 — 17.5 mm. The surface topography measurements were done at ambient conditions.



(a)



(b)

Figure 3.1: (a) SEM image of the fabricated IMC0 surface showing its topography. (b) SEM images of a cross section view of an IMC0 surface at two different random locations.

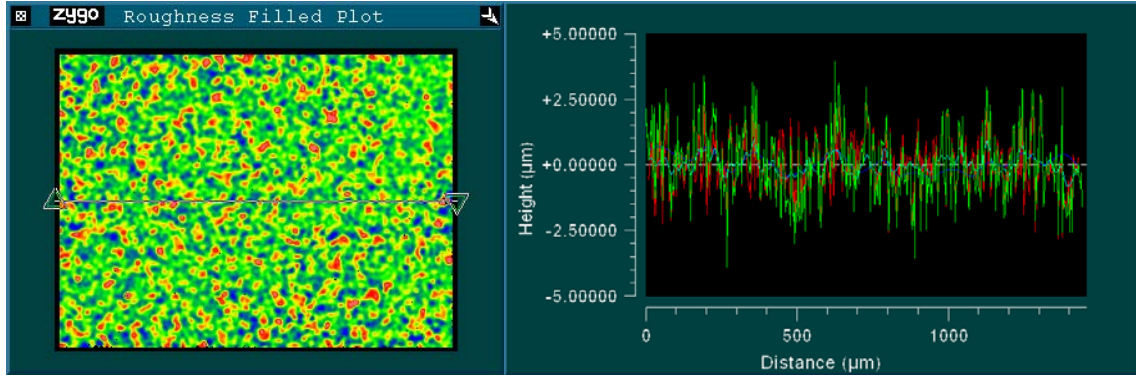


Figure 3.2: Characterization of surface roughness by Zygo optical profilometer. The roughness profile (right) associated with the scan line (left) is indicated.

Table 3.2: Data of roughness measurements for an IMC0 substrate

Measurements	Surface Area (mm ²)	Projected Area (mm ²)	Surface roughness r	Average of surface roughness
1	1.957	1.565	1.25	1.24 ± 0.03
2	1.935	1.568	1.23	
3	1.888	1.567	1.20	
4	2.01	1.568	1.28	

Atomic force microscopy (AFM) was used to characterize the surface topography, especially for the characterization of surface porosity. Note that the surface porosity ε is defined as the ratio of the porous volume within a rough surface domain to the total volume of a rough surface, $\varepsilon = V_{porous} / V_{total}$ (De Wiest et al., 1969; Scheidegger, 1974). A randomly selected area of $50 \mu\text{m} \times 50 \mu\text{m}$ was scanned. The 3D representation of a scanning result in Figure 3.3 (a) shows the surface topography of a fabricated IMC surface. Using WSxM 5.0 Develop 3.3 software (Horcas et al., 2007) the surface porosity ε (De Wiest et al., 1969; Scheidegger, 1974) is determined to be 0.43 in average with a standard deviation of 0.04 for three different scanned areas on the same IMC substrate.

The porosity is determined within the porous domain located on a base and a ceiling planes with a height of 1.5 μm and 5.4 μm , respectively (zero being at the lowest point on the surface). The base and ceiling planes are associated with the heights at which area of porous (a dashed line in Figure 3.3 (b)) or solid (a solid line in Figure 3.3 (b)) domains is $\sim 99.5\%$ of the total scanned area ($\sim 2500 \mu\text{m}^2$), thus minimizing the influence of surface defects or spikes, Figure 3.3 (b). The average height of the IMC rough surface features is measured to be $h_0 = 2.2 \mu\text{m}$ with a standard deviation of 0.2 μm . Figure 3.4 (a) indicates that within base and ceiling planes most of the events (i.e., topographical features considered) are included, which is consistent with Figure 3.3 (b). It should be pointed out that within the defined porous domain, the height of all the topographical features was counted from the base plane, so the corresponding average height generated from the histogram should be reduced by 1.5 μm . The AFM surface profiles in Figure 3.4 (b) with SEM in Figure 3.1 (b) show the presence of V - shaped cross sections of the network channels formed between Cn_6Sn_5 grains. These are the dominant topographic features of the surface. We have established that more than 100 surface profiles generated from AFM data are highly consistent with Figure 3.4 (b).

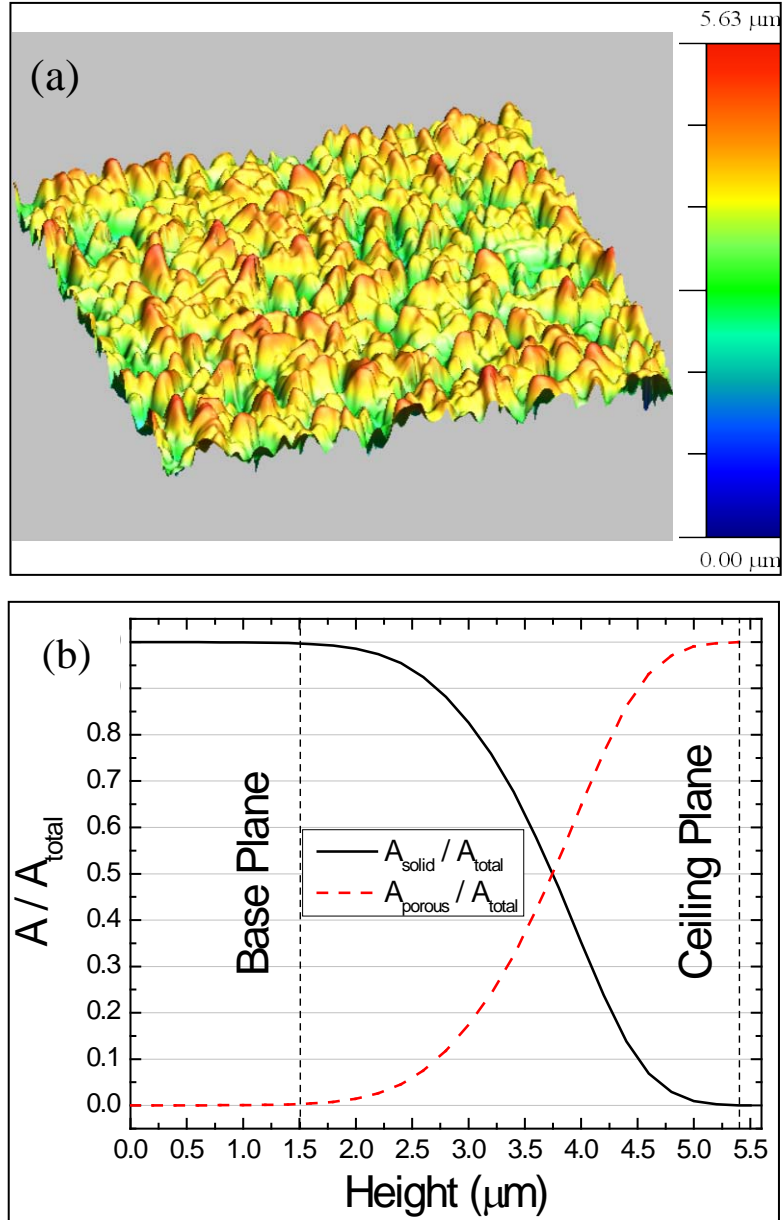


Figure 3.3: (a) Surface topography presented by 3D AFM scanning image of the fabricated IMC surface. Spatial scale bar is given on the right. (b) Area ratios between porous or solid domains and the total scanned area at various height levels.

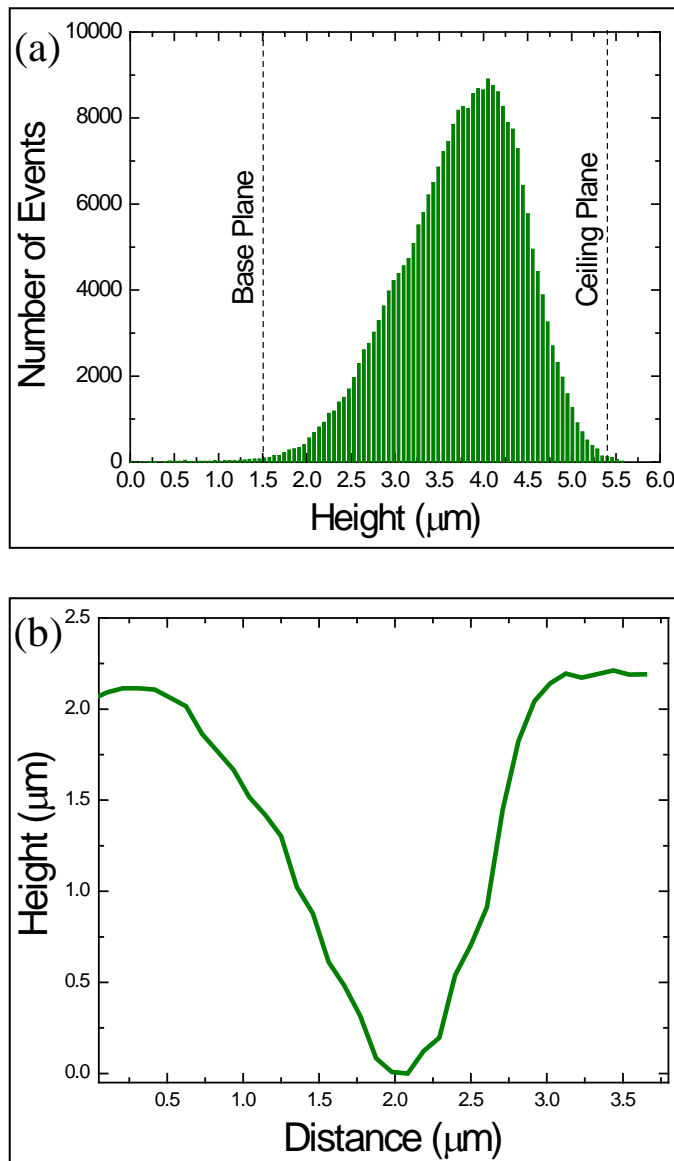


Figure 3.4: (a) Histogram for the height distribution of IMC topographic features. (b) A randomly selected surface profile showing cross section of a groove formed between Cn_6Sn_5 grains

3.2.3 Properties of Liquids, Contact Angle Measurements

Five organic liquids (purchased from Fisher Scientific International, Inc., as listed in Table 3.2) with different surface tension to viscosity ratios were chosen to be used for the study of the capillary rise over IMC0 rough surfaces. In Table 3.2, the properties such as boiling point, surface tension and viscosity of each organic liquid are collected (Landesberg, 2004). Properties are estimated at the room temperature which is measured to be around 25 °C, significantly lower (40 – 230 °C) than the liquid/vapor phase change temperature of selected organic liquids at the environmental pressure of 1 atm.

Table 3.3: Properties of liquids (Data collected from (Landesberg, 2004))

Liquids	Molecular Formula	Boiling Point (°C)	Surface Tension γ (mN/m)	Dynamic Viscosity μ (mPa·s)	γ/μ Ratios (m/s)	Apparent Advancing Contact Angle θ^*
2-Butanol	C ₄ H ₁₀ O	99.6	23.5	3.9	6.0	4.7
2-Propanol	C ₃ H ₈ O	82.4	20.9	2.0	10.7	4.5
Tetradecane	C ₁₄ H ₃₀	253.0	26.4	2.1	12.4	4.4
Dodecane	C ₁₂ H ₂₆	216.2	24.9	1.4	18.1	4.2
Methanol	CH ₄ O	64.7	22.1	0.5	40.9	3.6

The apparent advancing contact angles of these five liquids observed on the fabricated rough IMC surface were experimentally determined in order to support the calculation associated with the established model of the capillary rise. Advancing contact angles were recorded during the spreading of liquids over a rough IMC0 surface by using an optical contact-angle measuring device [OCA-15 LHT; HTFC 1200; DataPhysics Instruments GmbH, Germany] with the SCA software. The IMC rough surface was positioned horizontally on the measuring plate of the OCA device.

Note that the Bond number associated with selected liquids was very small ($\sim 2.1 \times 10^{-9} - 2.7 \times 10^{-9}$), so the gravity impact is negligible, see for the details regarding this argument the “Theoretical Model” section and explained in Appendix A. A drop of each liquid listed in Table 3.1, with a diameter of ~ 0.15 mm, was generated by a syringe (with a diameter of 0.015 mm) and released onto the horizontal IMC surface. The subsequent spreading of the resulting liquid drop monitored from the side was recorded by the high performance digital camera (DC) of the OCA device with a magnification of 40 \times . We declare as an advancing contact angle a contact angle at an arbitrary instant of time during the triple line movement. The recorded movie is subsequently decomposed into individual instantaneous frames. Then, a randomly selected, an image featuring the advancing contact angle was extracted from the recorded movie, one for each of the five organic liquids. After each measurement, the IMC substrate was ultrasonically cleaned by ethanol and dried with compressed air. The contact angle of each liquid was measured with the Image-Pro Plus[®] software for four independent tests. The average values of the measured data, with an average standard deviation of 0.7, are presented in the rightmost column in Table 1.

Figure 3.5 offers a set of selected images that illustrate the advancing contact angle of each organic liquid. The white dashed line in Figure 3.5 indicates the top interface of the IMC rough surface, located horizontally.

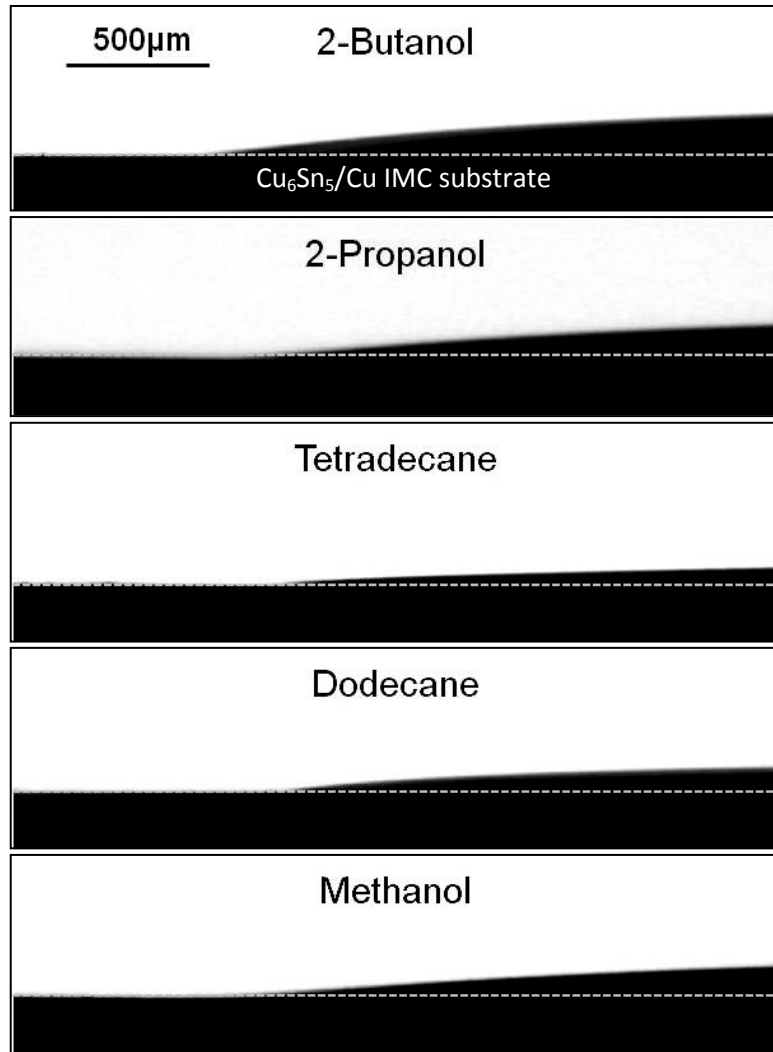


Figure 3.5: Measurement of apparent advancing contact angle of liquids on the rough IMC surface with a magnification of $40\times$ (A bar of $50\mu\text{m}$ is indicated in the figure)

3.2.4 Capillary Rise of Liquids through the IMC Rough Surface: Experimental

Data

After defining the characteristic parameters for the substrate and the contact angle during spreading, a series of tests involving liquid capillary rise over a vertical substrate has been facilitated. In this section we describe the experimental procedure followed and discuss the results obtained.

Figure 3.6 shows a schematic of the experimental setup for a study of the capillary rise over an IMC rough surface. The movement of the fabricated IMC plate is controlled by a translation stage. A distance scale is fixed in the plane of IMC, for an identification of the spatial location of the spreading front. A massive steel rack is used to hold the translation stage.

A liquid specimen was contained within a transparent glass chamber (\emptyset 27.5 mm \times 57.5 mm) whose top opening was sealed with a plastic foil sheet. A 10 mm slot was cut through the plastic sheet and the IMC plate was inserted into the container. Such configuration preserves an intended confinement of the spreading domain within the sealed chamber so that any excessive evaporation would be eliminated and its effects significantly reduced. A high performance Nikon digital camera was used to capture the close-up video of the capillary rise of liquids over the IMC surface with a frame rate of 30 frames/s.

As illustrated in Figure 3.7, the wicked area is clearly distinguished by a dark gray domain in the image sequence, extracted from an associated movie, so that a determination of the front location denoted as $z(t)$ can rigorously be executed. Locations

of the front were processed by Image-Pro Plus[®] software with an uncertainty of determining the linear dimensions smaller than 3%.

For each liquid, three videos were made, decomposed frames had been analyzed and the triple line locations measured. The standard deviation of the capillary rise rates for all tests is within the range of 0.01 to 0.05 mm/s^{1/2} in a “spreading distance vs. time square root” scale, based on multiple measurements for each liquid. This small margin strongly verifies reproducibility of the capillary rise data.

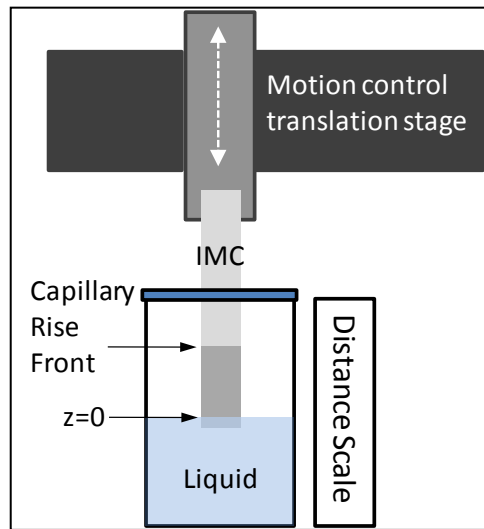


Figure 3.6. Experimental configuration for capillary rise upward an IMC rough surface

Note that the liquid wicking studied was rigorously constrained to the space domain of the experimental chamber (the triple line position at any instant of time had been within the field of vision inside the transparent chamber, to eliminate possible impact of evaporation that would take place if the triple line would propagate beyond this domain, see Figure 3.7). All data points for the triple line location vs. time were taken only while the triple line propagated within the experimental chamber. In this study, we focus on modeling of the time evolution of the capillary rise (location z vs. time t).

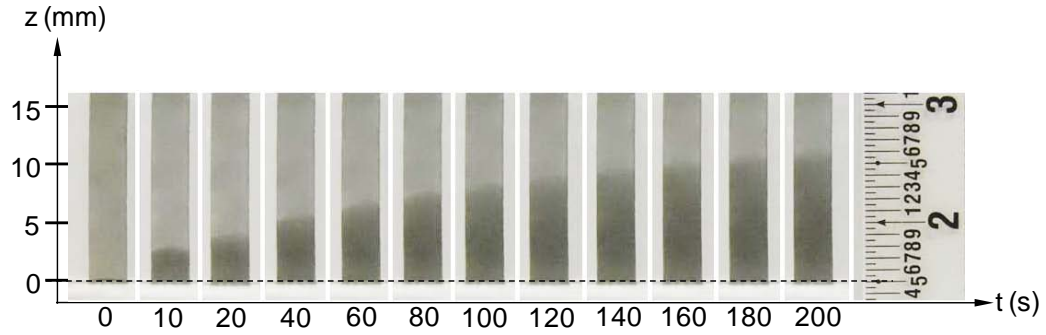


Figure 3.7: Image sequence of capillary rise fronts of Tetradecane wicking over an IMC surface (0 – 200 seconds)

The triple line front is not necessarily horizontal across the width of the IMC strip due to (i) the possible non-homogenous distribution of the surface grain field, which is dictated by the nature of the IMC substrate formation, and the corresponding appearance of the random roughness; (ii) the edge effects caused by the actual physical conditions imposed at the edges of IMC substrates. In addition, topographical features on edges of IMC substrate were influenced by cutting. So, the liquid front position at its edges may slightly differ from the front locations in the middle of the observed domain. However, measurements of the front location $z(t)$ were always conducted at a central location, i.e., within the surface strip middle domain. So, we have adopted an assumption that the edge effects would not be considered, effectively eliminating an impact of this deviation.

The primary meniscus height z_0 (indicated in Figure 3.8) is experimentally determined to be, in average, 0.7 ± 0.2 mm for all five organic liquids. For measurements of the capillary height of all the liquids, z_0 and the associated onset of time measurement, t , are assumed to represent the reference, starting point at the onset of observation ($@t = 0, z_0 = 0$ mm, see Figure 3.6, and in more detail, Figure 3.8). The one-to-one correlation between instantaneous front locations and time was, as elaborated earlier, established by

the decomposition of the real time digital imaging of the front performed *in situ*. So, among the decomposed frames, the one with an initial formation of the primary meniscus height was chosen to set the reference point. In the subsequent frames, wicking could be noticed clearly because the soaked area has a much darker appearance than the primary meniscus domain. The distinction between the meniscus area and the wicking area are generated from such a pixels contrast.

3.3 Theoretical Model

The objective was to predict evolution of the capillary front movement, i.e., to describe the kinetics of the wicking front for a set of liquids over the pre-fabricated rough surface. The assumptions are as follows.

1. Liquid properties (i.e., density, viscosity and surface tension) are constant during the wicking process.
2. The IMC surface is considered as being spatially isotropic. Similar type of an IMC surface leads to a perfectly uniform spreading of molten metal (Zhao et al., 2009a).
3. The gravity force impact versus surface tension and viscosity forces is neglected. The Bond number associated with organic liquids in Table 3.3 is assessed as:
$$Bo = \rho g (V/A)^2 / \gamma \cong (2.1-2.7) \times 10^{-9}$$
 (See Appendix A)
4. An impact of evaporation of the organic liquids is negligible, minimized by design of the experimental setup (a nearly saturated liquid vapor atmosphere in the experimental chamber). Moreover, the boiling points of all organic liquids used in the tests are 40 – 230 °C higher than the room temperature (~25 °C). (Note

that the evaporation rate is determined, for an equivalent area of IMC3 substrate used in tests at room temperature, to be $\sim 1.9 \times 10^{-6}$ g / s for a methanol which is the liquid with the lowest boiling point in this study. Such an evaporation rate is for an order of magnitude smaller than the wicking rate of the liquid ($\sim 3.5 \times 10^{-5}$ g / s), so the evaporation of liquids is considered as negligible.)

Liquid mass at the source is abundant (an infinitely large liquid source). The volume of the liquid bath in the glass container was $\sim (13 - 15) \times 10^3$ mm³, hence for ~ 5 orders of magnitude larger than the available total wicking void volume on the IMC surface ~ 0.06 mm³.

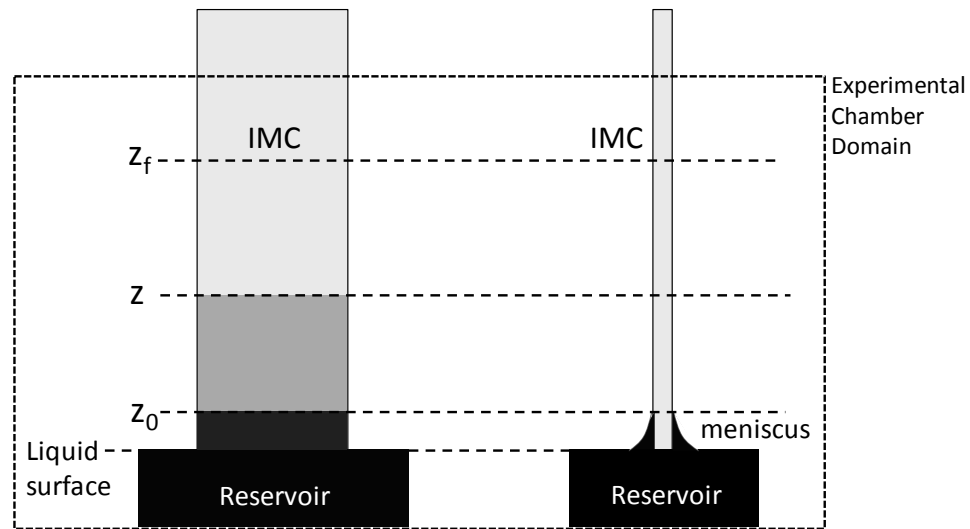


Figure 3.8: Model of the macro configuration of capillary wicking upward a rough IMC surface

Figure 3.8 shows schematically a configuration of the capillary wicking upward a rough IMC surface. Wicking of liquid through surface roughness begins at the location $z_0 = 0$ which is right above the triple line of the free surface meniscus. z_f is the final location where the wicking terminates. z is an arbitrary location between z_0 and z_f . As indicated on Page 24, the height of the primary location of the triple line of the meniscus z_0 is determined to be 0.7 mm with a standard deviation of 0.2 mm above the liquid surfaces for all five studied liquids.

The velocity field should be consistent with the Darcy's Law implemented for the liquids within the rough/porous domain of the rough surface, (Bejan, 2004; De Wiest et al., 1969; Scheidegger, 1974)

$$\mathbf{v} = -\frac{1}{\mu}[\mathbf{K} \cdot \nabla p] \quad (3.1)$$

where \mathbf{v} is the velocity vector, μ is the dynamic viscosity of the liquid, and \mathbf{K} is an intrinsic permeability tensor, see Section 2.3 in Chapter 2 (De Wiest et al., 1969; Scheidegger, 1974), of the porous medium exposed to liquids featuring the pressure gradient ∇p associated with the flow path and capillary effect.

For a 1-D planar flow configuration, a velocity scalar u , taken from the associated velocity vector, is of interest. The second order permeability tensor will also be reduced to a scalar for the planar IMC1 surface due to the 1-D configuration and the isotropic nature of the roughness domain of IMC1. Therefore the velocity of liquid at a location z can be expressed in a scalar form as, (De Wiest et al., 1969; Scheidegger, 1974)

$$u = \frac{k}{\mu} \left(-\frac{dp}{dz} \right) \quad (3.2)$$

where k is an effective scalar intrinsic (specific) permeability of the rough surface

The velocity of liquid while it flows through a location z at the corresponding instant of time t is expressed, by definition, as

$$u = \frac{d(\tau z)}{dt} \quad (3.3)$$

The product (τz) in Equation (3.2), which is associated with an arbitrary location z , is the real path of organic liquids flowing through IMC surface roughness, τ is the tortuosity of the IMC rough surface (Epstein, 1989; Boving and Grathwohl, 2001), which is defined as the ratio of the real distance between two points and the associated shortest linear length. The details about tortuosity are introduced later on Page 72 and in Appendix F.

The expressions for velocities in Equations (3.2) and (3.3) both represent the velocity associated with the same random location $z(t)$. Therefore the equality of both will lead to

$$\frac{d(\tau z)}{dt} = \frac{k}{\mu} \left(-\frac{dp}{dz} \right) \quad (3.4)$$

The capillary pressure is defined as the ratio of driving pressure force to the exerted area and by definition can be written as

$$\Delta p = \frac{F_\gamma}{A(\alpha, \theta)} \quad (3.5)$$

where $A(\alpha, \theta)$ represents the cross sectional area of the liquid occupied in a groove with a consideration of the free surface curve of the liquid caused by the surface tension. F_γ represents the capillary force exerted on a liquid associated with $A(\alpha, \theta)$.

The pressure gradient at the location z in equation (3.4) is assumed to be approximated for the physical domain of spreading as

$$-\left. \frac{dp}{dz} \right|_z \sim \frac{\Delta p}{\tau z} \quad (3.6)$$

The integration of Equation (3.4), with expressions given in Equations (3.5) and (3.6) inserted, with respect to time from $t = 0$ to t across the domain of spreading from $z_0 = 0$ to z leads to

$$z^2 = \frac{2k}{\tau^2 \mu} \frac{F_\gamma}{A(\alpha, \theta)} t \quad (3.7)$$

where, as defined above for Equation (3.5), $A(\alpha, \theta)$ and F_γ respectively, are the cross sectional area of the V-groove and the capillary force effected on the cross sectional area.

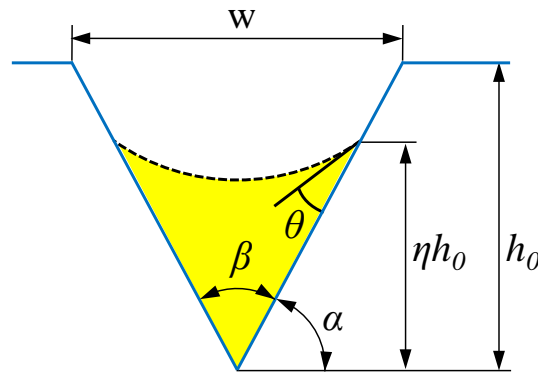


Figure 3.9: Geometric Details of Cross sections of V- Groove

Geometrical details of a V-groove model are given in Figure 3.9. Note that w is the width of the groove, h_0 is the height of the surface groove and (ηh_0) is the vertical distance between the groove bottom and the triple line of the liquid within the groove. We introduce η as the filling factor as a new variable, which is defined as the ratio of the actual liquid height in a groove to the groove height h_0 , see Appendix G.

Expressions for $A(\alpha, \theta)$ and F_γ , for a V-shaped groove, as Equation (3.8) and (3.9), are reported in details by Rye et al (Rye et al., 1996). As we consider a channel between grains as a single V-shaped groove which has the same geometrical features, it is appropriate in this study to utilize the expressions for $A(\alpha, \theta)$ and F_γ derived by Yost et al.

$$A(\alpha, \theta) = (\eta h_0)^2 \frac{\sin^2(\alpha - \theta) \tan(\alpha) - (\alpha - \theta) + \sin(\alpha - \theta) \cos(\alpha - \theta)}{\tan^2(\alpha) \sin^2(\alpha - \theta)} \quad (3.8)$$

$$F_\gamma = \frac{2(\eta h_0)\gamma}{\sin(\alpha)} \left[\cos(\theta) - \frac{(\alpha - \theta) \cos(\alpha)}{\sin(\alpha - \theta)} \right] \quad (3.9)$$

Note that α and β are groove angles for a V-groove and θ is the contact angle of a liquid in V-grooves. Note that the filling factor η will be parametrically introduced as a new empirical variable. Its modeling is important aspect of the process and will be discussed further in Chapter 5.

With the expressions for $A(\alpha, \theta)$ and F_γ of the V-groove, Equations (3.8) and (3.9), Equation (3.7) evolves into its final form. Equations (3.10) and (3.11) constitute the wicking model for the network of V-grooves. Note that this equation differs fundamentally from the Yost model because it is not valid for a single groove but for the

network of grooves forming the porosity of the hypothetical rough surface through the analogy of imbibing and flow through a porous medium defined by the given permeability. It can be noticed though that the moving front location z is proportional to the square root of the corresponding time, which is typical for a Washburn type model.

$$z^2 = \frac{4}{\eta h_0} \frac{k}{\tau^2} \frac{\gamma}{\mu} G(\alpha, \theta) t \quad (3.10)$$

where

$$G(\alpha, \theta) = \frac{\left[\cos(\theta) - \frac{(\alpha - \theta) \cos(\alpha)}{\sin(\alpha - \theta)} \right] \tan^2(\alpha) \sin^2(\alpha - \theta)}{\sin(\alpha) \left[\sin^2(\alpha - \theta) \tan(\alpha) - (\alpha - \theta) + \sin(\alpha - \theta) \cos(\alpha - \theta) \right]} \quad (3.11)$$

In Equation (3.10), (σ/μ) is the surface tension to viscosity ratio for liquids listed in Table 1. $G_I(\alpha, \theta)$ is dimensionless, and it is a function of geometry of the V-shaped groove (the basic geometric feature of the resulting network in addition to the permeability) as well as the contact angle θ .

The permeability is defined by Hubbert and Willis (Hubbert and Willis, 1957), see Appendix F:

$$k_{theor} = \frac{\varepsilon}{6} \left(\frac{2\varepsilon}{B} \right)^2 \quad (3.12)$$

where ε is the porosity; B is the ratio of the total surface area of all the voids throughout the porous medium to the total volume of the porous medium. Note that the surface porosity ε is defined as the ratio of the porous volume within a rough surface domain to

the total volume of a rough surface, $\varepsilon = V_{porous} / V_{total}$ (De Wiest et al., 1969; Scheidegger, 1974). As suggested in (Hubbert and Willis, 1957), B can be expressed by definition for a rough surface as

$$B = \frac{A_{surface}}{h_0 A_{projected}} = \frac{r}{h_0} \quad (3.13)$$

where r is the surface roughness defined in the surface characterization section on Page 53 and in Section 2.1.4.1 in Chapter 2.

The relation between porosity and tortuosity, (Epstein, 1989), is given as, (Boving et al., 2001)

$$\tau = \varepsilon^{-1.2} \quad (3.14)$$

The relation presented in Equation (3.14) was established by performing a curve fitting of the experimental data for porosity vs. tortuosity for selected material systems (Boving et al., 2001). The assumed analogy between tested materials in (Boving et al., 2001) and IMC porous surfaces (a close proximity of the orders of magnitude of the permeability and pore size) allows us to estimate tortuosity with a known porosity by using Equation (3.14). In this study authors treated IMC rough surface as a porous domain which features micro-size structures and channels, with a permeability of the order of magnitude of 10^{-13} m^2 and with an equivalent pore size of $\sim 1.5 \text{ }\mu\text{m}$. Data in (Boving et al., 2001) were verified against the experiments with a porous limestone and sandstone (a different material), but with a wide range of permeability with the order of magnitude of from 10^{-8} to 10^{-12} m^2 and pore sizes of $\sim 0.1 \text{ }\mu\text{m}$. We found this set of data sufficiently appropriate to verify the general correlation between the porosity and

tortuosity vs. the assumed analogy. That specific statement in the previous sentence is supported by the facts that (i) similar porous nature of the studied domain, (ii) the same definition of the permeability, and (iii) the close proximity of the orders of magnitude of pore dimensions ($\sim 1.5 \mu\text{m}$ vs. $\sim 0.1 \mu\text{m}$) and permeability values ($10^{-8} - 10^{-12} \text{ m}^2 \text{ Vs. } 10^{-13} \text{ m}^2$). So, we now stress explicitly that a hypothesis is adopted in using the relation described in Equation (3.14) as a suitable relationship between the porosity and the tortuosity. Excellent predictions generated from our theoretical model vs. empirical spreading data in the following section verify this hypothesis – in particular scaling for all the liquids.

With the measured average porosity $\varepsilon = 0.43$ with a standard deviation of 0.04 and average surface roughness $r = 1.24$ with a standard deviation of 0.03 (Section 3.2.2), the theoretically estimated permeability and tortuosity of the IMC surface are calculated, using the average value of porosity and surface roughness, to be $k = 1.69 \times 10^{-13} \text{ m}^2$ and $\tau = 2.73$, respectively. The AFM data show that the average height of the grooves within the porous domain on the surface is $2.2 \mu\text{m}$ with a standard deviation of $0.2 \mu\text{m}$. The width of the grooves was measured in total for 100 different grooves, on randomly selected different locations of surface profiles based on AFM data. The width of the grooves is determined to be $w = 2.7 \mu\text{m}$ in average, with a standard deviation of $0.7 \mu\text{m}$. Therefore, with the average groove height and width, the groove angle β of the V-groove model indicated in Figure 8, is determined to be ~ 63 degrees.

Contact angle θ of liquid in grooves, illustrated in Figure 3.9, is assumed to be equivalent to Young's equilibrium contact angle measured on a flat surface. The contact angle θ^* measured on IMC surface is actually an apparent contact angle over the rough

surface. As established for wetting a rough surface (Quere, 2008), a very small (close to 0) apparent contact angle θ^* is associated with a Young's contact angle $\theta \sim 0^\circ$. Therefore, in our case, for $\theta^* \sim 4^\circ$, measured on a rough surface already flooded with a liquid, it is reasonable to assume that $\theta = 0^\circ$ as well. The value of $G(\alpha, \theta)$ is determined to be 1.39 with $\alpha = 58.5^\circ$ and $\theta = 0$.

3.4 Results and Discussion

Figure 3.10 shows the kinetics data of all five liquids in a z vs. $t^{1/2}$ coordinate representation. The presented trend of data illustrates clearly that the wicking distance z is linear to the square root of time associated with the wicking process. This linear trend also verifies the relation between z and t given in the theoretically devised equation (6). The slope of a data set, in a z vs. $t^{1/2}$ scale, represents the rates ($\text{m/s}^{1/2}$) at which a liquid penetrates the porous IMC0 surface. The z vs. $t^{1/2}$ slopes become smaller with the descending surface tension to viscosity ratios, Table 3.1.

Figure 3.11 shows the appropriately scaled kinetics data of all five liquids in a $\log(z)$ vs. $\log[(\sigma t/\mu)^{1/2}]$ coordinate system. The time is scaled with the surface tension to viscosity ratios. All the data collapse into a single line which means the scaling of the time with (σ/μ) eliminates the wicking behavior of differing fluids differences (expressed through different surface tension/viscosity ratios). The different liquids on the same substrate are exposed to the same geometric features of an IMC surface composed of a network of V-grooves, i.e., to the same average groove height h_0 and groove angle α . The filling factor η , defined as the ratio of the actual liquid height to the groove height, theoretically should be within the range from 0 to 1.

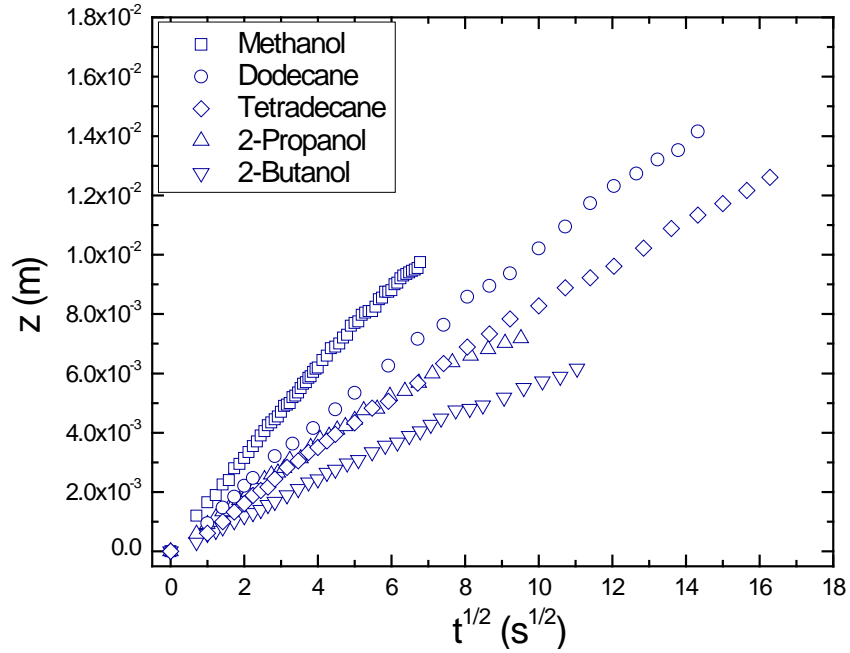


Figure 3.10: Kinetics data of liquids presented in z vs. $t^{1/2}$ coordinate

It was reported by Weislogel et al. (Weislogel et al., 1998) that, for a capillary rise in a single channel of a larger scale than in our experiments, the liquid height in a channel (which is equivalent to filling factor discussed in this chapter) will become constant after a short period of time, i.e., $t \sim 1$ s (for a channel with an approximate height and length of the order of magnitude of $\sim 10^1 - 10^2$ mm). That result also agrees with our experimental data and the theoretical model: the linear relation for $t^{1/2}$ and z shown in Figure 3.10, equation (6), indicates a constant slope for each liquid. Therefore, for the wicking phenomenon studied here, within the time period of the order of magnitude of $\sim 10^0 - 10^2$ seconds, the filling factor keeps unchanged for each of all five liquids. This argument is phenomenological and requires further consideration and empirical verification, beyond the scope of our inquiry at this instance.

Moreover, in this study, the available liquid used for the wicking process is unlimited in volume at the source, and the Bond number is small, so the filling factor is expected to be near 1. The collapse of all the data, Figure 3.11, implies that all liquids penetrate the IMC surface under the same filling condition, which means, for a given IMC porous surface fabricated in this study, the filling factor η is nearly the same constant which is within a range of $\sim 0.9 - 1.0$. The parametrical dependence on its value is presented in Figure 3.11, clearly indicating all data collapse for a high filling factor around 0.9.

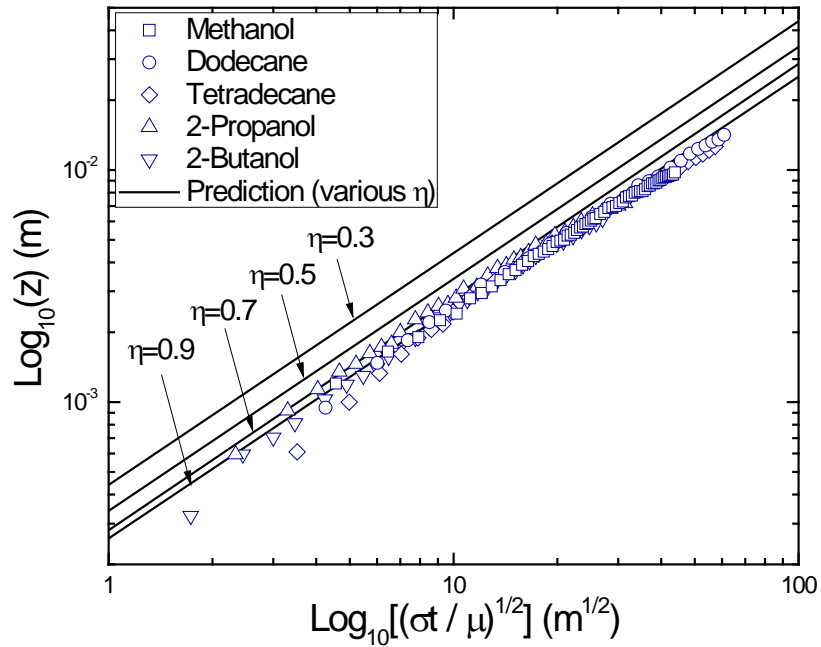


Figure 3.11: Kinetics data of liquids in presented with a scaled time $(\sigma t/\mu)^{1/2}$

The predictions from Equation (3.10) with hypothetically assumed different filling factors along with scaled kinetics data are presented in Figure 3.12.

The model gives accurate predication only as the filling factor is considered to be close to unity (a real situation). With $\eta = 0.9$, the agreement between theoretical

prediction and experimental data in Figure 3.12 appears to be very good. The average relative error of the theoretical prediction against experimental data is within the range from 4% to 8% (average 6% with a deviation of $\pm 2\%$) for all five liquids. With $\eta = 1.0$, the prediction agrees well with the experimental data, with an average relative error from 3% to 12% (an average 6% with a deviation of $\pm 4\%$).

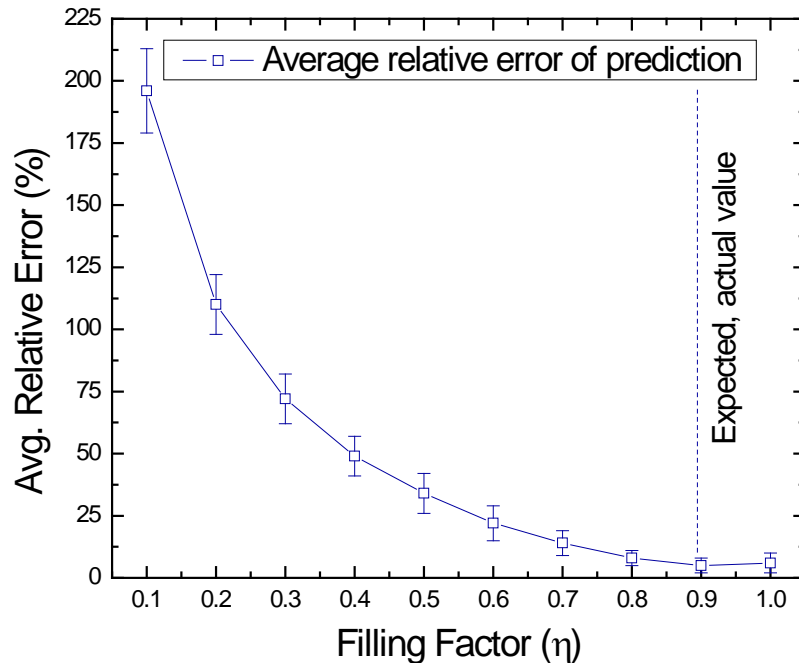


Figure 3.12: Average relative errors of theoretical prediction with various filling conditions

3.5 Summary

In this chapter, a theoretical model for wicking upward a rough surface in a planar fashion has been established by treating the rough IMC0 surface as a two dimensional porous medium featuring a network of open micro triangular grooves. The model is verified against experimental data.

Topographic features of an in house fabricated $\text{Cu}_6\text{Sn}_5/\text{Cu}$ intermetallic substrate with a surface roughness composed of non-uniform surface structures (but distributed uniformly and interpreted in terms of surface porosity and surface roughness) has been experimentally determined by Atomic Force Microscopy and optical surface profiling. The wicking kinetics of a set of selected liquids over rough surfaces, in absence of chemical reactions and with a negligible gravity influence, is described by a theoretically established model of a Washburn type. The model is expressed in terms of (i) the surface topography (i.e., permeability, tortuosity/porosity and geometry of micro-channel cross section); (ii) wicking features (i.e., contact angle and filling factor); and (iii) physical properties of liquids (i.e., surface tension and viscosity). An excellent agreement (with a relative error in the range of 4% to 8%) between theoretical prediction and experimental data, both of which show a z vs. $t^{1/2}$ relation, verifies the validity of the theoretical model. Scaled data indicate that for a specific rough surface, wicking kinetics of considered liquids depends on surface tension to viscosity ratios, and the formed equilibrium contact angles.

This study offers a practical simple method which can be used to analyze wicking kinetics of liquids over a surface with non-uniform micro size surface features but homogeneously distributed along the interface. Note that the topographic features of IMC

rough surfaces is characterized as a surface porosity and surface roughness experimentally by 3D surface profiling and AFM if the roughness is random, i.e., IMC0. Filling factor, in this case a constant, is the only empirical input for the theoretical model. It is found that the filling factor is the same for all five organic liquids for the analyzed IMC rough surfaces. With the topographic information acquired, analytically established model gives a prediction of the wicking kinetics of liquids over associated surfaces with a small relative deviation. Such a theoretical model will provide a theoretical framework for the studies Chapter 4 and 5 which deal with the spreading of molten solders on rough surfaces at elevated temperatures.

CHAPTER 4: CAPILLARY DRIVEN MOLTEN METAL FLOW OVER TOPOGRAPHICALLY COMPLEX SUBSTRATES[†]

4.1 Overview

This chapter focuses on phenomenological observation and analytical modeling of a radial spreading of molten solders (molten metal as opposed to organic liquids as presented earlier) on an intermetallic (IMC1) surface with a roughness composed of uniformly distributed grains. This work constitutes an effort to extend the approach advocated in Chapter 3 to a spreading of molten metal over substrates having similar topographic features. The chemical reaction has been minimized by using an intermetallic substrate consisting of a product of chemical reaction between the solder and the substrate.

The theoretical model of a capillary driven flow of liquid metal through topography features of rough surfaces has been verified by a study of molten solder alloy (Sn-Pb) spreading over $\text{Cu}_6\text{Sn}_5/\text{Cu}_3\text{Sn}/\text{Cu}$ IMC substrates. Flow through micro grooves over a rough IMC substrate is considered as a spreading through an isotropic two-dimensional porous medium featuring a network of open micro-grooves having pre-defined free-flow area cross sections. The relative margin of deviation between theoretically predicted and empirically determined locus of points of triple line locations is within the range of 5%-15%. This margin is considered as sufficiently small, hence it supports validity of the developed, analytically formulated square root power law model for a whole spreading domain. This law is presented in terms of (i) the geometry of topographical features of the rough surface (i.e., effective intrinsic permeability,

[†] This chapter includes detailed account of material summarized in *Langmuir* (2011), Vol. 27(23), pp. 14260 – 14266

porosity/tortuosity, and micro channel cross-section geometry, for definition of these quantities see Appendix F, G and Section 3.3 in Chapter 3), (ii) wetting/spreading features (equilibrium contact angle and filling factor), and (iii) molten metal/substrate properties (viscosity and surface tension). Experimental data involving triple line kinetics represent the data set of locations of the triple line vs. time obtained by *in situ* monitoring of the spreading of molten metal systems over IMC substrates by using the controlled atmosphere hot stage microscopy.

The triple line driven by surface tension and retarded by viscosity, in the absence of gravity (the assumption of the negligible gravity influence is discussed and justified on page 98), in most cases is modeled by a square root of time relationship, what is fully in accord with the well accepted Washburn's Law (Washburn, 1921) for the flow through a capillary (but in absence of a reaction at the interface). Our interest is to explore whether a modeling of the surface tension driven spreading of liquid metal through the network of microgrooves of a rough non-reacting surface and in an absence of gravity influence, can also be based on a square root power law, and how the geometrical features of such a surface impact this spreading.

4.2 Problem Formulation

A surface tension driven flow of a molten metal micro layer over a metal surface is, as a rule, a reactive flow. For example, soldering processes involving tin (either lead or lead-free) alloys and copper substrates are associated with Sn-Cu reaction leading to a fast intermetallics formation (say Cu_6Sn_5 and/or Cu_3Sn over Cu). This reaction interferes strongly with the spreading process. However, to understand the sole impact of surface

geometry on spreading of such systems, a reaction may need to be suppressed. So, to eliminate reaction in a study of such a spreading or to argue sensing of a minimal impact of it, one may manufacture a substrate consisting of an intermetallic layer coating over the core substrate. Such a surface topography features a micro-size-scale scallop-like grain structure that is inherently rough and represents a substrate with randomly distributed inter-grain hills/valleys, forming a network of micro channels. Figure 4.1 offers SEM images of the surface and its cross-section.

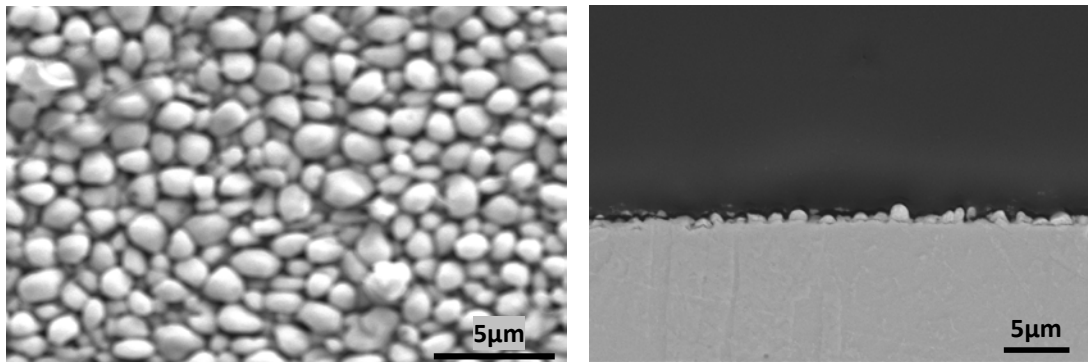


Figure 4.1: Surface topography of a $\text{Cu}_6\text{Sn}_5/\text{Cu}_3\text{Sn}/\text{Cu}$ (IMC-1) substrate

Such a surface (designated as IMC1), if used as a substrate for Sn-Pb spreading, represents an appropriate test bed for a study of the triple line (near reaction-free) kinetics over a rough surface. Figure 4.2 illustrates the sequence of a series of instantaneous frames made *in situ*, in real time, and during the spreading with a magnification of $20\times$ (see the next section for a description of the experimental procedure used to obtain the frame sequence).

The molten metal systems considered in this study were primarily lead-tin solders. Based on detailed real time *in situ* observation of the evolution of the process, it is established that the homogeneity of surface topography, featured by the network of micro

grooves, leads to an almost perfectly uniform spatial distribution spreading of liquid metal, see Figure 4.2. Note the source material in the center of the field of vision (within the white dotted line markings, the $t = 0$ s and $t = 1$ s frames) is feeding the network of grooves formed over the rough surface of the substrate. Over time, the molten material at its source is gradually exhausted. The through-the-grooves spreading front seen in Figure 4.2 (black dotted markings) is representing the location of the triple line, i.e., the front of the molten material is progressing through a maze of inter-connected surface grooves. The triple line velocity at a respective early instant of time for spreading over IMC1, is larger than for a lead-tin solder spreading over a virgin Cu substrate, (Liu et al., 2011b; Zhao et al., 2009a). We have studied in detail the lead-free solders spreading as well, see (Liu et al., 2011b; Zhao et al., 2009a), but modeling of the phenomenon presented here focuses on the former.

One may notice from Figure 4.2 that the rate at which the spreading radius increases becomes smaller approaching the termination of the spreading sequence. This rate change follows apparently a power-law trend in the spreading period that precedes the asymptotic phase (what is going to be the main subject of analytical modeling that follows). Note that the test indicated in Figure 4.2 is designated as Test 1 and the associated parameters are listed in Table 4.1. Heating cycle for this test is offered in Figure 4.4. More related experimental details are interpreted in Section 4.3.

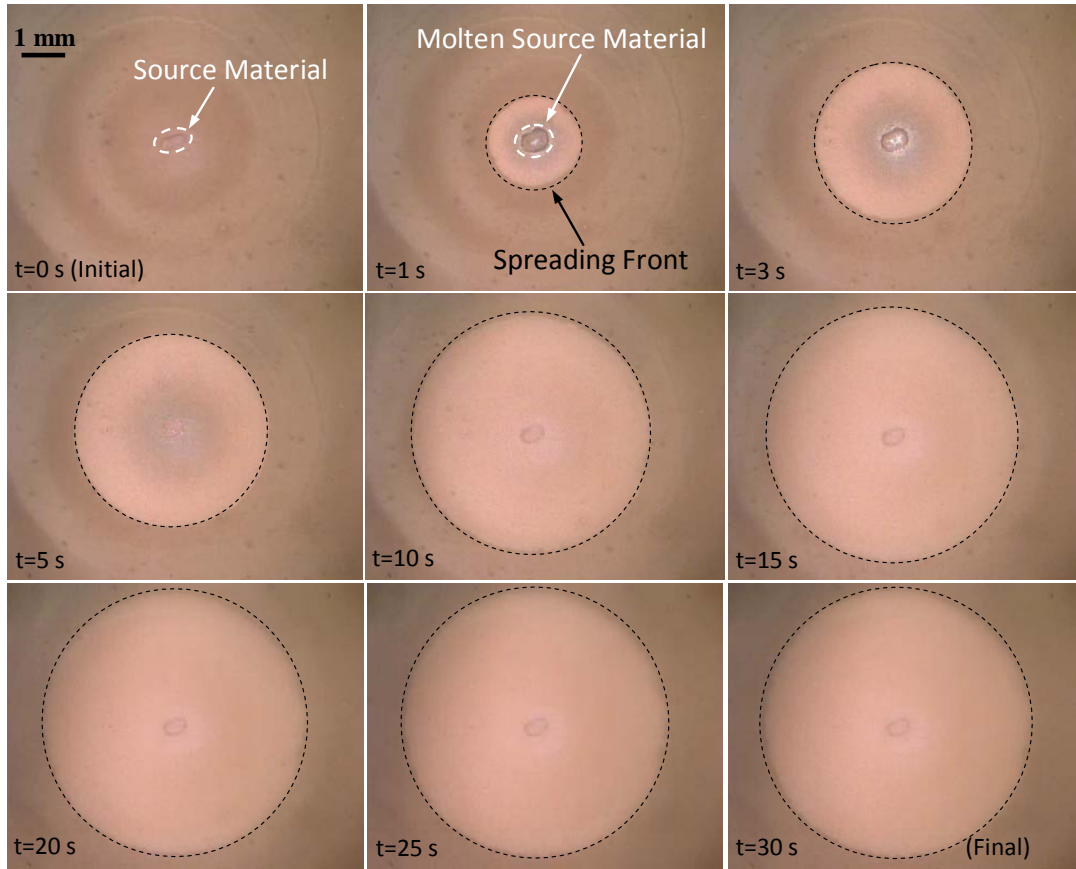
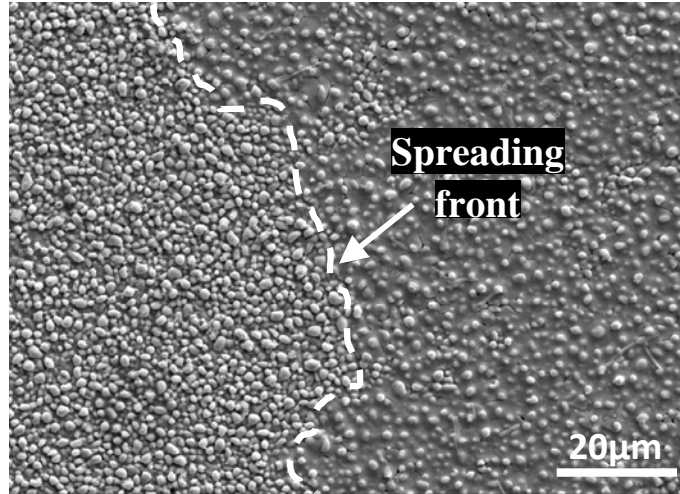
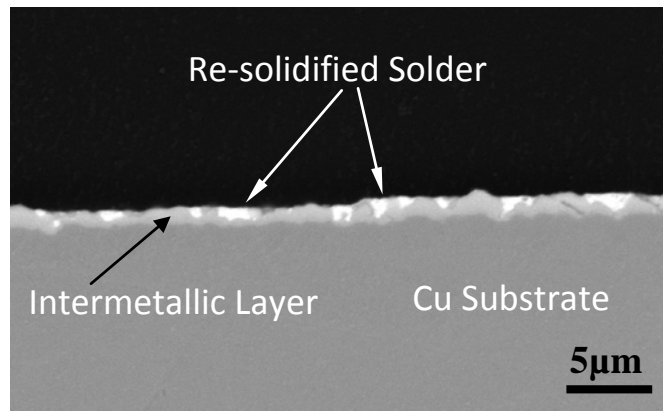


Figure 4.2: Instantaneous frames extracted from a real time in situ monitoring of Pb-Sn eutectic spreading over IMC1 ($\text{Cu}_6\text{Sn}_5/\text{Cu}_3\text{Sn}/\text{Cu}$) (Images associated with Test-2 in Table 4.1)

Figure 4.3 (a) offers an image of the domain at the edge of the spreading front. The white dotted line indicates the location of the spreading front of the triple line locus of points. It is easy to notice that the hills and valleys correspond to non-flooded and flooded surface roughness features, respectively, hence molten metal flows dominantly through the surface roughness features interpreted as the network of micro-grooves. Figure 4.3 (b) represents a SEM image of the cross section of a sample after solidification.



(a)



(b)

Figure 4.3: (a) SEM image at a location of the spreading front; (b) SEM image illustrates cross section of a sample after the test.

Our objective is to predict this spreading behavior, i.e., to correlate the triple line location with time. We are not necessarily interested only in fitting the empirical data with the adequate power law, rather we are interested in developing a theoretical model with a minimal input of empirical parameters. In the following sections, we present briefly the experimental procedure and data to be used in the model verification. Subsequently, we focus on building a model of spreading and its verification.

4.3 Materials and Experimental Procedures

The substrate used in this study is IMC1, the manufacturing process of which is described in details in Chapter 3. The so manufactured substrate IMC1 was exposed to an experimental procedure aimed at establishing the kinetics of liquid metal spreading over a rough surface but void of intense interface reactions. Solder material's solid state pellets of a specified mass (defined by the pellet size, i.e., its thickness and interface surface area were selected so that the solder mass at the onset of melting differs in subsequent tests). The equivalent radii are listed in Table 4.1, along with information about the extent of the ultimate spread at the onset of solidification. The equivalent radius is the radius of an equivalent circular interface surface area that corresponds to the actual non-circular area.

The hot stage microscopy was used to analyze kinetics of the triple line movement by monitoring in real time and decomposing digital movies into instantaneous frames. A substrate coupon having overall dimensions of 10 mm × 10 mm × 0.3 mm (or 0.5 mm) is positioned within the chamber of the LINKAM THMS 600 hot stage installed on an OLIMPUS BX51M optical microscope. A solder specimen was covered with a thin layer of RMA flux [EC-19S-8, Tamura Corp.]. The chamber was filled with ultra high purity N₂ (99.999%), after purging with nitrogen for 120 minutes before an initiation of the heating cycle. The purging has secured at least 30 chamber's volume replacements. Throughout the experiment execution, the steady stream of ultra high nitrogen was secured. The heating cycle consists of a ramp up, dwell and quench, as indicated in Figure 4.4. Note that tests studied in Chapter 5 were carried out with the same heating cycle as presented in Figure 4.4 (a). It is noticed that the spreading occurred under a non-isothermal condition, but in this study it is assumed that the properties of the liquid metal

keep constant within the specific small temperature range, as indicated in Figure 4.4, see Appendix D.

The heating ramp-up was specified as 100 K/min and the cooling ramp-down was 80 K/min. Temperature stability was specified at the level of 0.1 K. Verification of actual solder temperature was performed by comparing temperature readings for a given instant of time at the onset of melting, with the eutectic solder melting point temperature known. It is established that this temperature was recorded with a consistent bias (due to thermal contact resistance along the conductive path from the silver block heater to the solder pellet) of less than 7K at the 473 K temperature level. Correspondingly, temperature readings were corrected and the bias was eliminated. The series of thermal contact resistances includes (i) Ag heating block - quartz glass interface, (ii) quartz - glass - interface - substrate, and (iii) substrate-solder interface, in presence of flux. The peak temperature is set to be consistently 30K above the liquidus temperature of the corresponding solder.

Table 4.1: Substrate/solder sample sizes

Test No.	Solder	Area of IMC-1 substrate $A_s \times 10^6$	Initial thickness of the pellet $\delta_i \times 10^3$	Initial area of solder material $A_i \times 10^6$	Initial equiv. radius $r_0 \times 10^3$	Final area of solder material $A_f \times 10^6$	Final equiv. radius $r \times 10^3$
		(m ²)	(m)	(m ²)	(m)	(m ²)	(m)
1	Sn37Pb	100	0.05	0.11	0.188	27.45	2.956
2		100	0.05	0.13	0.204	31.12	3.147
3	Sn20Pb	100	0.05	0.23	0.270	34.35	3.306
4		100	0.05	0.28	0.297	35.31	3.353

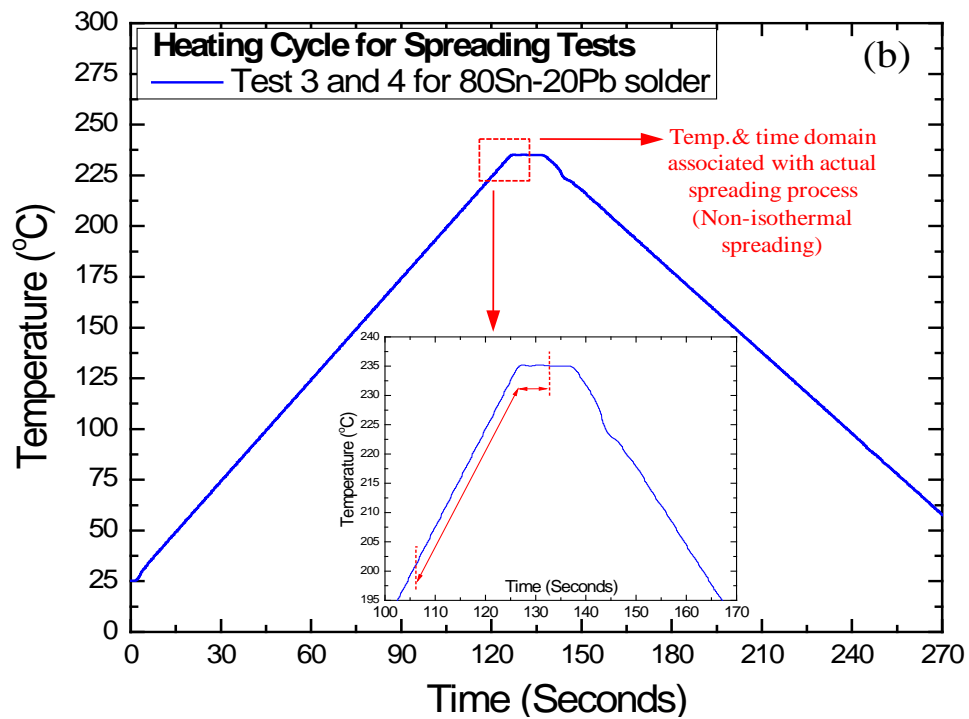
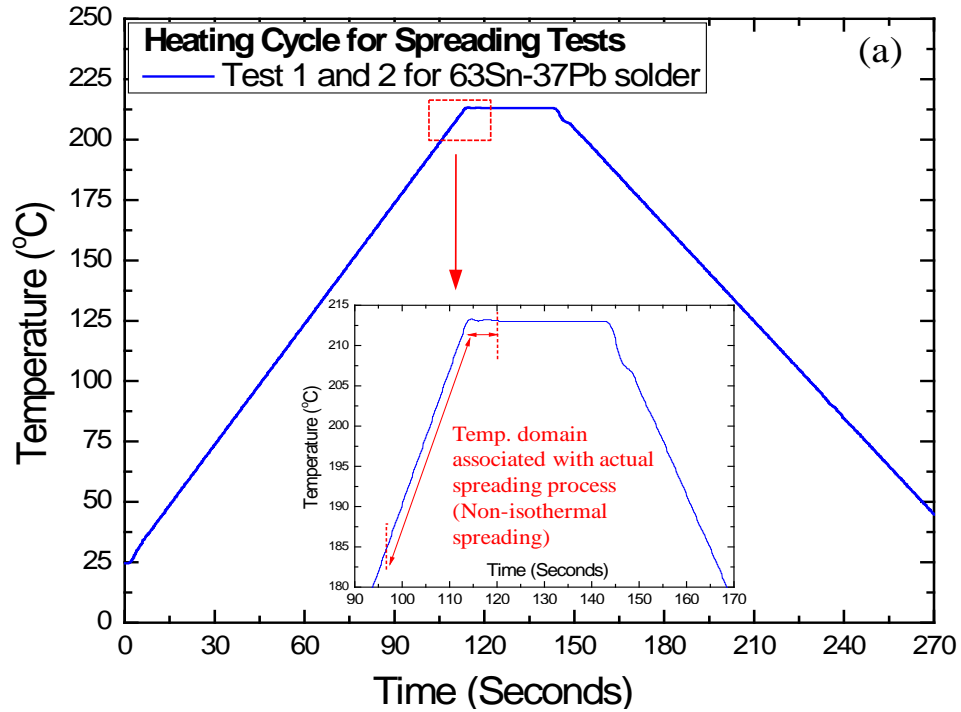


Figure 4.4: Heating cycle that consists of a ramp up, dwell and quench for spreading tests (a) for Test-1 and 2 for 63Sn-37Pb solder (b) Test-3 and 4 for 80Sn-20Pb solder. (Note that heating cycle in Figure 4.4 (a) is also used for tests studied in Chapter 5)

Figure 4.5 (a) offers a schematic of the hotstage microscopy system configuration indicating system components for heating, cooling, control, display and purging. Figure 4.5 (b) illustrates the hotstage microscopy setup located in the Brazing Research Laboratory of the University of Kentucky.

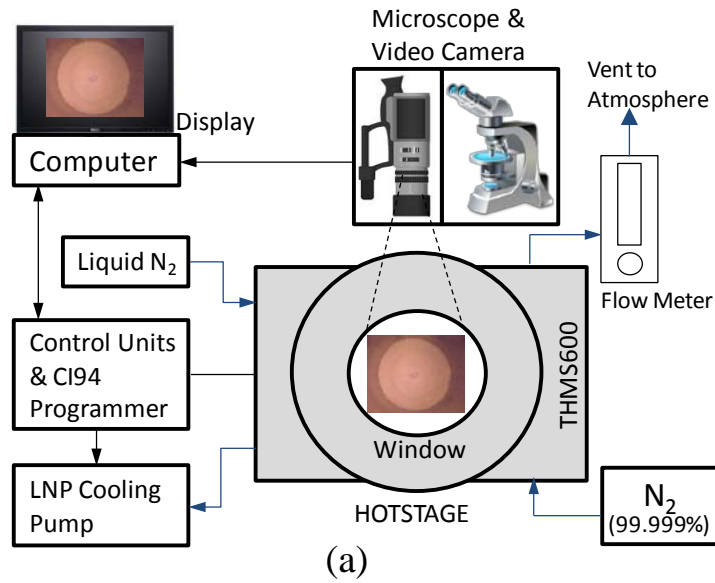


Figure 4.5: (a) Configuration of the hotstage microscopy system, (b) hotstage microscopy setup in the Brazing Research Laboratory of the University of Kentucky

During the heating/cooling cycle, digital imaging is performed with 22 frames/s digital camera system. Movie clips were digitally decomposed into individual frames and associated with digitally recorded corresponding substrate temperature histories. The spreading segment of an experiment evolves not at the constant peak temperature, but within the range of temperatures (in most experimental runs). It is assumed that the temperature dependence of thermo physical properties of the liquid phase is not significant to cause non-linear effects in the spreading behavior. The triple line was closely approximated with an instantaneous equivalent sessile drop perimeter locus of points (representing the solder spread perimeter). This was possible because upon a very short initial period of spreading controlled by inertia and surface tension, the triple line forms in the shape of a perfect circle if the substrate is characterized with uniformly distributed micro roughness topographic features. Measurements of the triple line locations were performed using Image-Pro PLUS® software. The uncertainty in determining linear dimensions was smaller than 3%. The uncertainty was estimated by comparing measurement results of the same test conducted by two independent readings using image processing software. Two randomly selected tests were used for uncertainty evaluations. Calibration of microscope readings was performed using a linear graduated micrometer with the pixel count within 10 μm half-division. The dwell at the constant peak temperature during spreading lasts for 120 seconds with initial phase experiencing the ramp-up rate of 100°C/min before reaching the plateau (solidification starts in average 100 seconds upon termination of the spreading observation period and the associated temperature is offered in Figure 4.4).

4.4 Experimental Results and Phenomenological Observations

Figure 4.6 shows the equivalent radius of the triple line location r vs. time t data for tests designated as Test-1 through Test-4, see Table 4.1. Temperature history of the heating cycle for all tests is offered in Figure 4.4. It can be noticed that each test features identical triple line kinetics profile trend: after initiation of the spreading and an initial hesitation of the liquid front, a fast ramp-up can be identified, followed by an asymptotic slow-down, and an ultimate spreading termination. Moreover, Figure 4.6 illustrates that if the initial solder material is more abundant (i.e., a larger initial liquid mass, See Table 4.1) the power relation domain will be maintained for a bit longer period of time, but the spreading will dominantly follow the power trend only during the central phase of spreading, not sizably influenced by the initial source mass. Test-1 has the least liquid source material, so it enters the final spreading stage first. Test-2 has more source material than Test-1 but less than test-3 and test-4, thus it goes into the final stage somewhat later. Test-3 and Test-4 maintain the power relation for the longest time as they have the largest source material available. So, one may conclude that the size of the initial mass did not change the character of spreading in the surface tension-viscosity trade-off domain, what would not be the case for the domain of the inertia-controlled start of spreading and the asymptotic decay at its end.

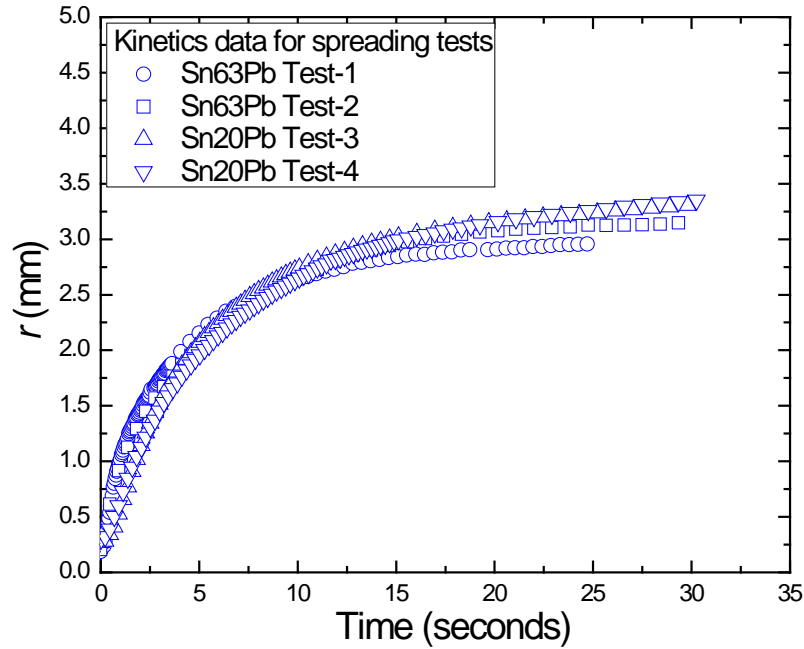


Figure 4.6: Time t vs. spreading front for Test-1, 2, 3 and 4

A large number of tests as illustrated by Figure 4.6 have been performed using IMC1, IMC2 and IMC3, with eutectic and non-eutectic Sn-Pb solders, as well as lead-free solders (Liu et al., 2011b; Zhao et al., 2009a). All lead solders have consistently featured similar trends as the ones presented here. It is established that the central, power law domain keeps dominantly linear r vs. $t^{1/2}$ dependence with an average adjusted R-square value of 0.979 (so, it is very well correlated). Note that the R-square provides a measure of how well future outcomes are likely to be predicted by a model (Steel and Torrie, 1960). These tests confirm the reproducibility of the discussed behavior; hence offer a reliable data base for model building of the triple line kinetics, an objective of this study to be presented next. In anticipating the analysis that will follow the model presentation, it should be noted that if a cubic power law instead of quadratic is heuristically adopted, empirical data may be correlated for a longer central surface

tension-viscosity time domain (extending into the asymptotic termination phase), but with a larger data deviation within it (see the discussion section later).

Based on these observations, one may conclude that the spreading process of a sessile drop on a rough surface having micro scallop-grain topography, such as Pb-Sn solders spreading on IMC1 surface, can be divided, in the first approximation, into three stages:

The initial stage influenced by inertial forces (Courbin et al., 2009) (may be assisted or not by the gravity force; in our case, the substrate surface is horizontal and gravity effect may not be included if the Bo number is small (see the justification under item 4 of the list of assumptions in Section 4.6 on building the theoretical model). This stage is very short compared to the whole process, it is essentially linear and characterized with a large slope (a fast, short lived stage). In this study this initial stage is about ~1 second compared to a whole spreading process of ~25-30 seconds. Moreover within this initial stage spreading is completed by up to 20% as the spreading radius is concerned.

The power-law stage: The relation between the spreading front and time obeys a certain power law (assumed to be a square root relation in this case, see the proof later, Equation (4.11)), but it may differ as has been well known from previous investigations of the same phenomenon over smooth non-reactive or weak reactive surfaces, following the balance of surface tension and viscosity forces and a suppressed impact of reactions. This stage is the main stage of spreading and covers a large portion of the whole process. Note the main stage in this study lasts up to about 11 ~13 seconds and covered up to 92% of the final spreading radius.

The final stage, featuring an asymptotic trend of spreading, diminishing slope impacted by diminishing liquid source's quantity (in the case over non-flooded surface roughness alterations) follows.

The focus of this chapter is on the power law stage which takes place roughly from 0.5~1-2 second into the spreading process and lasts up to a roughly 11~13 seconds into the spreading (that is, starting after about 20% of the final spreading radius is reached, up to ~92% of the final spreading radius), which apparently covers a large portion of the whole process. Our study does not involve modeling of the initial inertia vs. surface tension phase (Courbin et al., 2009) but focuses on the subsequent surface tension-viscosity phase. Our assessment obtained from empirical data on the spreading kinetics indicates, as stated above, the duration of the first phase of ~ 1-2 s, as indicated earlier, i.e., at least an order of magnitude shorter than the central, considered phase. The prediction of the initial phase duration in a spreading process was studied earlier for some spreading settings, e.g. a released sessile drop spreading over a flat non-reactive surface (Biance et al., 2004; Seveno et al., 2009), but for a different physical situation (a wetting balance configuration instead of sessile drop setup in this study) and will not be included in this chapter. Modeling of the initial spreading phase for the configuration considered in this study still waits for a solution. We should indicate that spreading over the flat surfaces, as well as various patterned surfaces, and in particular over surfaces with a reaction at the solid/liquid interface, may feature more than three distinct stages (Cazabat et al., 1986; Dezellus et al., 2003). The study presented here corresponds to a spreading through the network of micro-groves, featuring a scallop grain micro-pattern (rarely studied) – as opposed to spreading over rough surfaces where roughness alterations are

fully flooded. Time measurement is determined with uncertainty smaller than 10^{-3} s, at least three orders of magnitude smaller than the time scale of the spreading process evolution considered, $O(10^0-10^1)$ s).

4.5 Characterization of the Surface Topography

The IMC1 surface, Figures 4.1 and 4.7 (a), has a complex scallop-shape (see also Figures 4.7(c) and 4.3(a)), and represents a porous-like 3-D topographical domain. To simplify its features in an attempt to build a model that can be well deterministically related to micro channels topographic features, we intend to regularize the grains shape by using an a priori selected surface structure. A surface patterned with the compact package of regular hexagonal elements which simulate the grains has been selected to represent such simplified topography, Figure 4.7 (b). The lateral sides of hexagonal elements form a series of triangular grooves, Figure 4.7 (c) and (d). All topographic elements of the same kind are in the first approximation considered to be the same. The bottom and lateral sides of each hexagonal element are, based on a SEM characterization of the real surface, see Figure 4.1, approximated to be $O(100 \mu\text{m})$. To prove the validity of this regularization of the surface topography, systematic measurements of grain sizes across the spreading domain were conducted at multiple randomly selected locations. A total of 150 individual grains of an IMC1 surface have been considered within the field of vision of $115 \mu\text{m} \times 84 \mu\text{m}$ and at a magnification of $1000\times$. The average equivalent radius of the measured grains is $1.1 \mu\text{m}$ with a standard deviation of $0.23 \mu\text{m}$. Moreover, the equivalent radius of 70% of all the measured grains falls within the range between $0.75 \mu\text{m}$ and $1.25 \mu\text{m}$, see Appendix C.

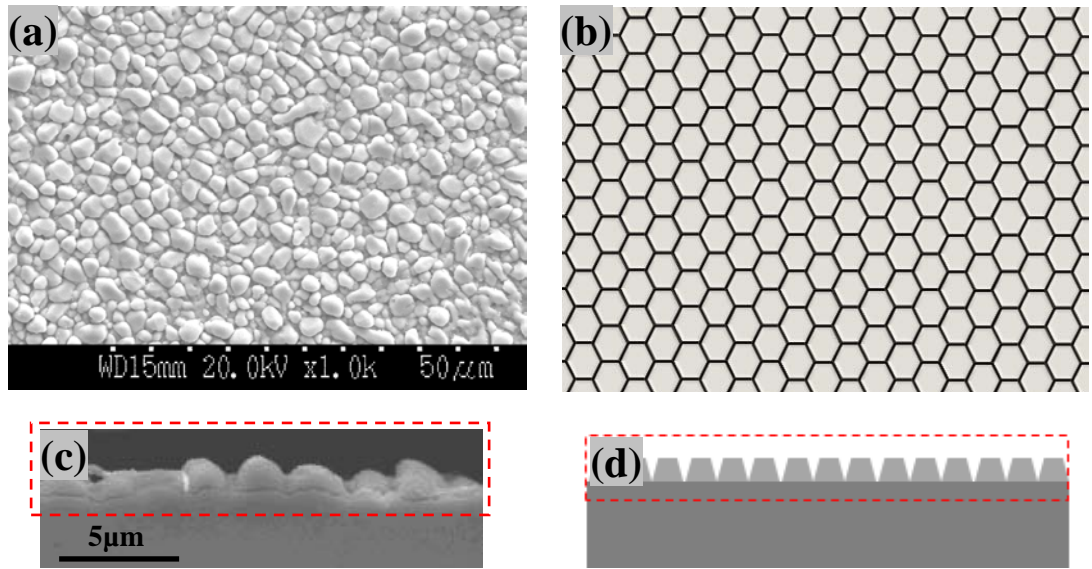


Figure 4.7: (a) Real surface topography of IMC1. (b) A simplified topography: a collection of regular hexagonal elements. (c) Cross-sectional view of IMC surface with marking an IMC layer. (d) Cross-sectional view of the simplified topography.

Geometrical details of a simplified surface and a hexagonal element are schematically shown in Figure 4.8.

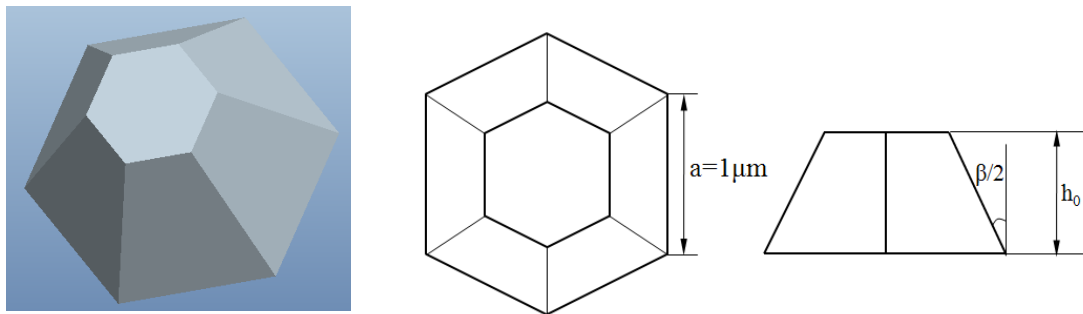


Figure 4.8: A regular hexagonal element which is used to simplify the IMC surface.

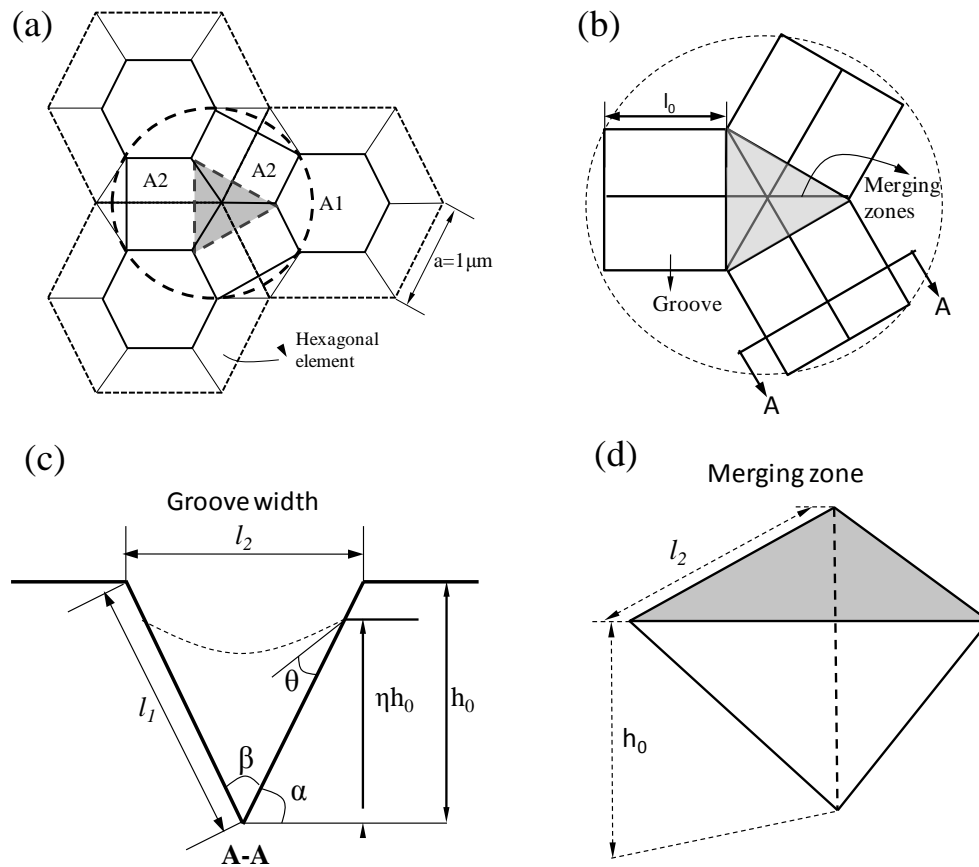


Figure 4.9. (a) Simplified surface topography of IMC1: (a) A collection of joined regular hexagonal elements. (b) Details of the topography. (c) Cross sectional view of an open triangular groove. (d) Details of the geometric configuration of a single merging zone.

Based on such a simplification of an IMC1 surface, it can be recognized that the surface roughness appears as composed of two main topographic features: (i) the open triangular grooves and (ii) the merging zones at the locations of the grooves where the channels are merging. Thus, the characteristic topographic features of the rough surface would include the number of grooves and the number of merging zones. Groove angle β , see Figure 4.9 (c), is assessed experimentally to be in average $\sim 57^\circ$, see Appendix C. The

characteristic geometric parameters are listed in Appendix E. The details of these topographical features are shown schematically in Figure 4.9. The so-defined topographical structure of the surface is used in modeling to characterize the related geometric features of the surface through an associated description of the network of triangular cross-section groves between the grains, thus forming the network of channels through which the liquid phase flows during the spreading phase of the considered phenomenon.

4.6 Building the Theoretical Model

The objective is to predict the movement of the triple line driven by surface tension and retarded by viscosity, i.e., to describe the kinetics of the spread front of liquid metal on a topographically altered IMC1 surface. Let us consider IMC1 surface as a two-dimensional porous medium. The following main assumptions will be imposed.

1. No chemical reactions during spreading. The reaction product already formed on a virgin Cu substrate in form of the IMC1 coating suppresses any further reaction due to the stability of Cu_6Sn_5 in the $\text{Cu}_6\text{Sn}_5/\text{Cu}_3\text{Sn}/\text{Cu}$ system at the interface that gets into contact with Sn from Pb-Sn liquid. (Appendix B)
2. The IMC1 surface's topographical features are considered as being spatially isotropic. In case of aging the IMC1 layer at the elevated temperature for a prolonged time, the scallop grain size becomes larger (IMC2 and IMC3) and may interfere with other surface alterations leading to the roughness non-uniformity and as a consequence leads to a preferential spreading, (Liu et al., 2011b; Zhao et al., 2009a; Liu et al., 2012) (considered in Chapter 5).

3. Liquid phase properties are constant during the spreading (temperature independent).
4. The gravity force impact vs. surface tension is neglected. The Bond number associated with liquid metal filling the groove is assessed as $Bo = g\rho(V/A)^2/\gamma \cong 8.19 \times 10^{-3} < 0.01$.
5. The liquid mass available for spreading during the viscosity/surface tension driven phase is of the same order of magnitude or larger than is the product of the liquid density and the volume of the region of the topographically altered interface fluid paths available for spreading at an instant of time. For example, the initial volume of the liquid at the source was in the range of 6 to 14 $\times 10^{-12} \text{ m}^3$ while the voids volume within the 2-D porous layer available for spreading up to the end of modeled period was in the range of 5.2 to $4.7 \times 10^{-12} \text{ m}^3$.
6. The surface alterations' volume available for liquid phase spreading is filled, in average, uniformly.

The control volume of the differential element of the 2-D axisymmetric porous substrate interface layer $\Delta\delta$ between triple line radii r_0 and r is presented in Figure 4.10. The onset of spreading starts at t_0 ; t_f is the time corresponding to the final spreading front location while t is an arbitrary time between t_0 and t_f so that $t_0 < t < t_f$, when $t = t_0 = 0$, $r = r_0$; u_0 and u correspond to t_0 and t , respectively.

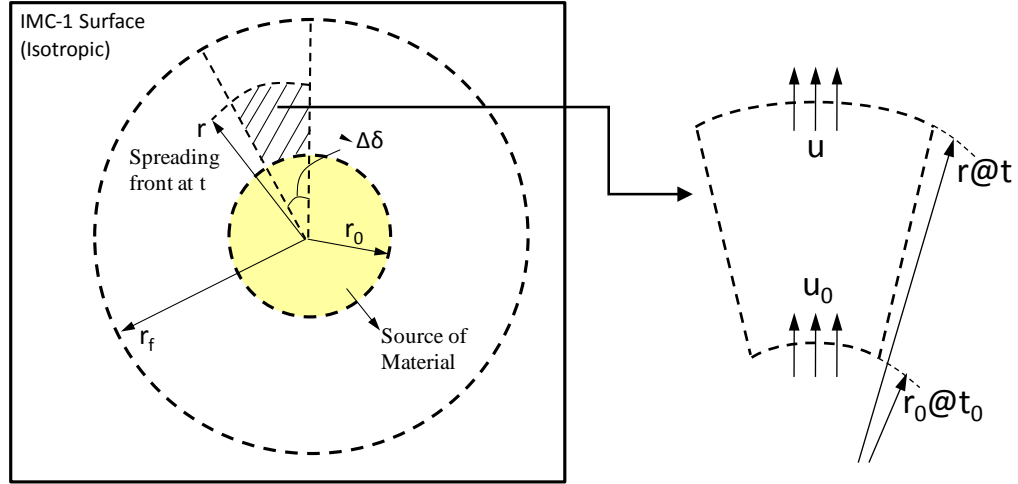


Figure 4.10: The control volume within the domain of a two dimensional porous medium

The velocity field must be consistent with the continuity equation and the Darcy's Law implemented for the arbitrary liquid metal differential element within the marked control volume (Bejan, 2004; De Wiest et al., 1969; Scheidegger, 1974)

$$\frac{D\rho}{Dt} + \rho \nabla \cdot \mathbf{v} = 0 \quad (4.1)$$

$$\mathbf{v} = -\frac{1}{\mu} [\mathbf{K} \cdot \nabla p] \quad (4.2)$$

where \mathbf{v} is the velocity vector (to be reduced to velocity u for a 2-D axi-symmetric flow), ρ is the liquid metal density, μ is the dynamic viscosity, and \mathbf{K} is a second order intrinsic permeability tensor of the porous medium (to be reduced to a scalar for an isotropic IMC1 surface) exposed to metal flow featuring the pressure gradient ∇p associated with the flow path driven by capillary force.

Taking into account the imposed assumptions, equations (1) and (2) become

$$\frac{1}{r} \frac{\partial}{\partial r} (ru) = 0 \quad (4.3)$$

$$u = \frac{k}{\mu} \left(-\frac{\partial p}{\partial r} \right) \quad (4.4)$$

From (3) one gets straightforwardly:

$$u_0 r_0 = ur \quad (4.5)$$

Replacing expressions of u_0 and u in Equation (4.5) by Darcy's law and definition of velocity respectively will lead:

$$\frac{k}{\mu} \left(-\frac{\partial p}{\partial r} \right)_{r_0} r_0 = \frac{d(\tau r)}{dt} r \quad (4.6)$$

The product (τr) , which is corresponding to arbitrary position r , is the path of the molten metal flowing through IMC1 surface alterations, introduces the concept of tortuosity into the model, (Epstein, 1989); similarly, ΔL_0 is the path associated with position r_0 , hence

$$\Delta L_0 = \tau r_0 \quad (4.7)$$

where τ is the tortuosity of the IMC1 surface introduced in Appendix F.

The pressure gradient at the location r_0 in Equation (4.6) can be approximated as

$$-\left. \frac{\partial p}{\partial r} \right|_{r_0} \sim \frac{\Delta p}{\Delta L_0} = \frac{\Delta p}{\tau r_0} \quad (4.8)$$

Combining Eq. (6) and (8) leads to

$$\frac{k}{\mu \tau^2} \Delta p = r \frac{dr}{dt} \quad (4.9)$$

The pressure drop driving the flow due to capillary force is determined by the topography of the surface, surface tension (Rye et al., 1996), but also the extend of filling the network of grooves,

$$\Delta p = \gamma \sin(\alpha - \theta) \tan(\alpha) / (\eta h_0) \quad (4.10)$$

where γ represents the liquid melt – solid surface tension; θ is the Young's contact angle for liquid melt in a surface groove, Figure 4.9 (c); α and h_0 represent the groove angle and height, Figure 4.9 (c).

Note that we introduce a filling factor η (see Appendix G), not considered in (Rye et al., 1998). Integration of Equation (4.9) with respect to time from t_0 to t across the domain of spreading from r_0 to r leads to

$$r^2 = 2 \frac{\gamma}{\mu} \frac{k}{\eta h_0 \tau^2} G_2(\alpha, \theta) t + r_0^2 \quad (4.11)$$

where

$$G_2(\alpha, \theta) = \sin(\alpha - \theta) \tan(\alpha) \quad (4.12)$$

In Equation (4.12), $G_2(\alpha, \theta)$ is a non-dimensional geometrical parameter stemming from the topography of a micro groove, Figure 4.9 (c). Equation (11) gives the correlation between an instantaneous location of the triple line, r , and the spreading time, t . It also shows that the spreading rate is related to the topography of the surface and liquid properties. Note that Equation (11) includes permeability, porosity/tortuosity and filling factor as the most important topographical features of the considered spreading phenomenon.

The value of (γ / μ) for eutectic tin-lead solder is estimated at 200 °C to be 148 m/s as reported by Yost et al (Yost et al., 1997). For Sn20Pb solder, the surface tension is estimated at 220 °C to be 420 mJ/m², (Howie and Hondoros, 1982; White, 1971). The viscosity is estimated to be 2.3 mPas also at 220 °C (Ejima et al., 1990). Physical properties for Tests - 1 through Test - 4 are listed in Table 4.2. For both solder materials, the equilibrium contact angle is assumed to be 25°, (Yost et al., 1997). Details of determination of the theoretical permeability and tortuosity are in Appendix F.

Table 4.2: Physical properties and porous surface characteristics (Data are adopted from (Yost et al., 1997; Howie and Hondoros, 1982; White, 1971; Ejima et al., 1990))

Test	Solder Material	γ	μ	$k_{\text{theor}} \times 10^{14}$	τ	θ
		(mJ/m ²)	(mPa s)	(m ²)	(-)	(deg)
Tests-1 and 2	Sn37Pb	400	2.7	1.364	2.590	25°
Tests-3 and 4	Sn20Pb	420	2.3			

4.7 Results and Discussion

Figures 4.11 and 4.12 show how predictions of triple line locations are validated against the associated experimental data. Note the error bar for the data ($< 3\%$ as discussed in Section 4.3 page 90) is smaller than the symbols thus invisible. Note that the solid and dashed lines for theoretical predictions in Figures 4.11 and 4.12 Figures are on top of each other.

The boundaries in Figure 4.11 and 4.12 are determined by a certain small relative deviation between the theoretical prediction and the empirical data with a purpose to cover a large portion of the spreading process. For example, Test-1 and Test-2, Figure 4.11, the capillary-viscous domain is defined with a relative deviation smaller than $\sim 15\%$; for Test-3 and Test-4, Figure 4.12, the capillary viscous stage is determined with a relative error smaller than $\sim 25\%$.

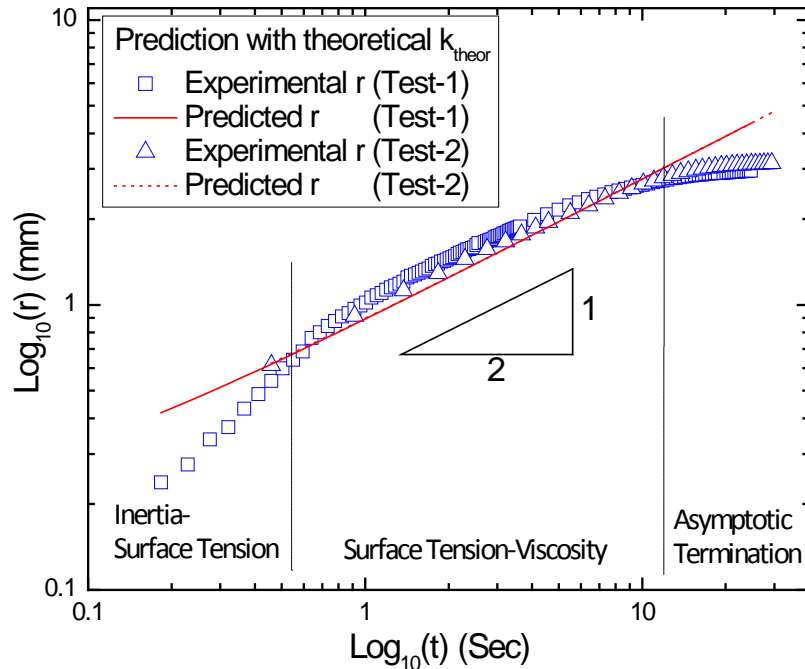


Figure 4.11: Prediction of the triple line location for Tests 1 and 2

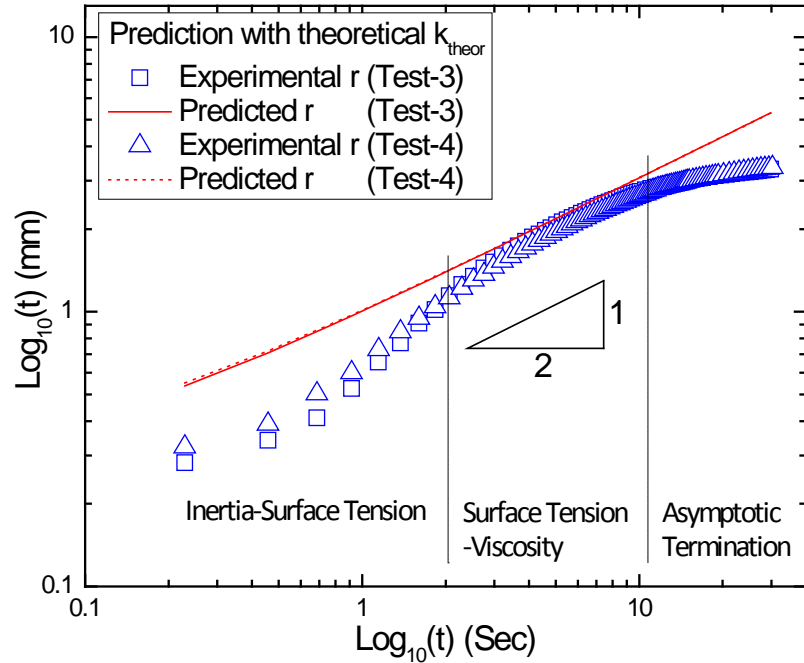


Figure 4.12: Prediction of the triple line location for Tests 3 and 4

Table 4.3 gives the average relative error of the prediction of triple line locations by Equation (4.11).

Table 4.3: Average Relative Error of Triple Line Location Prediction

Test No.	Average Relative Deviation of a Prediction	
	$k_{\text{theor}} = 1.364 \times 10^{-14} \text{ m}^2$ (Appendix F)	
	0-12 seconds	0.5-12 seconds
Test-1	13%	11%
	0-13 seconds	0.5-13 seconds
Test-2	5%	5%
	0-11 seconds	1-11 seconds
Test-3	20%	10%
Test-4	21%	15%

The relative deviations of triple line location predictions for the process of spreading within the central time range modeled are sizably smaller than for the overall data set (i.e., for a case that the initial phase of spreading is also included). The initial phase of the process is dominated by inertial forces as discussed in Section 4.4 on page 92 (Courbin et al., 2009). Hence this discrepancy is fully expected because the model intends to interpret the viscosity/surface tension controlled phase (excluding inertia controlled phase). For the case of the eutectic solder considered, the predicted value of the triple line location agrees well with the experiments (5% and 11%). For the case of 80Sn-20Pb solder, the agreement is also reasonable (10% and 15%). Hence, the validity of square root Equation (4.11) is demonstrated (assuming its true validity in the surface tension-viscosity regime of spreading). It should be emphasized that Equation (4.11) has been obtained for a physical situation that corresponds to a triple line movement of the liquid flowing through the surface alterations, hence implying a 2-D porous medium interpretation of the surface roughness, i.e., not for a triple line movement of a sessile droplet, as modeled by a Tanner's power law type correlation. A comparison between empirical data and both 1/2 and 1/3 law correlations indicates that a 1/3 power law (if adopted heuristically) may cover a broader time range but with a larger relative deviation (up to 10%). It should be noted that the proposed theory based on Darcy's law recovers rigorously the 1/2 power law relationship, as illustrated in this chapter. A detailed analysis of the local slopes of the empirical data, see Figure 4.10 and 4.11, reveals that the range of the power coefficient is $n = 1/2 + 0.13/-0.2$, with $n=1/2$ in the modeled (central) domain, and 1/1.4 at the transition from inertia to surface tension vs. viscosity domain, and 1/3 at the transition into an asymptotic termination of the spreading.

4.8 Summary

In this chapter, spreading of liquid metal (eutectic and hypo eutectic Sn-Pb) over an intermetallic substrate ($\text{Cu}_6\text{Sn}_5/\text{Cu}_3\text{Sn}/\text{Cu}$) is modeled as a surface tension and viscosity driven flow over a rough surface with a suppressed reaction at the interface. The phenomenon is modeled as a non-reacting fluid penetration of the micro layer of liquid along a two-dimensional axisymmetric porous interface. The validity of the Darcy's law has been assumed with both intrinsic permeability and associated tortuosity defined from a topographical model of scallop-like surface alterations. Hence, the flow over a rough surface is interpreted as a flow through the network of microgrooves characterized with (i) topographical features of the rough surface (i.e., effective intrinsic permeability, porosity/tortuosity, and micro channel cross-section geometry), (ii) wetting/spreading features (equilibrium contact angle and filling factor), and (iii) molten metal properties (viscosity and surface tension). Note that the topographic features of IMC rough surfaces can be characterized as a surface porosity and surface roughness either geometrically if representing uniform microstructures as in this chapter (IMC1), or experimentally if the roughness is random but not uniform as studied in Chapter 3 (IMC0).

The established model is corroborated with experimental data obtained for the kinetics of spreading of solders under controlled atmosphere by using frame decomposition of digital movie sequences obtained in real time and *in situ* by the hot-stage microscopy. The power law trend of the model predictions vs. empirical data has been verified for the domain of surface tension-viscosity controlled spreading regime. It is demonstrated that such an approach would overestimate spreading kinetics in initial and final stages of spreading.

The prediction generated from the model has a relative deviation from empirical data within the range of 5% to 15%. After the short time period featuring the inertial forces controlling spreading (between 0 and ~1-2 s after the onset of spreading), a 1/2 power law spreading phase takes place. Spreading terminates asymptotically upon exhausting the liquid metal source.

This chapter, Chapter 4, focuses on the experimental observation and analytical modeling of a radial spreading of molten solders on an intermetallic (IMC) surface with a roughness composed of uniformly distributed grains. This work constitutes an effort to extend the modeling approach advocated in Chapter 3 to a spreading of molten metal, as opposed to organic liquids as presented earlier in Chapter 3, over substrates having similar but uniformly distributed (or isotropic) topographic features. In the following chapter, Chapter 5, the effort will be extended to a preferential (rather than isotropic considered in this chapter) spreading of the same molten solder system on IMC surfaces with anisotropic (rather than isotropic) topographic features composed of intermetallic grains with a certain orientation.

CHAPTER 5: PREFERENTIAL SPREADING OF MOLTEN METAL OVER AN ANISOTROPICALLY MICROSTRUCTURED SURFACE[‡]

5.1 Overview

This chapter focuses on phenomenological observation, data collection, and modeling of a preferential spreading of molten solders on anisotropically microstructured intermetallic surfaces (IMC2 and IMC3) with roughness composed of grains forming certain orientations of the associated network of grooves. Hence, this chapter extends the modeling process discussed in the previous chapter (Chapter 4) to a spreading of molten metal over substrates having anisotropic rather than isotropic topographic features.

Spreading of a molten metal system on intermetallic surfaces (IMC2 and IMC3) with anisotropic microstructured surface topography was studied with hotstage microscopy and an elliptical spreading pattern was noticed. Surface characterization implies that the spreading may be preferential, i.e., aligned to the direction associated with the grain orientation of the intermetallic surface. Empirical data to be presented did confirm that expectation. The kinetics data indicate that imbibing follows Washburn relation during the middle spreading stage (after more-or-less brief initial spreading segment) and then deviates due to the impact of finite-size source material before the ultimate asymptotic termination. A theoretical model was established to analyze such a preferential spreading phenomenon: the main stage of the spreading kinetics agrees well with the Washburn-type $x \sim t^{1/2}$ relation obtained by the theoretical model, but the semi-empirically determined constants differ along the main axes of spreading (as opposed to the situation studied in the previous chapter); for the subsequent time segment of the phenomenon evolution an $x \sim t^{1/n}$ ($n \approx 5$) relation was established. The study in this chapter

[‡] This chapter includes detailed account of material summarized in *EPL* (2012), Vol. 97, 46003

shows that the direction of spreading of molten metal flow can be controlled by surface topography modification at the micro scale and that kinetics of the main phase of the spreading can still be described well with the already proposed model (see Chapter 3). Please note that the chemical reaction has been minimized by using an intermetallic substrate.

In this chapter, we first demonstrate preferential spreading phenomena associated with molten alloys wetting which ultimately ends with an elliptical spreading pattern at an elevated temperature of up to ~486 K (Heating cycle is given in Figure 4.4 in Chapter 4). Subsequently, it is verified also experimentally that the preferential spreading direction is controlled by the orientation of the grains at the substrate's surface. The spreading process is theoretically considered in terms of an analytical model established to predict the kinetics of the triple line during the main stage of the phenomenon evolution. Finally, corroboration of the theoretical model and empirical data is performed.

5.2 Experimental Observation and Results

The materials and manufacturing processes for IMC1, IMC2 and IMC3 used for the study in this chapter are discussed in details in Chapter 2. The *in situ* observation of the spreading of molten solder materials on IMC2 and IMC3 substrates at elevated temperature levels was conducted by using the hotstage microscopy, which is introduced in Chapter 3. Image sequences for spreading kinetics are extracted from videos captured by the hotstage microscopy.

The purpose of the experimental study in this chapter is to (1) show that a change of topographical features of the rough surface can be used for tuning the preferential spreading; (2) experimentally demonstrate the correlation between the illustrated spreading preference and the presence of anisotropic topographic features of the substrate; (3) provide empirical data for validating the theoretical model that describes the kinetics during the main evolution stage of such a preferential spreading (the one governed by surface tension and retarded by viscosity).

5.2.1 Preferential Spreading (Directional Spreading)

Figure 5.1 (a), (b) and (c) offer three different sets of images from the tests of a molten metal spreading (in a form of imbibition) on IMC1, IMC2 and IMC3 surfaces, respectively. The presented frames were extracted from the movie clips generated during the set of real time, *in situ* monitoring of the spreading of a solder (Liu et al., 2011b). It can be noticed that IMC1 has a random but uniform distribution of IMC grains. IMC2 and IMC3 feature a spatial orientation of grain structures of a larger size. The difference between spreading of a single molten metal system, i.e., an eutectic Pb-Sn solder, on such three different surfaces is clearly identified. Figure 5.1 (d) indicates that the final spreading pattern of a molten solder on an IMC1 substrate is almost a perfect circle. Figure 5.1 (e) and (f) offer an elliptical spreading pattern for a molten solder on an IMC2 and IMC3 substrate, respectively.

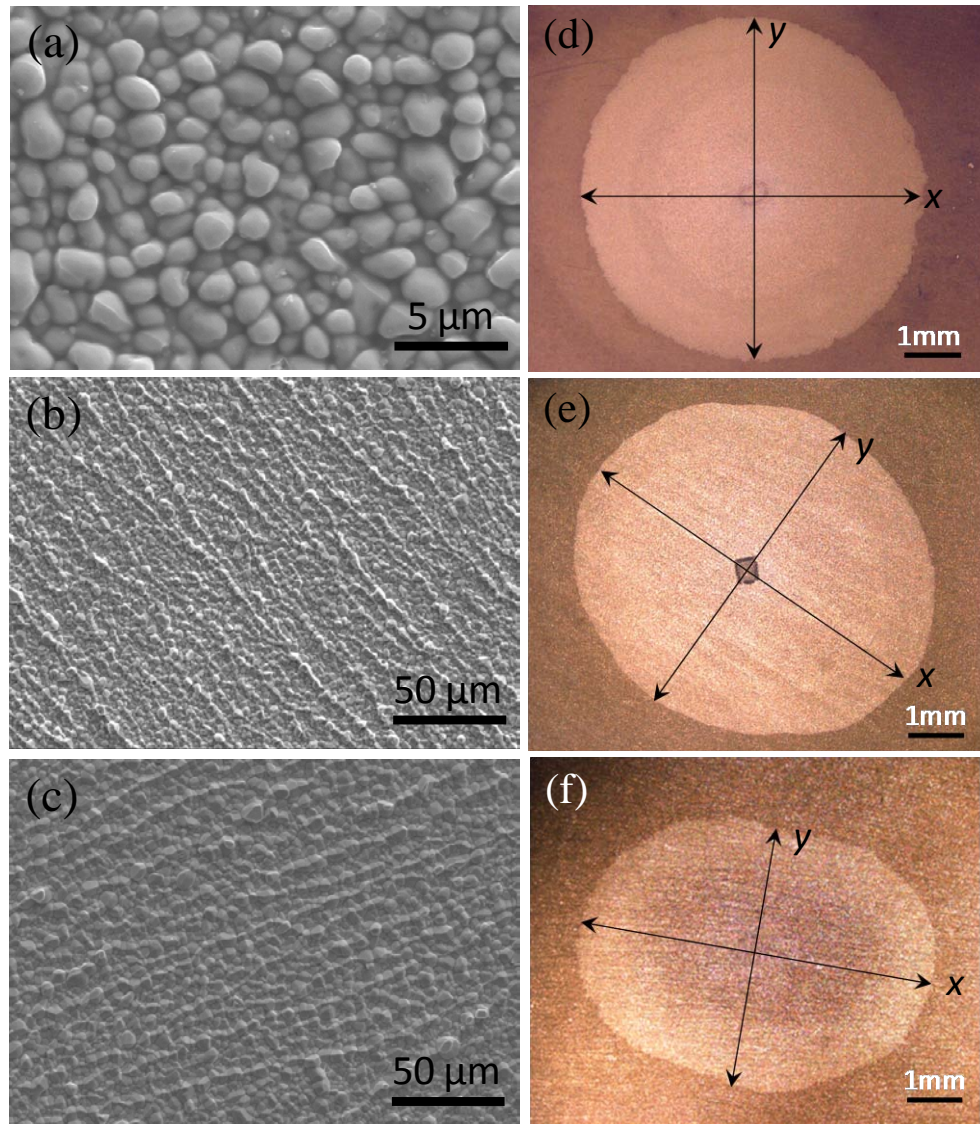


Figure 5.1: (a) (b) and (c): SEM images showing topographical features of an IMC1, IMC2 and IMC3 substrate respectively; (d): a final circle pattern for eutectic Pb-Sn solder spreading on an IMC1 substrate; (e) and (f): elliptical patterns for eutectic Pb-Sn solder spreading on an IMC2 and IMC3 substrate, respectively

Note that the ratio of the orthogonal long and short axes of spreading patterns, which will be referred to as the *directional spreading ratio* R_{ds} , is different for IMC2 and IMC3. It is noticeable that directional spreading ratio of an imbibition on IMC2 is smaller

than that of IMC3 and this difference is consistent for at least three sets of empirical data for IMC2 and IMC3. The comparison of spreading on IMC1 and IMC3 (or IMC2) implies that the elliptical spreading pattern of molten metal is assumed to be caused by topographic features of IMC3 (or IMC2).

Figure 5.2 offers the quantitative data of the magnitudes of directional spreading ratios for spreading on IMC1, IMC2 and IMC3. The microstructured surface generated from a longer aging process at a higher temperature is associated with a larger R_{ds} .

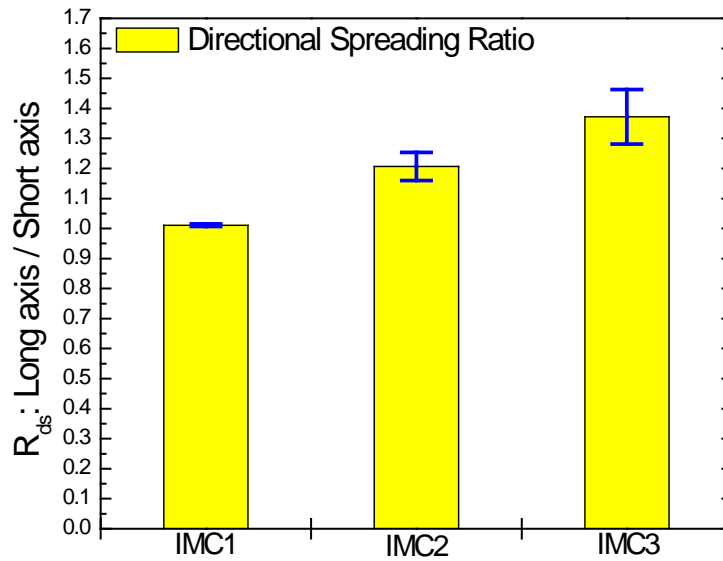


Figure 5.2: Ratios of the length of long axis to short axis for IMC1, IMC2 and IMC3 substrates.

The directional spreading ratios R_{ds} of cases for IMC1, IMC2 and IMC3 are 1.01 ± 0.01 , 1.21 ± 0.05 and 1.37 ± 0.09 , respectively. The average empirical data and associated standard deviations were determined by multiple measurements for three independent imbibition tests for each IMC substrate. The measurements were performed with Image Pro software with an estimated uncertainty of ~3% for linear length determination.

It should be noticed that the spreading process (i.e., imbibition) of a molten eutectic solder on IMC1 has been studied in Chapter 4. This includes (i) a topographical characterization and (ii) the kinetics analysis and modelling. The new and independent empirical evidence for IMC2 and IMC3 as shown in Figure 5.1 (b), (c), (e) and (f), demonstrates the influence of topographical alterations on the spreading behavior of a molten metal system. The empirical evidence indicates that the spreading could be tuned by surface manufacturing techniques.

5.2.2 Surface Characterization

The preferred spreading direction and the one perpendicular to that direction are designated as x - and y - axis (a long and a short axis of the elliptical pattern of the triple line locus of points), respectively, as indicated in Figure 5.3 (a). The residue of a small amount of source Pb-Sn material around the center area can be noticed in Figure 5.3 (a). Figure 5.3 (b) offers a SEM image for an area within the black dotted square shown in Figure 5.3 (a). The front of the residue of the source material and the x and y principal directions are identified. It can be noticed that the agreement between the preferred spreading direction and the direction of the parallel traces along the succession of large grains is clearly identifiable.

Figure 5.3 (c) gives a close-up of the parallel traces along larger grains within the domain shown in Figure 5.3 (b). Hence, the agreement between the preferred spreading direction and the direction of parallel traces is fully confirmed. The re-solidified Sn-Pb alloy residue within the grooves is identified and it is verified that the grooves formed among grains are filled during spreading to a certain extent.

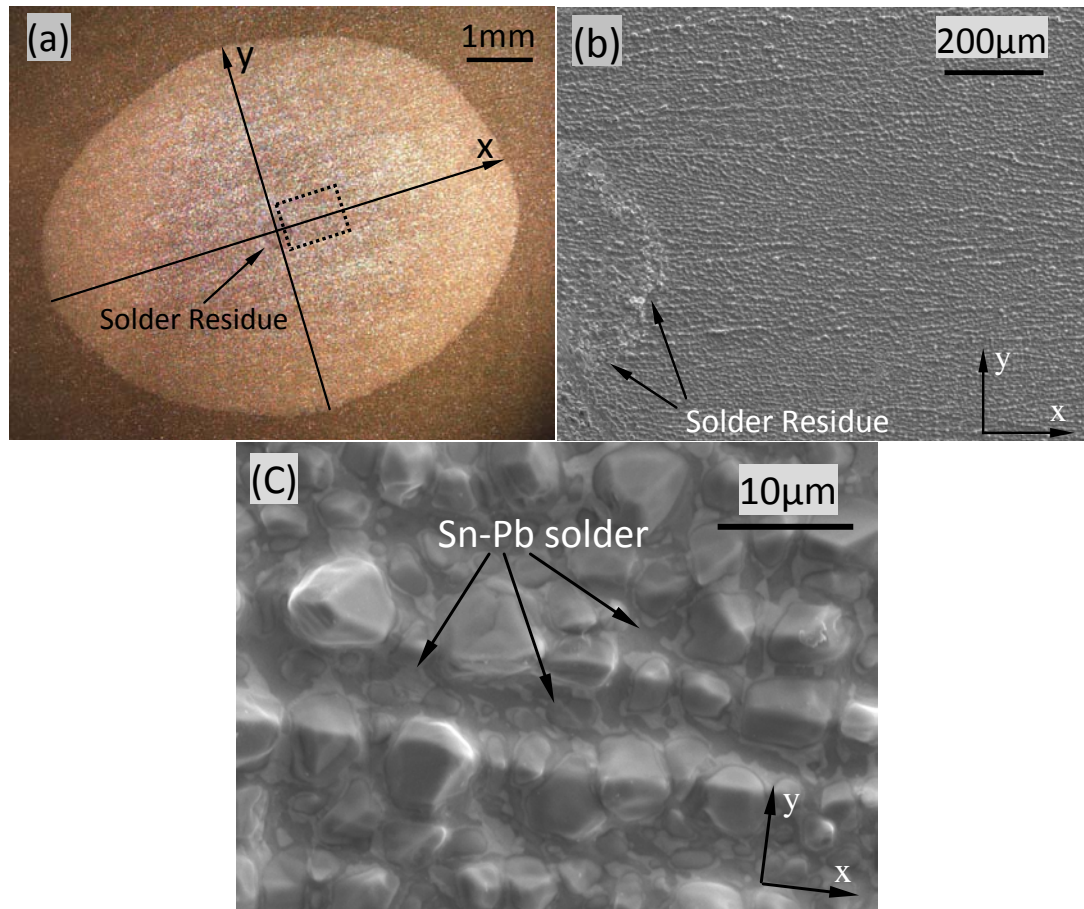


Figure 5.3: (a) The final ellipse-like spreading pattern with x (preferential) and y axis, (b) Source material residue and the parallel traces of grains associated with the x axis, (c) Small amount of re-solidified solder material present in grooves between parallel traces of grains after spreading. Note x and y directions are consistent in (a) (b) and (c).

In order to obtain more details about topographic features of substrates, the atomic force microscopy (AFM) is utilized to identify the details of the surface topography. Figure 5.4 (a) indicates a representative scanning result of a randomly selected $50\mu\text{m} \times 50\mu\text{m}$ area of IMC3, with a vertical length scale marked on the right. It is noticed that the parallel traces composed of the larger grains form aligned barriers so

that valleys are formed between them. Figure 5.4 (b) illustrates a view along the parallel traces (x -axis). The chains of the peaks and the valleys between appear to be obvious. Figure 5.4 (c) offers a view perpendicular to that of Figure 5.4 (b). In this case, no major aligned topographical features are observed. Therefore, no contiguous channel-like topographical features can be identified in that direction.

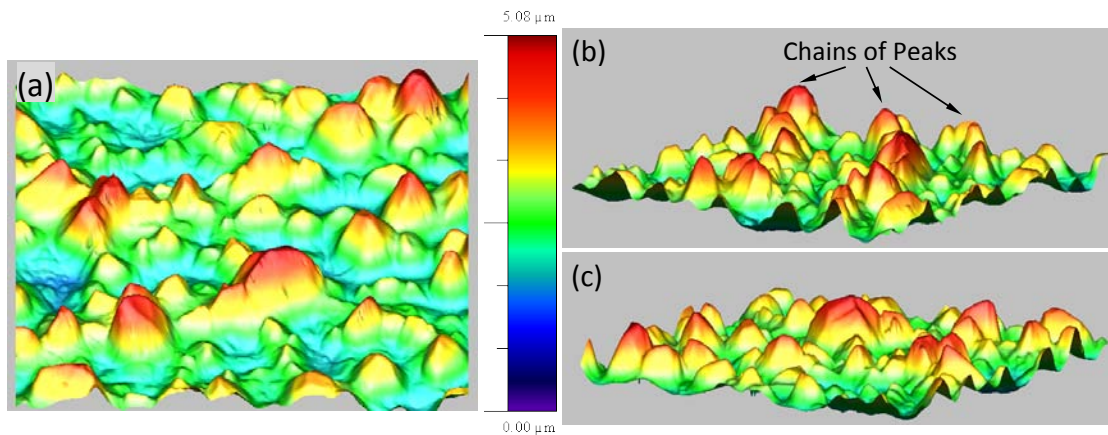


Figure 5.4: (a) Parallel traces of the larger grains showing peaks and valleys, (b) Chains of peaks identified from a view along the parallel traces of larger grains, (c) No chains of peaks noticed from a view along the direction perpendicular to the chain of peaks identified in (b)

The surface characterization with SEM and AFM confirms that parallel traces of larger grown grains on IMC3 lead to a preferential spreading of molten metal. That can be explained by the fact that the liquid metal flows along the x direction while confined within chains of peaks, hence flows through channel-like topographical formations of the surface by the mechanism of imbibition. On the contrary, the liquid metal along the y direction has to conquer barriers composed of grain peaks, although there are scattered

open triangular channels formed between the peaks in this direction as well. Hence, liquid metal experiences more resistance to spreading in that direction. Different topographic features of the flow paths along those two directions cause the preferential spreading.

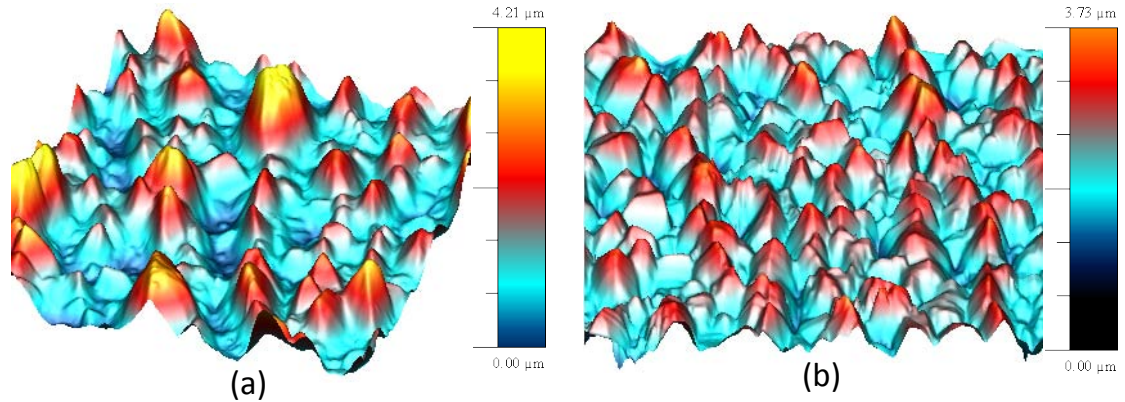


Figure 5.5: AFM scanning results indicate the topographical features of (a) IMC3 and (b) IMC2 substrates. (The scanning area is $50 \times 50 \mu\text{m}$)

Figure 5.5 (a) and (b) offer the AFM scans of surface topographical features for IMC3 and IMC2, respectively. The scanning was conducted for both cases on a random substrate area of $50 \times 50 \mu\text{m}$. It can be noticed that the micro grains on IMC2 substrate are more compact and smaller than those on IMC3. Due to an aging process at a higher temperature IMC3 substrate features more pronounced grain orientation and so formed parallel surface grooves along a certain direction. As it is demonstrated that such grain orientation is associated with the direction of the long axis of the elliptical imbibition pattern, it could be understood that the difference between the directional spreading ratios of IMC2 and IMC3 cases (Figure 5.1 (b) and (c)) arise from the size and compactness of their topographical features because the same molten metal system was used.

For the modeling that will be described in “Theoretical Analysis” section of this chapter, Section 5.3, we experimentally consider IMC3 substrate. The mechanism of spreading for IMC2 would be similar to that for IMC3. The topographic difference along those two flow directions for IMC3 is characterized quantitatively by defining the associated surface porosities as in Chapter 3 and 4 (Liu et al., 2011a and b; De Wiest et al., 1969; Scheidegger, 1974). These surface porosities are determined by AFM scanning using WSxM 5.0 Develop 3.3 software (Horcas et al., 2007). Similarly, as discussed in Chapters 3, 4 and in (Liu et al., 2011 a and b), the tortuosities along x axis (between traces of the grains) and y axis (across traces of the grains) are determined to be: $\tau_x = 1.71$ with a deviation of 0.05; and $\tau_y = 1.88$ with a deviation of 0.09. Multiple measurements of the porosity at 4 different randomly selected scanning locations were conducted. Note that the tortuosity of the porous medium can be related to the associated porosity by a relationship as follows $\tau = \varepsilon^{-1.2}$ (Boving et al., 2001). Moreover, following the approaches for surface characterization described in Chapter 3 and AFM scanning results, the average height of the grains and the average groove angle on IMC3 are determined to be $1.4 \mu\text{m}$ with a standard deviation of $0.2 \mu\text{m}$ for four independent scans at various locations and 45° with a standard deviation of 6° based on measurements of groove width taken at 40 randomly selected grooves, respectively.

5.2.3 Spreading Kinetics

Figure 5.6 (a) demonstrates the random but uniformly distributed topographical features of an IMC1 substrate. Figure 5.6 (b) offers a sequence of instantaneous image frames during spreading of the Sn-Pb eutectic pellet positioned in the center of the field of vision. The spreading was on an IMC1 surface at ~ 486 K (The temperature profile is offered in Figure 4.4 in Chapter 4). The almost perfect circular triple line spreading results from a uniform distribution of the scallop-like randomly distributed surface grains. The experimental study and modelling of such a spreading was demonstrated in Chapter 4. Figure 5.4 (d) illustrates anisotropic spreading of Sn-Pb eutectic on an IMC3 surface at 486 K (The temperature profile is offered in Figure 4.4 in Chapter 4). This spreading features an elliptical triple line pattern. Spreading was observed in situ and recorded as a digital video clip by using a hotstage microscopy system with a frame rate of 22 frames / second. A sequence of individual frames of the spreading process was extracted from the recorded video.

Note that the basic mechanism of spreading on an IMC2 or IMC3 surface is the same as on IMC1 as described in Chapter 4: the molten material formed from a solid pellet positioned in the center stays in bulk and is gradually sucked into microgrooves throughout the porous surface by a capillary force (imbibition). It can be noticed that the spreading prefers one direction throughout the whole process. This behavior was reported first by Zhao et al (Zhao et al., 2009a).

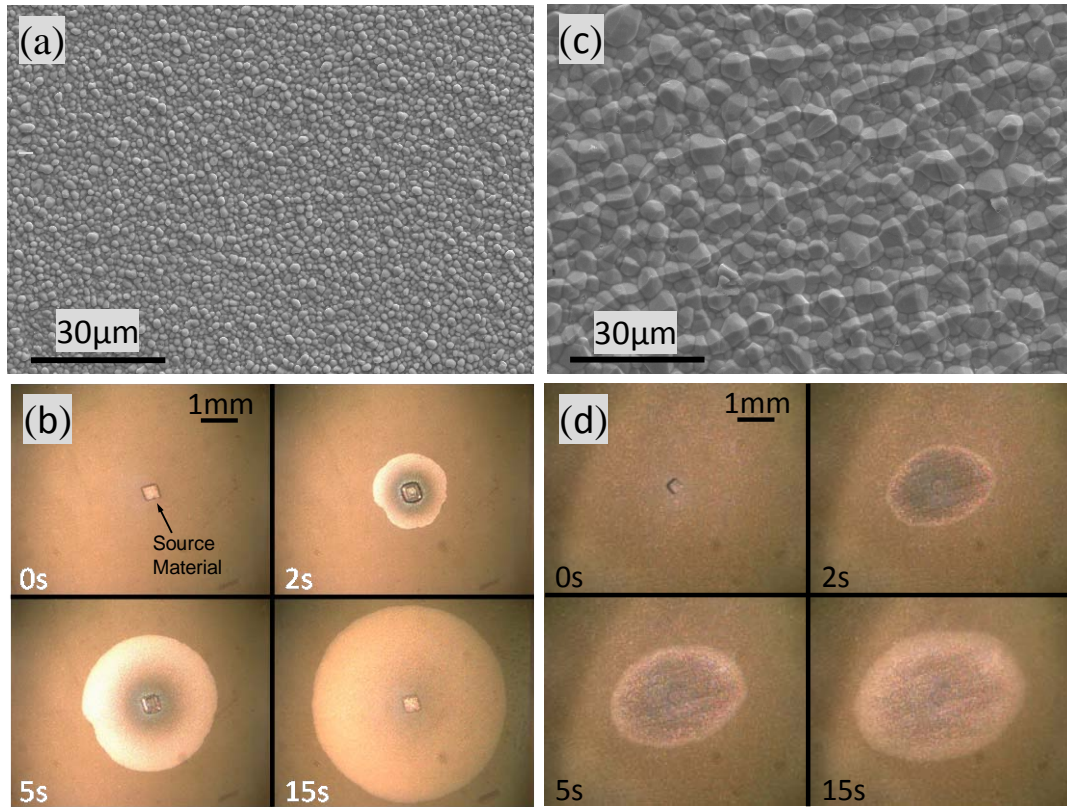


Figure 5.6: (a) SEM image of the surface topography of an IMC1 surface, (b) An image sequence of the Sn-Pb eutectic spreading on IMC1 surface, (c) SEM image of an anisotropic topography featured by the IMC3 surface topography, (d) Image sequence of the Sn-Pb eutectic spreading on IMC3 surface.

Figure 5.7 offers the kinetics data of imbibition on all three types of microstructured surfaces in a log-log scale. It is noticed that the kinetics of the uniform spreading on IMC1 is faster than the spreading along short axes for IMC2 and IMC3, and slower than preferential spreading along the long axes. The spreading rate along the long axis of IMC3 substrate is largest among all, and on the other side the spreading rate along the short axis of IMC3 is the lowest comparing to those of IMC2 and IMC1. The difference between them implies that the kinetics is influenced by and hence could be

tuned/controlled with the modified topographical features of the surface. Note that (i) the data for IMC1 in Figure 5.7 is the same data set for Test 2 in Figure 4.6 in Chapter 4, (ii) the data for IMC3 in Figure 5.7 is the same data set for Test 1 presented in Figure 5.9. Data set for IMC2 is presented in Table H5 in Appendix H.

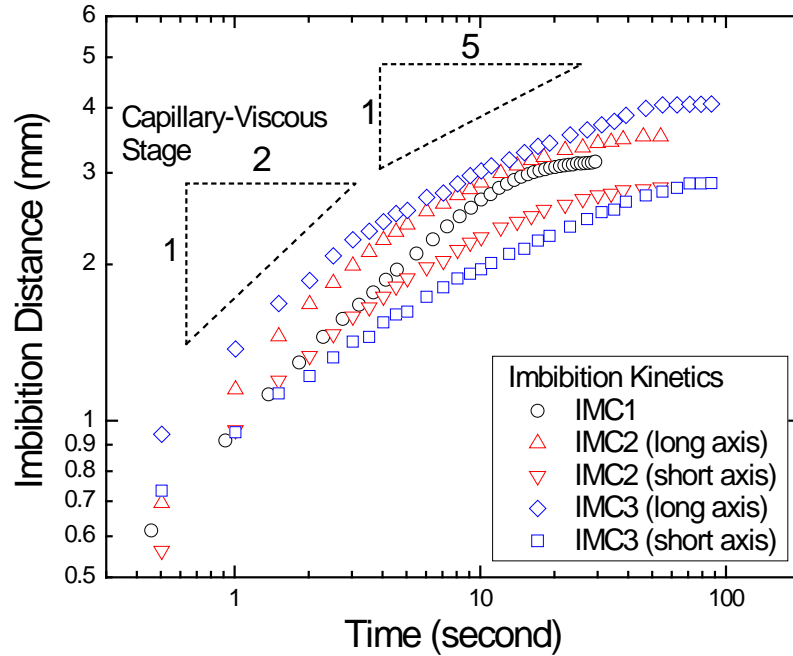


Figure 5.7: Kinetics of spreading on IMC1, IMC2 and IMC3 in a log-log scale, respectively.

It should be pointed out that the spreading within the capillary-viscous stage of all three cases follows the Washburn-type relation and terminates with an asymptotic ending (as discussed in Section 4.4 in Chapter 4). It is also noticed that the directional spreading on IMC2 and IMC3 features a transitional stage between the capillary-viscous stage and the final asymptotic ending, which has a slower kinetics than the one described by Washburn-type relation. With the data sets for surface topographical features and spreading kinetics, the purpose is to establish a theoretical frame for modeling the

directional spreading. The theoretical analysis is an extended effort of the modeling processes demonstrated in previous chapters, i.e., Chapter 3 and Chapter 4. The basic physical mechanism of imbibitions is the same for both spreading situations; hence the theoretical prediction may be based on the same model.

5.3 Theoretical Analysis

In this chapter a model that can describe the anisotropic spreading is going to be established, which is an extended effort to the modeling processes for a planar and an axisymmetric configurations introduced in previous chapters, i.e., Chapter 3 and 4. Note that the model in this chapter, will be different than that in Chapter 3 and 4, i.e., it is established without introducing Darcy's law as a momentum equation and the permeability as a factor that describes the topographical features.

The kinetics of molten metal spreading on IMC3 substrate will be theoretically analyzed with the following assumptions (Note that the similar assumptions are listed in the modeling process described in Section 4.6 in Chapter 4, but it is our intension to formulate the set here again: (i) the IMC surface is considered as a porous domain, composed of a network of open triangular grooves; (ii) no chemical reaction exists during the spreading process; (iii) properties of molten metal are considered as constant during the spreading process; (iv) gravity is negligible as the Bond number is small: $Bo = \rho g(V/A)^2 / \gamma \approx 8.0 \times 10^{-3}$ in this case (V and A are volume and surface area of the solder pellet, respectively), see Appendix A; (v) the liquid metal free surface curvature along the groove axis is negligible compared to that across the groove axis; (vi) the sessile drop type spreading could be divided into 4 stages: (1) the inertial stage: starts with the

completion of the phase change of the source material. It usually lasts for a very short period of time (i.e., around 10^0 second) and features an $R \sim t^{1/n}$ relation with n smaller than 2, as we emphasized in the previous chapter, Chapter 4. (Liu et al., 2011 a and b) (2) the capillary-viscous stage: the main stage of the spreading process. The capillary force will be the driving force for the spreading, while the viscous force plays a role of a retarding force. The duration of this stage depends on the source material quantity. Otherwise the asymptotic effect involving diminishing liquid metal at the source will influence the spreading, as mentioned in Chapter 4, (Liu et al., 2011b); (3) the capillary-viscous-asymptotic stage: as the liquid source material begins to deplete, the asymptotic effect starts to influence the spreading. This stage is a transition stage from the capillary-viscous stage to the final stage, which features an $R \sim t^{1/n}$ relation with n larger than 2 as it can be noticed in Section 4.7 in Chapter 4. The power law regimes in this stage have also been noticed and reported for the capillary flow in an interior corner (Weislogel et al., 1996); (4) the asymptotic stage: as material at the source gets depleted the spreading process stops.

The model is based on the theoretical analysis of kinetics of the triple line location movement of liquid metal exposed to spreading along x and y directions within the capillary-viscous stage. Derivation of the kinetic model will be demonstrated for the x direction and the same should be applied to the y direction.

In this analysis, the IMC3 microstructured surface is, as assumed, considered as a porous medium. Therefore the real path of the liquid metal flow through such a porous domain is larger than the apparent distance from the origin. The relation between the apparent and the real paths is given by Epstein (Epstein, 1989)

$$x^* = \tau_x x \tag{5.1}$$

where τ_x is the tortuosity along the x direction, defined as the ratio of the real extended curved path that fluid passes through the micro channels, x^* , to the shortest distance between the ends of the real path, x . The tortuosities along x and y directions are different as mentioned in the ‘‘Surface characterization’’ section.

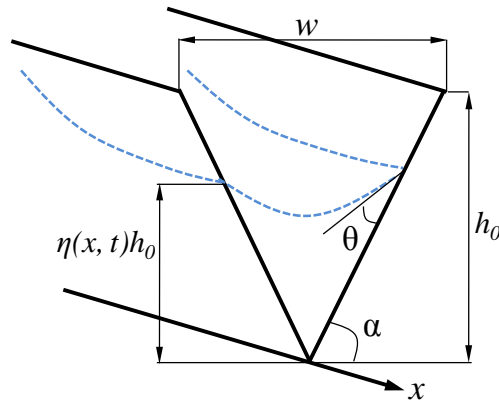


Figure 5.8: Configuration of the model of an open triangular groove with a liquid phase within it (Rye et al., 1996)

Figure 5.8 offers the model configuration of a typical representative open triangular groove formed with liquid phase in it. In Figure 5.8, w is the groove width; h_0 is the groove height; α is the groove angle; θ is the contact angle of liquid; $\eta(x^*, t)h_0$ represents the actual height of the liquid in a groove where $\eta(x^*, t) \in (0,1)$ represents the filling factor function defined as the ratio of (i) the actual liquid height in a groove at a certain location and corresponding instant of time and (ii) the groove height.

Rye et al (Rye et al., 1996) applied Poiseuille’s law to an open triangular groove and have established a model for the kinetics of a flow through a single open triangular groove. Following that approach, the volumetric flow rate of liquid through a single

meandering groove at the spreading front along the x direction on an IMC3 porous surface can be expressed as

$$q(x^*, t) = \frac{A^2(x^*, t)}{8\pi\mu} \left(-\frac{\partial p}{\partial x^*}\right) \quad (5.2a)$$

where μ is the dynamic viscosity of liquid; $(-\partial p / \partial x^*)$ is the gradient of the capillary driven pressure in the groove; $A(x^*, t)$ is the cross-sectional area of the flowing liquid in the groove (Rye et al., 1996; Liu et al, 2011a and b)

$$A(x^*, t) = [\eta(x^*, t)h_0]^2 A^*(\alpha, \theta) \quad (5.2b)$$

where $\eta(x^*, t)$ is the filling function, and h_0 is the height of grooves indicated in Figure 5.4. α is the groove angle and θ is the contact angle, also presented in Figure 5.8. $A^*(\alpha, \theta)$ has the following form (Rye et al., 1996)

$$A^*(\alpha, \theta) = \frac{1}{\tan^2(\alpha) \sin^2(\alpha - \theta)} [\sin^2(\alpha - \theta) \tan(\alpha) - (\alpha - \theta) + \sin(\alpha - \theta) \cos(\alpha - \theta)] \quad (5.2c)$$

The driving force originates in the pressure difference of the liquid in grooves caused by capillary effects. As the principal curvature of liquid parallel to the grooves is negligible (Rye et al., 1996), the capillary pressure can be expressed as

$$\Delta p = \frac{\gamma \sin(\alpha - \theta) \tan(\alpha)}{\eta(x^*, t)h_0} \quad (5.3)$$

where γ is the liquid-vapor surface tension.

The volumetric flow rate of fluid driven by capillary force in a single meandering open triangular groove is also expressed as the product of the flow velocity and the cross-sectional area of the flowing liquid,

$$q(x^*, t) = [\eta(x^*, t)h_0]^2 A(\alpha, \theta) \frac{d(x^*)}{dt} \quad (5.4)$$

Assuming that there are N grooves crossing a differential control domain at the spreading front in x direction on IMC3 surface, the total volumetric flow rate through such a control domain can be expressed by both equation (5.2a) and (4) as $Nq(x^*, t)$. Thus this equality of total flow rates in a steady state and with no compressibility effects described by equations (5.2a) and (5.4), for any N , would offer

$$\frac{(\eta(x^*, t)h_0)^2 A(\alpha, \theta)}{8\pi\mu} \left(-\frac{\partial p}{\partial x^*}\right) = \frac{d(x^*)}{dt} \quad (5.5)$$

For the capillary-viscous stage of the spreading process, $\eta(x^*, t)$ keeps constant as the source material can supply a sufficient material for spreading.

Therefore we have $\eta(x, t) = \eta_{0,x}$ within capillary-viscous stage, where $\eta_{0,x}$ is the initial filling factor when source material is sufficient. So, with a constant filling factor function the pressure gradient along x -axis is estimated as

$$-\frac{\partial p}{\partial x^*} \sim \frac{\Delta p}{\tau_x x} \quad (5.6)$$

Integration of equation (5) and the corresponding equation for y direction will offer a Washburn type ($x \sim t^{1/2}$) model for the spreading kinetics

$$\xi^2 = \frac{\eta_{0,\xi} h_0 \sigma}{4\tau_\xi^2 \pi \mu} G(\alpha, \theta) t + \xi_0^2, \quad \xi = x \text{ or } y \quad (5.7a)$$

where

$$G_3(\alpha, \theta) = A(\alpha, \theta) \tan(\alpha) \sin(\alpha - \theta) \quad (5.7b)$$

In equations (5.7a–b) x_0 and y_0 (introduced through ξ_0 symbol) represent the equivalent initial radius of the source material at the onset of melting and they are identical to the initial source material of small mass, considered as being spatially symmetric. Note that Equations (5.7a - b), which are the counterpart of Equations (3.10 - 3.11) in Chapter 3 and Equations (4.11 - 4.12) in Chapter 4, does not contain permeability as a parameter that describes the topographical features of rough surfaces for the purpose of an easier estimation and prediction of the spreading radii.

For the spreading process in the capillary-viscous-asymptotic stage, $\eta(x, t)$ gradually decreases as the finite source material begins to deplete (an asymptotic influence: the filling factor is changing as a function of time, and the spreading distance). Therefore, integration of Equation (5.5) in the case of a variable filling factor function is expected to generate a model with $x \sim t^{1/n}$ relation with n different than 2.

5.4 Results and Discussion

Figure 5.9 offers the kinetics data in a logarithmic scale for two selected, independent Sn-Pb spreading tests on IMC3 substrates at ~486 K. (The temperature profile is offered in Figure 4.4 in Chapter 4). Those two tests are associated with different amounts of the initial Pb-Sn eutectic solder source material (Test 1: $\sim 7.94 \times 10^{-3} \text{ mm}^3$; Test 2: $\sim 5.33 \times 10^{-3} \text{ mm}^3$). Spreading radius was measured from a frame sequence decomposed from the videos of the tests recorded by a hotstage microscopy system. Determination of linear dimensions by using Image Pro[®] software is associated with an uncertainty smaller than 3%. Note that Test 1 and Test 2 are selected at random from a number of tests performed used for this kinetics study. All data of the other tests are fully consistent with the trend represented by Test 1 and Test 2. Note that the data set for Test 1 is the same data set for IMC3 as presented in Figure 5.6

It can be noticed from Table 5.1 that Test 1 is associated with a larger mass of source material so that the final spreading radius is larger than that of Test 2. Therefore, the final radius of the spreading is dominated by the initial material amount, as expected. On the other hand, the ratios of the final spreading radii for both tests are very close to each other, (Liu and Sekulic, 2011b), the last column in Table 5.1. Thus the initial material sizes have a minimal impact on the ratio of the spreading radii, which is assumed to be dominated by surface topography.

The solder used in this study represents the eutectic tin lead solder (Sn37Pb) with a surface tension of $\sim 400 \text{ mN / m}$, and a viscosity of $\sim 2.7 \text{ mPa}\cdot\text{s}$ at molten state at $\sim 473\text{K}$ (Yost et al., 1997; Howie and Hondoros, 1982; White, 1971; Ejima et al., 1990). The contact angle is estimated as 25 degree as reported in (Yost et al., 1997). As stated in the

Section 5.2.2 “Surface characterization”, the groove angle is measured to be $\alpha = 45^\circ$, the average height of grains as the groove height is determined to be $h_0 = 1.4 \mu\text{m}$. With implementing these data values, equations (5.7a-b) will yield a prediction of the kinetics for capillary-viscous stage of the considered spreading for both x and y directions, as listed in Figure 5.9.

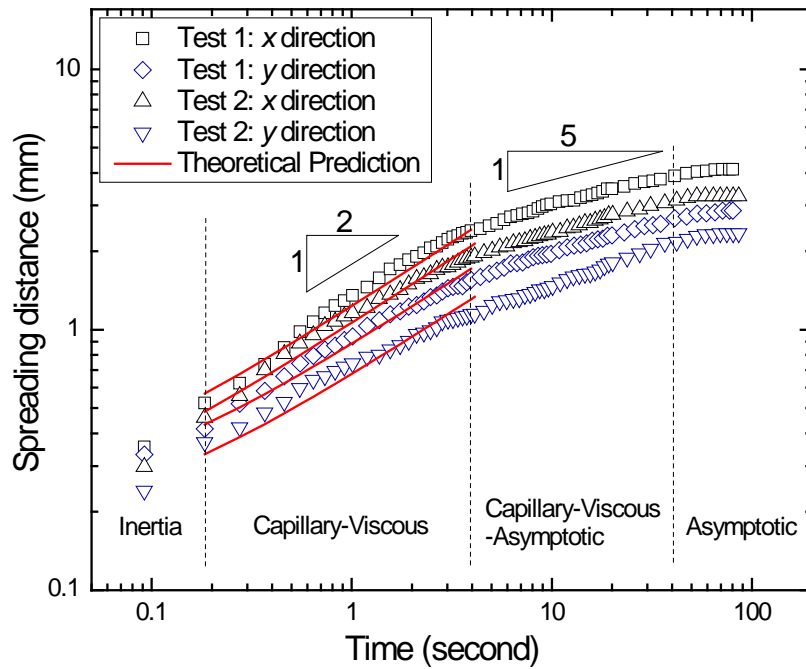


Figure 5.9: Kinetics data of Sn-Pb alloy spreading on IMC3 substrates at $\sim 486 \text{ K}$ featuring two different kinetics power laws and an asymptotic ending.

From the ~ 0.2 up to ~ 4 seconds of the process, the capillary-viscous stage covers up to 58% of the final spreading distance. The theoretical model (Equations (5.7a-b)) gives a good prediction of kinetics with an average relative error of $6\% \pm 10\%$ for both x and y directions with two different estimated constant filling factors, see table 5.2. Note that (i) different filling factors along x and y direction at early time are due to the different topographic features along the flow paths, and due to various amounts of the

initial material; (ii) the ending time of Washburn type spreading within predicted range (~4 s) is consistent with our experimental observation that at about 4 s of the spreading the bulk source material has been completely absorbed into surface roughness, which means the filling condition would be changed afterward as assumed.

Table 5.1: The initial size of the source material, the final spreading radius and the ratios of the final radii x / y .

Test No.	Initial radii (mm)	Final spreading radii (mm)	Directional spreading ratio: $R_{di} (x_f/y_f)$
Test 1	$x_0 = y_0 = 0.23$	$x_f = 4.22$ $y_f = 2.87$	1.47
Test 2	$x_0 = y_0 = 0.18$	$x_f = 3.28$ $y_f = 2.35$	1.40

Table 5.2: Selected filling factors, a prediction range and associated average relative errors of the prediction.

Test No.	Selected filling factor range	The percentage range of the predicted spreading	Average relative error
Test 1	$\eta_{0,x}: 0.9 - 1.0$ $\eta_{0,y}: 0.5 - 0.7$	$x / x_f: 13 - 57\%$ $y / x_f: 15 - 54\%$	x direction: 7–10% y direction: 6–9%
Test 2	$\eta_{0,x}: 0.7 - 0.9$ $\eta_{0,y}: 0.3 - 0.4$	$x / x_f: 14 - 58\%$ $y / x_f: 16 - 49\%$	x direction: 6–10% y direction: 7–9%

In capillary-viscous-asymptotic stage, which is taking place from ~ 4 up to ~ 35 seconds of the process, the kinetics of spreading in the x (preferential) direction and in the y direction don't obey Washburn law and are described by $x \sim t^{1/n}$ and $n \approx 5$. Asymptotic endings appear at the very end of the spreading, as expected.

5.5 Summary

Preferential spreading of molten Sn-Pb alloy on IMC2 and IMC3 Cu_6Sn_5 intermetallic substrates was studied and elliptical spreading patterns were noticed. It is experimentally proved that the spreading is preferential due to the grain orientation of the intermetallics.

Moreover, the kinetics is governed by topographical features of the surface, which can be characterized with porosity/tortuosity experimentally. Note that a surface uniform roughness as can be characterized with porosity/tortuosity by using geometrical method as studied in Chapter 4; a random (or non-homogeneous) surface roughness, as studied in Chapter 3 and this chapter, can be characterized with porosity/tortuosity by 3D surface profiling and AFM (a similar discussion is provided in Section 3.5 in Chapter 3). It is demonstrated that the IMC3 has a more pronounced preferential orientation compared to the IMC2 so the imbibition on it indicates a larger extent of anisotropy in terms of a larger directional spreading ratio. This offers a possible method to control or tune the flow of molten metal by an alteration of the surface topography, induced by grain growth.

It has been established that the early state of the imbibition of molten metal is driven by the capillary force and retarded by the viscous force. The kinetics is described based on the mass conservation principle and the spatial difference of the topographical

features (as porosities/tortuosities at two different directions) and thus a Washburn-type relation can be obtained as a result. Note that the model in this chapter, different than that in Chapter 3 and 4, is established without introducing Darcy's law as a momentum equation and the permeability as a factor that describes the topographical features. For a radial spreading (sessile drop) configuration, the central material source is of a finite mass and the spreading will be slowed down by the exhaustion of the liquid source. The height of liquid metal contained in the roughness composed of microstructures will decrease over time thus reducing the capillary driving force.

Finally, a theoretical model was established to describe the kinetics of spreading of molten metal in both preferential and non-preferential directions over a complex microstructured rough surface, during the capillary-viscous stage (up to ~4 seconds) with an average relative error of 6% – 10% for a selected range of filling factors.

CHAPTER 6: EXPERIMENTAL STUDY OF REACTIVE WETTING OF AgCuTi FILLER METAL ON TOPOGRAPHICALLY MODIFIED TiAl – BASED ALLOY SUBSTRATES[§]

6.1 Overview

In order to extend our focus to a physical system that does not necessarily feature Washburn-type of spreading typical for non-reactive systems, this chapter addresses an experimental study of a reactive wetting at high temperatures. Different from the previous chapters, i.e., Chapter 3, 4 and 5, which deal with soldering materials at low temperatures with a maximum suppression of chemical reactions, this chapter deals with a wetting associated with strong chemical reactions for brazing materials at a much higher temperature level. The reactive wetting kinetics on both rough and polished surfaces has been considered. Additionally, the interface conditions and formed microstructures, which are associated with strong chemical reactions between a molten metal and a substrate, were briefly but sufficiently identified in order to support the analysis of the wetting kinetics.

A reactive wetting of AgCuTi over a TiAl substrate was investigated *in situ* by hot stage microscopy under a protective atmosphere of a high purity argon at an elevated temperature (~1270 K level). Experimental results involving movement of the triple line indicate that the wetting process of molten AgCuTi alloy on both polished and rough surfaces features similar kinetics. This may be counter-intuitive, because we have established for non-reactive cases a significant impact of the topographical features of the substrate on the kinetics of the triple line movement. In the case of here considered reactive spreading three wetting stages were identified, (i) the initial stage upon the onset

[§] This chapter includes detailed account of material summarized in *Applied Surface Science*, Vol. 259, 2012, pp 343-348

of melting, characterized by a triple line that is essentially stationary or even in some cases slightly contracting, (ii) the middle stage featuring almost linear spreading kinetics, and (iii) the asymptotic stage with a kinetics with a diminishing spreading rate. Hence, wetting kinetics within the main spreading stage features the power law of $R^n \sim t$ ($n=1$), which is designated as a linear spreading. During the spreading, Ag-based solid solution and Al-Cu-Ti ternary intermetallics were formed beneath the molten metal at the interface within the joint zone (Li et al., 2012). The spreading of AgCuTi filler over TiAl is proved to be highly reactive and the topographical modification of the base metal surface appears to have a minimal impact on the wetting kinetics. This was demonstrated in simultaneous spreading tests by using both polished and rough substrates through the not sizable movement of the triple line.

6.2 Materials and Experimental Procedure

6.2.1 Materials Selection

The wetting system studied in the set of experiments considered in this chapter includes (i) TiAl (Ti-46.5Al-2.5V-1.0Cr, mole %) as a base metal, and (2) AgCuTi (Ag-33Cu-4.5Ti, wt.%) as a filler metal. TiAl intermetallics-based alloy (TiAl) is regarded as one of the candidates for many high temperature applications, especially in manufacturing of moving parts of automobile and aircraft engine components (Yamaguchi et al., 2000; Wilfried et al., 2009; Clemens and Kestler, 2000). It would be of significant importance to study wetting of molten filler metals on TiAl under controlled atmosphere as brazing is one of the most widely used methods for bonding TiAl in dissimilar materials assemblies (Noda, 1998). Unfortunately wetting and

spreading of a molten filler metal, i.e., a AgCu system, over the TiAl substrate under a controlled atmosphere have been seldom studied most likely because vacuum environment has been used often as more appropriate (Li et al., 2006; Lee et al., 1998; Shiue et al., 2003; Shuie et al., 2004).

In this chapter, we present an experimental study of the wetting kinetics of the AgCuTi filler metal during spreading over the TiAl substrates having distinct topographical features in a high purity argon protective atmosphere. The main focus of this study is to (i) examine the reactive wetting behavior of a molten AgCuTi filler on a TiAl substrate, and (ii) explore a possible impact of topographical alterations on the wetting kinetics for such a reactive wetting system.

6.2.2 Experimental Procedures

Real-time *in situ* observations of the spreading of the molten AgCuTi filler metal over TiAl, and associated quantitative measurements of the spatial distribution of the spread were utilized to analyze the kinetics of the triple-line movement. The *in situ*, real time monitoring was performed by using hot-stage microscopy as described in earlier chapters. A substrate coupon made of TiAl, having overall square dimensions of 5.5 mm × 5.5 mm × 0.6 mm, was positioned within the hot zone chamber of the LINKAM TS 1500 stage installed on an OLIMPUS BX51 M optical microscope. A brazing filler metal, i.e. AgCuTi specimen in form of a solid pellet with dimensions of ~Φ1.8 mm × 0.05 mm, was positioned in the central domain of the TiAl substrate. The AgCuTi filler metal melting temperature range is 1023 K to 1073 K (Villars et al., 1995). Note that this

filler metal has a laminate structure with AgCu eutectic outer layers sandwiching the central Ti layer, as indicated in Figure 6.1.

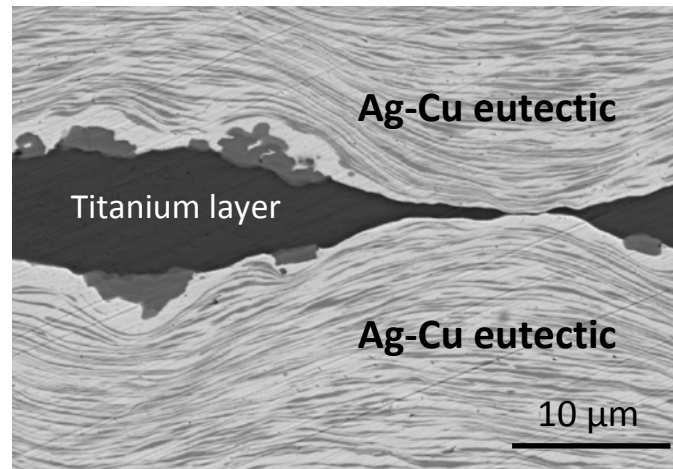


Figure 6.1: Microstructure of a cross-section of the AgCuTi brazing filler metal, showing a AgCu/Ti/AgCu sandwich structure. (Li et al, 2012)

TiAl substrate's surface was either additionally roughened using mechanical grinding with a 500# SiC sandpaper (the achieved roughness $R_a = 0.256 \pm 0.016 \mu\text{m}$) or alternatively polished with a $3 \mu\text{m}$ suspension ($R_a = 0.009 \pm 0.002 \mu\text{m}$) so that an impact of surface roughness of a topographically altered interface can be assessed. Surface roughness measurements were performed over an area of $0.27 \text{ mm} \times 0.27 \text{ mm}$ at various locations on TiAl substrates by a ZYGO New View 7500 system in ambient atmosphere. Figure 6.2 shows the topographical details of both rough and polished TiAl substrates.

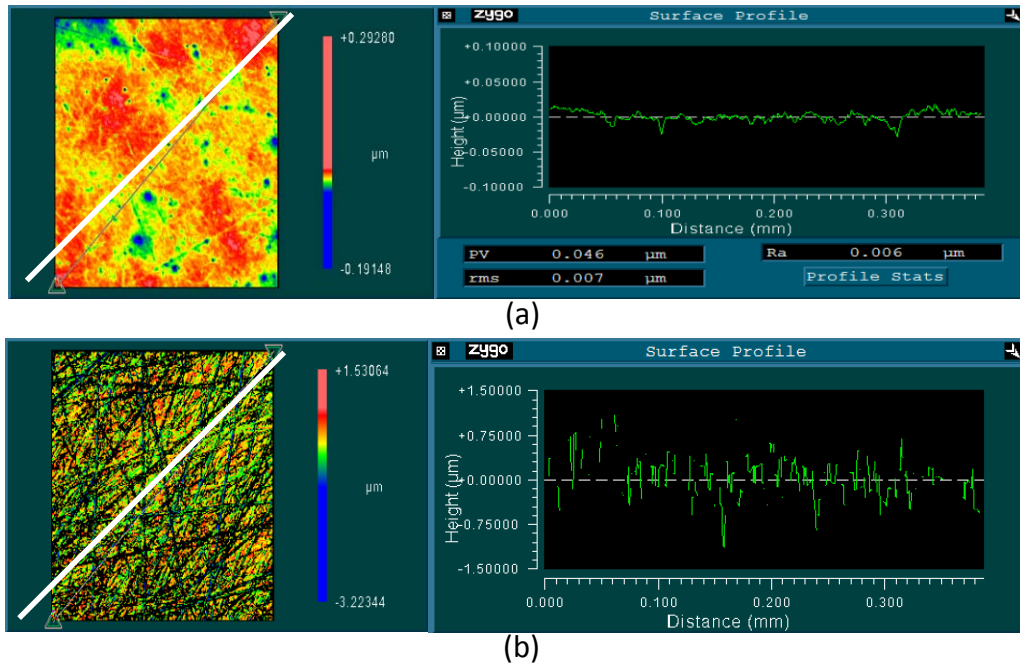


Figure 6.2: (a) Topographical details of a polished TiAl surface. (b) Topographical details of a rough TiAl surface.

All the spreading tests with the hot stage microscopy were conducted as already indicated in ultra high-purity argon atmosphere. The hot-stage chamber was purged with ultra high purity argon (99.999%) for about 15 hours (which was sufficient for about 300 chamber volume replacements) before initiation of the heating cycle. The heating cycle consisted of a ramp up, dwell at the peak, and a quench, which is given in Figure 6.3. The heating ramp-up was executed with 120 K/min and the cooling ramp-down rate was 100K/min. The peak temperature and dwell time were set to be 1273 K and 2 min, respectively. Temperature stability at the peak was at the 1 K level. The uncertainty of the brazing filler metal surface temperature exposed to heating cycle was dependent on thermal resistance between the stage surface, TiAl substrate, and the brazing filler metal sample. The discussion of the impact of these resistances is offered by Zhao (Zhao, 2005) for the hotstage microscopy for the low temperature test cases. In this case, at higher

temperatures, the impact would be influenced additionally by reaction. This topic will be considered elsewhere.

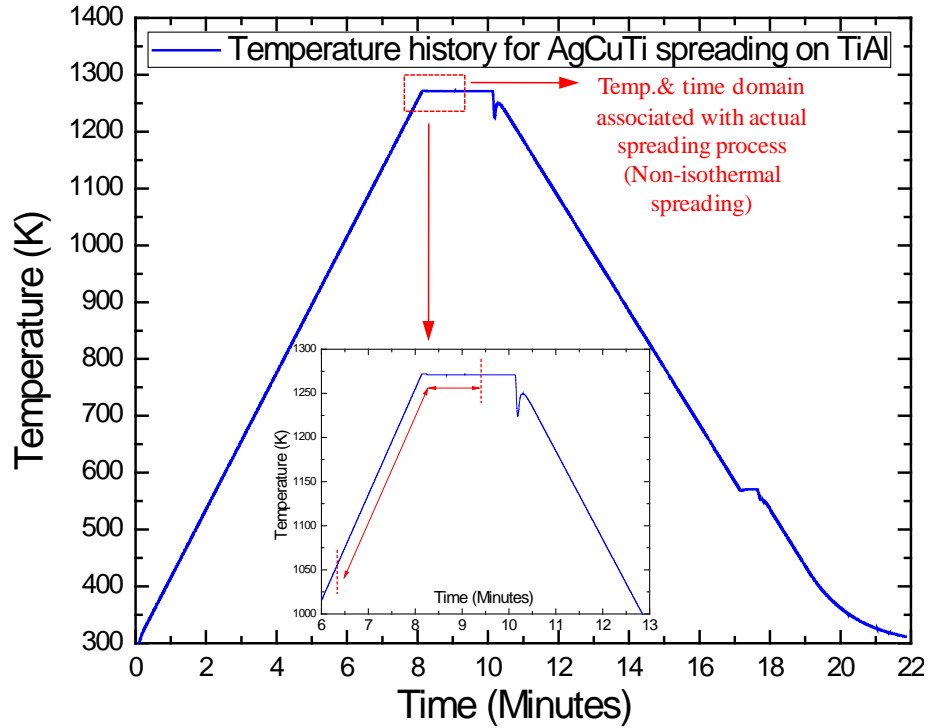


Figure 6.3: Heating cycle for spreading tests for AgCuTi – TiAl reactive wetting system

During the heating/dwell/cooling segments of the cycle, digital film recording was performed by using a camera system with a 22 frames/s. Movie clips were subsequently decomposed into individual frames, and were associated with the corresponding, digitally recorded, temperature histories. The triple line was closely approximated with an equivalent radius of the sessile drop instantaneous locus of points, representing the molten metal spread perimeter. Measurements of the triple-line locations were performed using Image-Pro PLUS software. The uncertainty in determining linear dimensions was less than 3% for the given length scale.

6.3 Results and Discussions

6.3.1 Phenomenological Observation and Experimental Data

This section provides an in situ real time phenomenological observation and quantitative data for a wetting of molten AgCuTi on both polished and rough TiAl substrates. The data sets for the purpose of studying wetting kinetics (which will be discussed in details in Section 6.3.3) are presented in Appendix H, Table H4. The wetting phenomena will be interpreted based on the experimental observation and the obtained data sets of wetting kinetics. No modeling of the process is included.

Wetting and associated spreading processes of the molten AgCuTi alloy on both polished and rough surfaces feature the same sequence of events. Figure 6.4 shows a typical sequence of instantaneous images during AgCuTi alloy spreading on a polished TiAl. As indicated in Figure 6.4 (a), the AgCuTi braze solid pellet was of a roughly circular shape. Upon heating to the temperature in the neighborhood of the melting point, the filler pellet contracts slightly upon initial melting, Figure 6.4 (b). With continuing heating within the range of 1223 K – 1263 K, Figure 6.4 (c), the spreading features an increasing rate (note the liquid bulk appears as being to a less significant degree a mixture of liquid and solid phases). Figure 6.4 (d) indicates the spreading reaching the asymptotic limit at the dwell temperature. During the dwell time, the braze has consolidated the spreading area, Figure 6.4 (e). At the end of the cooling process, the re-solidified AgCuTi layer over TiAl appears as in Figure 6.4 (f).

It should be noticed that the spreading studied in this chapter is non-isothermal spreading. The melting point of the AgCuTi filler is about 1063 K which is lower than

our peak ($\sim 1273\text{K}$). It is assumed in this study that the temperature has a minimal impact on the liquid properties (i.e., surface tension, density and viscosity)

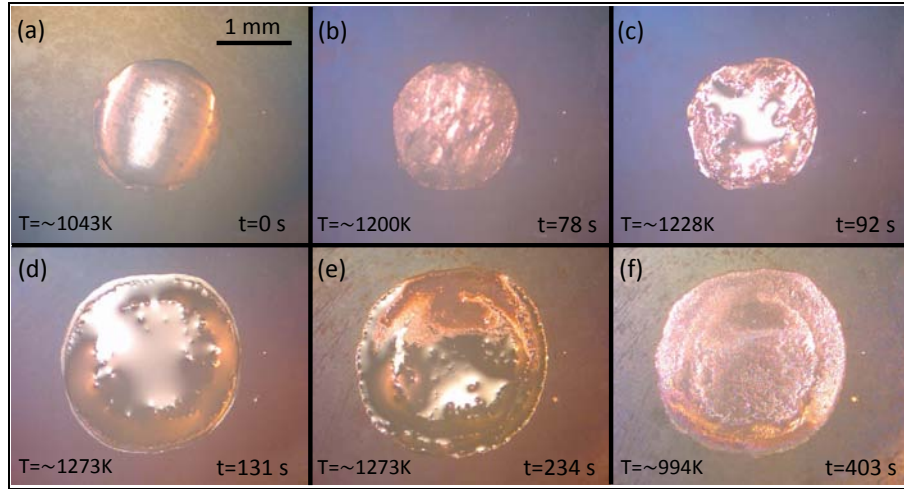


Figure 6.4: A sequence of instantaneous frames during AgCuTi braze spreading on the polished TiAl substrate: (a) before melting (b) after the onset of melting (c) after the onset of spreading (d) an advanced period of spreading (e) initial re-solidification (f) complete re-solidification

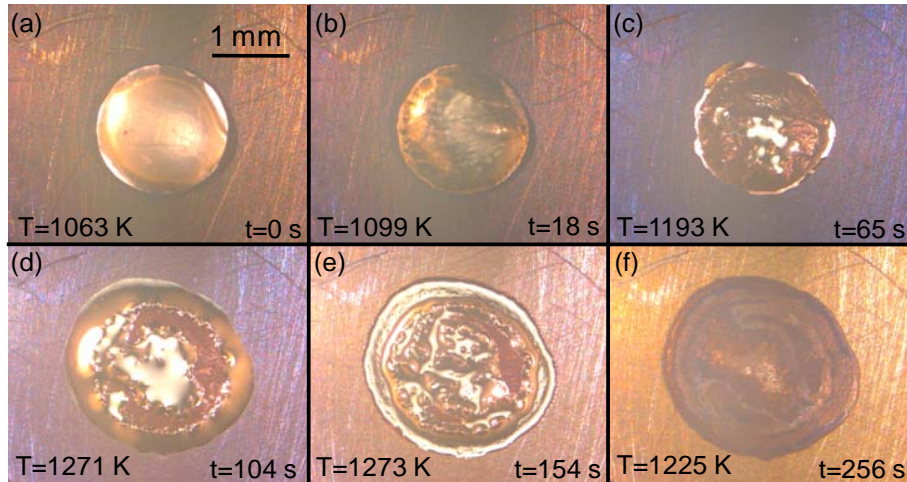


Figure 6.5: A sequence of instantaneous frames during AgCuTi braze spreading on the polished TiAl substrate. Insets represented the same set of events as in Figure 6.4.

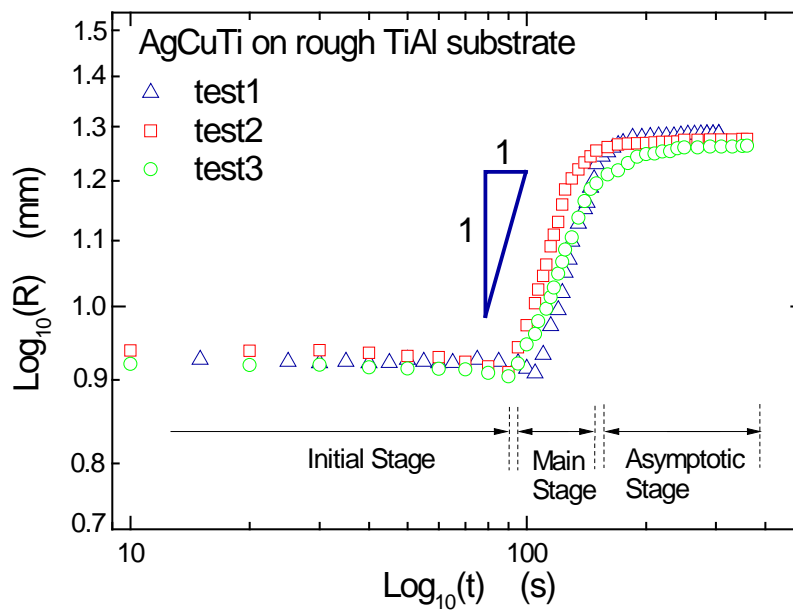
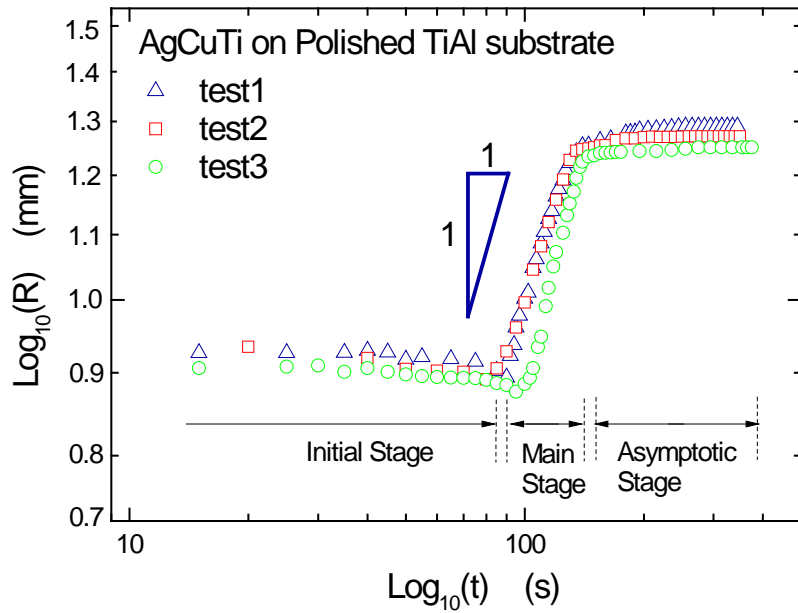


Figure 6.6: Kinetics data in a logarithmic scale of the triple line for the AgCuTi filler metal spreading on: (a) a polished TiAl substrate, (b) a rough TiAl substrate (from melting through solidification). Note: the temperature associated with the origin of the abscissa is 1043 K (before the onset of melting)

Figure 6.5 shows a sequence of instantaneous images during AgCuTi alloy spreading on a rough TiAl surface. Note that the similar experimental phenomena were noticed as mentioned for AgCuTi spreading on a polished TiAl surface.

In Figure 6.6 (a) and (b), the equivalent spreading radius versus time plots in a logarithmic scale are presented for the wetting systems of the AgCuTi brazing filler metal on the polished and rough surfaces of TiAl, respectively. The time at the abscissa origin is associated with a temperature of 1043 K. The actual melting temperature of AgCuTi filler in this study is observed to be around 1063K. It can be noticed that the wetting kinetics of AgCuTi alloy on (i) polished and (ii) rough surfaces are similar in the sense that the spreading radius decreases slightly during the initial stage of the melting, and subsequently increases with a large spreading rate until approaching an asymptotic value.

In accordance with experimental observations and data sets shown in Figure 6.5, the entire spreading process is proposed to be divided into three stages by different slopes established by data points as indicated in a log-log scale:

(i) Initial stage (associated with data points of a near zero slope in a log-log scale).

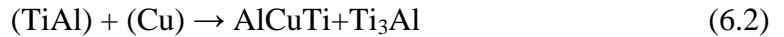
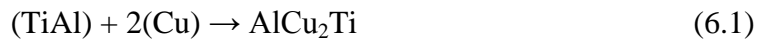
In this stage the filler metal has melted gradually within the melting temperature range with the molten filler contracting slightly due to adverse wetting conditions at the onset of spreading indicating a contact angle larger than 90° in that phase of spreading. The poor wetting can be attributed to the influence of the oxide layer on the surface of TiAl. It is well known that TiAl easily reacts with N, H, O (Shen et al., 2001). The oxide layer formation can be traced from two sources: (a) oxidization of the TiAl during polishing and roughening in air when the samples were prepared, and (b) oxidization during the heating process as traces of oxygen exist in the heating chamber of the hotstage,

regardless of a thorough purging with argon. Therefore the molten AgCu braze is actually in contact with the oxide layer on TiAl surface at the very beginning of the spreading process. The similar behavior of poor wetting is also noted by other authors (Gale et al., 1999; Shen et al., 2001), for a filler (Ag, Cu, Al) / preoxidized TiAl system, where metal-metal contact during the initial stage of spreading was hampered by oxide films formed on the TiAl substrate. In this chapter, the contracting behavior of the liquid braze (AgCuTi) associated with a large contact angle (at least $> 90^\circ$) is fully consistent with the conclusion in (Eustathopoulos et al., 1999) that the contact angle falls in the range of $\sim 110^\circ$ – 140° for a non-reactive metal system over an oxide system. It should be noted that the dissolved reactive-Ti in molten braze is of a small amount and it exists within the center domain within the filler (as indicated in Figure 6.1), therefore it doesn't reach the interface at this early stage.

(ii) Main spreading stage (featured by a slope of 1 as the data points indicate in a log-log scale). As the temperature is rising, i.e., higher than ~ 1173 K, the decomposition of the titanium and aluminum oxides on the TiAl surface starts (Schmiedgen et al., 2002) and meanwhile the reaction, i.e., the dissolution of Ti element is assumed to become more intensive. When the temperature of the wetting system has reached about 1243 K - 1263 K, an onset of significant spreading takes place. The noticed transition from the poor wetting behavior in the initial stage to the rapid spreading can be attributed to the change of the contact angle of the liquid metal on the oxide layer on TiAl surface and a clean metallic TiAl (Eustathopoulos et al., 1999). In this stage, the oxide film on TiAl surface is decomposed due to both the high temperature (Schmiedgen et al., 2002) and the effects of Ti element at the interface. Subsequently the direct contact of molten AgCu

and clean TiAl metallic surface is established, thus forming a small contact angle ($< 90^\circ$) for a metal/metal system as advocated in (Gale et al, 1999). This transition, usually fast, of a contact angle of a metal/oxide system ($> 90^\circ$) to a contact angle of a metal/metal system ($< 90^\circ$), is in agreement with our and other observations of the onset of the rapid spreading (Eustathopoulos et al., 1999).

During the subsequent ~ 50 s, the triple line of molten AgCuTi filler has advanced with a large constant spread rate (that is, a linear R vs. t relation with a stiff slope as presented in Figure 6.5). The constant spreading rate, as reported in (Calderon et al., 2009) for the spreading of AlSi alloys on carbon, featured a wetting controlled by the chemical reaction within the local triple line domain. In our case, after the contact angle transition, the direct contact of TiAl metallic surface and the molten AgCuTi filler triggers chemical reactions between TiAl and Cu as indicated by equation (6.1) and (6.2), see below, (Villars, 1995). These reactions have been verified by many other studies (Li et al., 2006; Lee et al., 1998; Shiue et al., 2003; Shuie et al., 2004) and are listed as follows



The specific interface chemical reactions (proved by EDS analysis as it will be stated later in Section 6.3.2) and the constant moving rate of the triple line herein is consistent with the statement associated with the linear spreading for the spreading of AlSi alloys on carbon as reported in (Calderon et al., 2009). Additionally, as it has been

reviewed in Section 2.4.3.1 in Chapter 2, the kinetic of a reactive spreading will follow a linear relation (Equation (2.35)) for a number of reactive wetting systems (Kumar and Prabhu, 2007). It should be noticed that the main stage associated with a constant and large spreading rate covers up to ~ 95% of the total spreading domain.

(iii) Asymptotic stage. A reduced concentration of Cu in AgCuTi molten filler due to the consumption of Cu during the main spreading stage (Cu concentration: original 28 wt.%, after spreading $\sim 6.23 \pm 2.06$ wt.%, confirmed by the EDS analysis, see Section 6.3.2, leads to a decreased chemical reaction rate between TiAl and Cu. Consequently the spreading of the molten filler gradually slows down and ultimately, through the final asymptotic stage, reaches the maximum spread area and spreading termination. The final contact angle of the re-solidified braze on the TiAl substrate was determined to be $\sim 30^\circ$ with multiple measurements at arbitrary locations of the triple line domain after solidification, by using the Image-Pro PLUS software. This value is within the empirical range for the wetting of metal/metal systems suggested by Eustathopoulos et al (Eustathopoulos et al., 1999).

The depletion of Cu from the liquid phase causes (1) an asymptotic slowing down and ultimate termination of the spreading process (note that the exhaust of the liquid source may be another reason for the asymptotic termination of the spreading); (2) re-solidification of the edge domain of the filler dominated by Ag and Ti. It should be noted that at the peak temperature of 1273 K, which is much higher than the melting point of pure Ag, the re-solidification of the edge domain of the filler still takes place confirmed by the experimental observation as indicated in Figure 6.4. The possible reason for such a

re-solidification is that Ag-Ti alloy is in a solid phase when concentration of Ti is higher than ~6% in accordance with Ag-Ti binary phase diagram (Appel et al., 2011).

6.3.2 Microstructure Analysis

The microstructure analysis offers a better understanding of the interface configuration that is used to identify the reactive wetting conditions. It offers an evidence for the characterization of the chemical reaction products or intermetallic layers at the interface which may have impacts on the reactive spreading process. Figures 6.7 (a) and (b) show a top view of a resolidified AgCuTi filler metal by using Scanning Electron Microscopy (SEM). A line scan analysis, conducted by using Energy Dispersive Spectroscopy (EDS), across the radial direction of the filler spread over the substrate's surface is marked in Figure 6.7 (b). Figures 6.7 (c) and (d) present the microstructure at the interface of an AgCuTi filler metal brazed on TiAl away from the triple line and in the triple line domain, respectively. The observations are as follows.

It is noticed that the resolidified filler metal features a fairly regular circular triple line shape, as can be seen in Figure 6.7 (a). The main elements content, i.e. Ti, Ag, Cu, changes (approximately no change for Ti and a slight decrease for Ag and Cu) from the center to the edge of the resolidified AgCuTi braze filler, as documented in Figure 6.7 (b). Furthermore, on the surface of the filler residue there is a minimal amount of Al, and the Ti concentration is much higher than that of the Cu. Such a lower concentration of Cu element could be attributed to its consumption by the associated chemical reactions, as indicated in Equations (6.1) and (6.2), during the wetting and spreading process. Namely, Cu element easily reacts with TiAl and forms AlCu_2Ti phase at high temperatures and

with a prolonged dwell time, the Al-Ti-Cu ternary intermetallics products, i.e., AlCuTi, Ti₃Al and Al₄Cu₉, will form consequently (Villars, 1995). Figures 6.7 (c) and (d) clearly indicate Al-Cu-Ti ternary phases thus confirming the presence of AlCu₂Ti and AlCuTi+Ti₃Al intermetallics at the interface. The reaction products between TiAl and AgCu based alloy have been studied in detail by Li *et al.* (Li et al., 2006). The reaction products were analyzed and confirmed by using the SEM (S-3200-N HITACHI) and the EDS (EVeX-EDS system).

It is noted that the spreading front is irregular spatially at the micro scale, as can be seen in Figure 6.7 (d). During the spreading process, the elements distribution across the interface was changed due to the substrate dissolution into the molten filler, inter-diffusion and chemical reaction between the substrate and the molten filler (as indicated in Equations (6.1) and (6.2) and Figure 6.6 (d)). The detailed study of the interface between an AgCuTi filler and a TiAl substrate was reported by Li et al (Li et al., 2006). More Cu from the filler metal had been continuously consumed, and Ti and Al from the TiAl had been dissolved into the molten filler. In the early stage of the spreading, Cu element was rich enough to support the chemical reaction and the spreading process; however, in the later stages of the spreading, there was not enough Cu especially at the spreading front. As mentioned in Section 6.3.1, as Ti concentration increases Ag-Ti alloy becomes solid after the concentration of Ti gets higher than ~6%, according to Ag-Ti binary phase diagram (Appel et al., 2011). The spreading process would then be affected by an earlier solidification of the front zone and the remaining molten filler would be confronted with an already solidified spread edge. Thus, the irregular morphology of the zone would be formed.

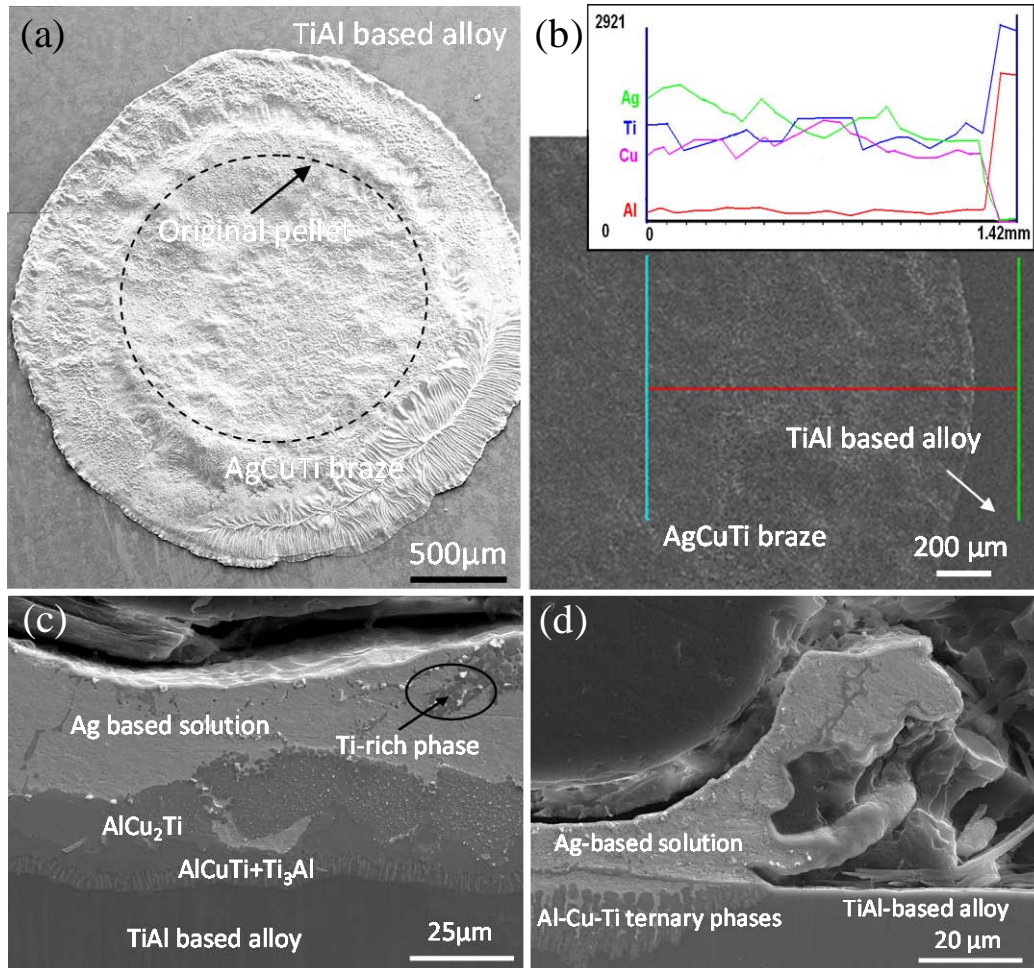


Figure 6.7: (a) Top view of a re-solidified AgCuTi filler metal. (b) The line scan analysis of the main elements, distribution across the radial direction of the re-solidified braze. Microstructure of the interface of the AgCuTi filler metal brazed on TiAl (c) the cross section within the central domain of the re-solidified filler metal (d) the cross section within the edge domain of the resolidified filler metal.

6.3.3 Phenomenological Analysis of Wetting Kinetics

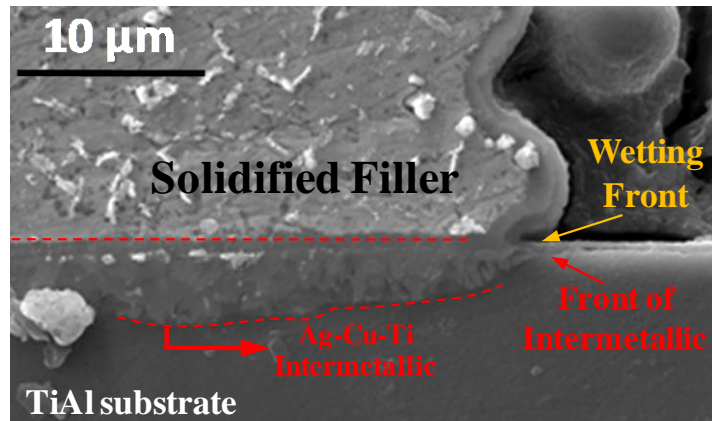
For non-reactive solid/liquid systems the dynamics of wetting/spreading of sessile drop on both smooth and rough/structured solid surfaces has been relatively well studied (de Gennes, 1985; Quere, 2008). A model describing wetting of silicon oil on a glass

surface (Tanner, 1979) was successfully devised long ago with $R^n \sim t$, $n = 10$, as we have reviewed in Section 2.1.3 in Chapter 2. Non-reactive wetting on a rough/structured surface follows in most cases a Washburn-type relationship (Washburn, 1921). For example, spreading of a liquid metal and organic liquids over a rough inert surface is characterized with $R^n \sim t$, $n = 2$ as indicated in the previous chapters, i.e., Chapter 3, 4 and 5, (Liu and Sekulic, 2011; Liu et al., 2011a; Liu et al., 2011b; Liu et al., 2012). In this chapter, the spreading of molten AgCuTi filler on both polished and rough TiAl substrates features kinetics of the similar power law, apparently with n equal to neither 2 nor 10, as indicated in Figure 6.4. The focus in this study is on the main stage of the spreading process, which covers ~95% of the spreading radius.

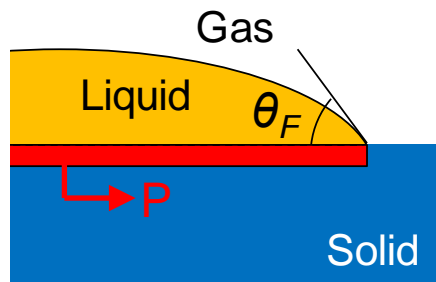
It can be noticed in Figure 6.6 that within the main stage of spreading, a constant triple line velocity ($U = dR / dt$) has been observed which will lead to the relation $R^n \sim t$ with $n \sim 1$. The similar relation of R vs. t was also reported in (Dezellus et al., 2003; Landry and Eustathopoulos, 1996) for reactive wetting controlled by the reaction process at or close to the triple line, which is consistent with our hypothesis that the spreading of AgCuTi on TiAl is controlled by a chemical reaction.

In accordance with the results of the interface characterization advocated in Section 6.3.2, Figure 6.8 offers an experimental evidence that supports the linear wetting kinetics ($R \sim t$) for such a reactive wetting system. Figure 6.8 (a) offers a SEM image for a cross section of the wetting front domain for such an AgCuTi – TiAl wetting system after the resolidification. It can be noticed that the resolidified filler is sitting on but not exceeding over the intermetallic layer front formed between the filler metal (Ag-Cu-Ti) and the base metal (Ti-Al). The configuration is the same as it is for a reactive wetting

case that is dominated by chemical reactions, as introduced in Section 2.4.3 in Chapter 2. Figure 6.8 (b), which is extracted from Figure 2.17(b), offers a scheme of such a configuration for reactive wetting. Therefore it can be stated that the reactive wetting of molten AgCuTi on a TiAl substrate is dominated by chemical reactions.



(a)



(b)

Figure 6.8: (a) solidified AgCu filler sits on the production of chemical reaction at the interface, (b) a wetting configuration for reactive wetting system described in Chapter 2 (Figure 6.6 (b) is extracted from Figure 2.17 (b))

Note that the same $R^n \sim t$ ($n \approx 1$) relation for both polished and rough substrates in this study indicates that during the spreading controlled by chemical reactions the surface topography appears to have a small impact on the kinetics of the triple line. Therefore, in such a reactive wetting/spreading process, strong chemical reactions rather than surface topographical features may dominate.

6.4 Summary

Spreading experiments of the AgCuTi filler metal over a TiAl (TiAl) substrate under controlled high-purity argon atmosphere were carried out at elevated brazing temperatures by using advanced high temperature hot-stage microscopy. Triple line movement of molten AgCuTi filler on both polished and rough TiAl substrates feature the same spreading behavior in accordance with the empirical kinetics data. The spreading process can be divided into three stages: (i) the initial stage, (ii) the main spreading stage, and (iii) the asymptotic spreading stage. Within the main spreading stage, the constant slope of the triple line movement was obtained featuring a linear relationship between the equivalent triple line radius and time, $R^n \sim t$, $n \approx 1$. An evidence of the presence of Ag-based solid solution and Al-Cu-Ti ternary intermetallics, i.e. $Ti_3Al+AlCuTi$ and $AlCu_2Ti$ phases at the interface between the residue filler metal and TiAl substrate is established, which is consistent with a linear reactive spreading behavior as reported for other reactive wetting systems, i.e., for the spreading of AlSi alloys on carbon as reported in (Calderon et al., 2009). Moreover, as it has been reviewed in Section 2.4.3.1 in Chapter 2, the kinetic of a reactive spreading will follow a linear relation (Equation (2.35)) for a number of reactive wetting systems (Eustathopoulos et

al., 1999). This study, an AgCuTi/TiAl brazing case, indicated that the topographical modification of base metal surfaces may have a minimal impact on wetting kinetics of the braze providing the wetting is dominated by the Al-Cu-Ti ternary chemical reaction within the triple line domain.

The spreading of AgCuTi filler over TiAl is proved to be highly reactive due to a pronounced formation of intermetallics within the interface domain, Figure 6.7 and 6.8. The topographical modification of the base metal surface appears to have a minimal impact on the wetting kinetics as demonstrated by the *in situ* observation and analysis of reactive spreading tests using both polished and rough substrates, as indicated in Figures 6.4, 6.5 and 6.6.

CHAPTER 7: CONCLUSIONS AND FUTURE WORK

In this Chapter, the last chapter of this dissertation, the results of the current research and associated contributions are summarized with a few final remarks. The recommendations for the future work are discussed briefly based on the study offered in this dissertation.

7.1 Main Conclusions

In this dissertation, an imbibition phenomenon has been experimentally registered for several representative liquid systems, i.e., low temperature organic liquids and elevated temperature molten metals' spreading over topographically modified intermetallic surfaces. A Washburn-type theoretical modeling framework has been established for both isotropic and anisotropic non-reactive imbibition of liquid systems over rough surfaces. The roughness domain of the surfaces has been considered as a porous-like medium and the associated surface topographical features have been characterized either theoretically or experimentally. Empirical data have been utilized to verify the theoretical framework. The agreement between theoretical predictions and empirical data appears to be good (i.e., the relative error of the prediction for planar spreading of organic liquids is up to 8%, for axisymmetric and anisotropic spreading of liquid metals is up to 15%). Moreover, a reactive wetting in a high temperature brazing process has been studied for both polished and rough surfaces. A linear relation between the propagating triple line and time has been identified and the wetting is therefore proved to be dominated by a strong chemical reaction. Hence, the major findings and contributions are summarized as follows:

1. A theoretical framework was established for modeling of either an imbibition of low temperature liquids, i.e., organic liquids or molten metals, over rough surfaces. The imbibition phenomenon is modeled as a non-reactive fluid penetration of the micro layer of liquid along a two-dimensional porous-like medium domain, which is either spatially isotropic or anisotropic. The validity of the Darcy's law has been assumed with both intrinsic permeability and associated porosity/tortuosity determined from the characterization of surface topography. The imbibition of liquids on a rough surface was expressed in terms of (i) the surface topography (i.e., permeability, tortuosity/porosity and geometry of micro-channel cross section); (ii) wicking features (i.e., contact angle and filling factor); and (iii) physical properties of liquids (i.e., surface tension and viscosity). The filling factor is the only assumed parametrically changing empirical input for the theoretical model. It is found that the filling factor is the same constant for various organic liquids for the imbibition on the same type of IMC0 rough surfaces with an infinite liquid source. For a sessile drop configuration with the finite mass source, the filling factor for the imbibition is a function of the imbibition distance and associated time. At main evolution stage of the imbibition the filling factor can be assumed to be a constant.
2. The practical approach to the characterization of a surface roughness was introduced. Topographic features such as those of an in house fabricated intermetallic substrate, i.e., IMC0, with a surface roughness composed of irregular surface structures (but uniformly distributed) can be experimentally determined

with surface roughness, permeability and porosity/tortuosity by using Atomic Force Microscopy (AFM) and 3D optical surface profiling. For the surface topographical features with a certain spatial orientation, such as for IMC2 and IMC3, AFM can be used to determine the surface roughness with the specific porosity and tortuosity. For the surface topographical features with relative regular shape and uniformly distributed, such as IMC1, a geometrical methods can be used to characterize the surface roughness: topographical features are simplified with regular polyhedrons so that parameters associated with surface roughness could be calculated.

3. The kinetics of a planar-type of wicking of a set of five different organic liquids over rough surfaces in the gravity field positioned vertically, in absence of chemical reactions and with a negligible gravity influence, is described by a theoretically established model of a Washburn type. An excellent agreement (with a relative error in the range of 4% to 8%) between theoretical prediction and experimental data, both of which show a z vs. $t^{1/2}$ relation, verifies the validity of the theoretical model. Scaled data indicate that for a specific rough surface, wicking kinetics of considered liquids depends on surface tension to viscosity ratios, and the formed equilibrium contact angles. Filling factor is determined to be within the range from 0.9 to 1.0. Empirical data indicate that for a rough surface (as in the case of IMC0) the filling factor keeps the same value for a capillary rise phenomenon for a variety of liquids.

4. Isotropic (axisymmetric) spreading of liquid metal (eutectic and hypo eutectic Sn-Pb) over an intermetallic substrate ($\text{Cu}_6\text{Sn}_5/\text{Cu}_3\text{Sn}/\text{Cu}$) is described with developed theoretical model as a surface tension and viscosity driven flow over a rough surface with a suppressed reaction at the interface. The prediction generated from the model has a relative deviation from empirical data within the range of 5% to 15%. After the short time period featuring the inertial forces controlling spreading (between 0 and ~1-2 s after the onset of spreading), a 1/2 power law spreading phase takes place. Spreading terminates asymptotically upon exhausting the liquid metal source. It is demonstrated that such a model based on the theoretical framework would overestimate spreading kinetics in initial and final stages of spreading. Filling factor in this study is determined by mass conservation principle and assumed to be a constant during the triple line movement.

5. Preferential spreading of molten Sn-Pb alloy on IMC2 and IMC3 Cu_6Sn_5 intermetallic substrates was studied and elliptical spreading patterns were noticed. It is experimentally proved that the spreading is preferential due to the grain orientation of the intermetallics. Moreover, the kinetics is governed by the topographical features of the surface, which can be characterized with porosity/tortuosity. It is demonstrated that the IMC3 has a more pronounced orientation compared to the IMC2 so the imbibition on it indicates to a larger extent an anisotropy (in terms of a larger directional spreading ratio). This offers a possibility to develop a method to control or fine tune the flow of molten metal by

an alteration of the surface topography, induced by grain growth. It has been established that the early state of the imbibition of molten metal is driven by the capillary force and retarded by the viscous force. The kinetics is described by balancing those two forces during the central phase of the spreading and a Washburn-type relation can be obtained as a result. An analytical model was established based on the theoretical framework to describe the kinetics of spreading of molten metal in both preferential and non-preferential directions over a complex microstructured rough surface, during the capillary-viscous phase (of up to ~4 seconds) with an average relative error of 6%– 10% for a selected range of filling factors. For a radial spreading (sessile drop) configuration, the central material source is of a finite mass and the spreading has been slowed down by approaching an exhaustion of the liquid mass source. The height of liquid metal contained within the roughness features composed of micro-grains will decrease over time, thus reducing the capillary driving force. The associated filling factor is described as a function of spreading time and distance and simplified as a constant for the central stage of spreading.

6. Reactive spreading of the AgCuTi filler metal over a TiAl (TiAl) substrate under controlled atmosphere conditions with the high-purity argon atmosphere was studied *in situ* at elevated brazing temperatures. An evidence of the presence of Ag-based solid solution and Al-Cu-Ti ternary intermetallics, i.e. $Ti_3Al+AlCuTi$ and $AlCu_2Ti$ phases in the joint zone of the residue filler metal/TiAl is established. The Al-Cu-Ti ternary chemical reaction dominates the spreading process.

Spreading of molten AgCuTi filler on both polished and rough TiAl substrates feature similar behavior in accordance with the kinetics data. The spreading process can be divided into three stages: (i) the initial stage, (ii) the main spreading stage, and (iii) the asymptotic spreading stage. Within the main spreading stage, the constant slope of the triple line movement was obtained, featuring a linear relationship between the equivalent triple line locus of points radius and time, $R^n \sim t$, $n \sim 1$. This study, for the AgCuTi/TiAl system brazing case, indicates that the topographical modification of base metal surfaces may have a minimal impact on wetting kinetics of the braze providing the wetting is dominated by the chemical reaction within the triple line domain.

Overall, this study offers an innovative Washburn-type theoretical framework for modeling of an imbibition of low and high temperature systems (organic liquids or molten metals) over a rough surface by treating the rough domain as a porous-like medium. The study also provides theoretical and experimental methods for characterizing the surface roughness parameters. An insight is given to the potential tuning and control of the imbibition of the liquid phase for a manufacturing process. Additionally, a reactive wetting of a brazing material system was demonstrated and a linear evolution of spreading was registered.

7.2 Future Work

The following general statements regarding the future work can be advocated based on the experience gained during the execution of the current work.

1. Improve the theoretical framework for the imbibition of liquids over rough surfaces by a further elimination or reduction of an empirical input. More precisely, providing an analytical model for the filling factor magnitude and/or modeling approach to eliminate such a factor altogether would advance the applicability of the theoretical approach. The theoretical framework should be further studied for a multi-dimensional imbibition (or penetration) acknowledging true nature of permeability embedded in the Darcy's law as a second order tensor.
2. Identify the impact of non-isothermal or near-isothermal condition on the spreading process, such as liquid metal behavior during phase change and the spreading kinetics. The spreading of a molten metal in the current study is performed under effectively non-isothermal conditions (although within a pre defined temperature range) and the spreading model sensitivity on the property variability would be useful to consider.
3. A need for a study of the mechanism of the Cu_6Sn_5 intermetallic grains growth would be beneficial in order to understand the underlined physics that controls the process, important for a perceived potential to control the spreading preferentially.

The purpose would be to take a full control of the orientation of the roughness and associated molten metal flow.

4. A theoretical model, with a minimal empirical input, for a much more complex reactive wetting case still needs to be developed. The wetting kinetics appears to be linear ($R \sim t$) but the parameters that would be needed to determine the exact form of such a relation should be identified. Those parameters include surface tension and viscosity of the liquid metal, surface topographical features, chemical reaction rates (i.e., the kinetics of the interface phenomena description and the impact on the spreading evolution) and so on.
5. All theoretical models should be reconsidered in terms of non-dimensional parameters xxx. A scaling analysis on the relevant set of governing equations and boundary conditions should be revised.

APPENDICES

Appendix A

Bond number, Capillary length and the criteria for the negligible gravity effect

Bond number, a non-dimensional number that is defined as the ratio of gravity and the surface tension force, is expressed as (Bejan, 2004)

$$Bo = \frac{\rho g l^2}{\gamma} \quad (A1)$$

where for a liquid, ρ is the density, g is the gravitational acceleration, γ is the associated gas-liquid surface tension, and l is the characteristic length of the liquid.

If Bond number is small enough it means the gravity effect is sufficiently small compared to surface tension effect thus a negligible gravity. In such a case, we have

$$\frac{\rho g l^2}{\gamma} \ll 1 \Rightarrow \frac{\gamma}{\rho g} \gg l^2 \Rightarrow \sqrt{\frac{\gamma}{\rho g}} \gg l \quad (A2)$$

It is noticed that for a droplet on a surface, the associated characteristic length l can be considered as the base radius r . So with Equation B2 valid, we have

$$\sqrt{\frac{\gamma}{\rho g}} = \kappa^{-1} \gg r \quad (A3)$$

where κ^{-1} is defined as capillary length of the liquid (de Gennes et al., 2004).

Therefore if in the case that the capillary length of a liquid is much larger than the base radius of a droplet of such a liquid, the associated Bond number is also sufficiently small, thus a negligible gravity.

Determination of Bond number for capillary rise in Chapter 3, and radial imbibition for Chapter 4 and 5.

The Bond number associated with capillary rise of organic liquids in Table 3.3 in Chapter 3 is assessed for the liquid contained in an open triangular groove, as indicated in Figure A1 (a): $Bo = \rho g l^2 / \gamma = \rho g (V/A)^2 / \gamma \cong (2.1-2.7) \times 10^{-9}$. The volume of the liquid contained in a V-groove is represented as V and A is the free surface area of the liquid.

The Bond number associated with radial imbibition presented in Chapter 4 and 5 is for a sessile drop above the rough surface. The Bond number for Chapter 4 is assessed as: $Bo = \rho g (V/A)^2 / \gamma \cong 8.19 \times 10^{-3} < 0.01$. Bond number in Chapter 5 is: $Bo = \rho g (V/A)^2 / \gamma \cong 8.0 \times 10^{-3}$. Note that the volume of the molten metal drop is expressed as V and the free surface area of the drop is presented as A , as indicated in Figure A1 (b).

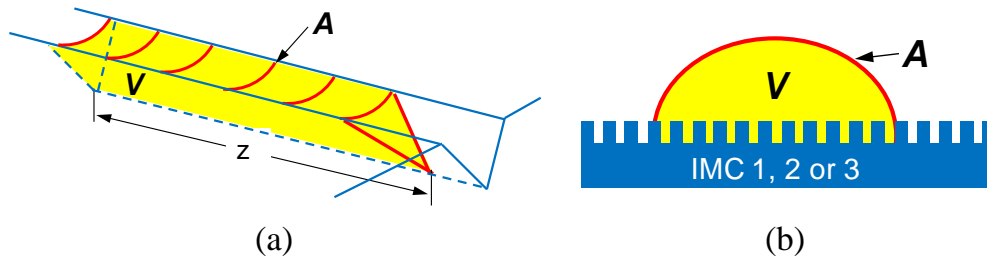


Figure A1: (a) Determination of Bond number for an open triangular groove, V and A represent the volume and free surface area of the liquid contained in a groove, respectively; (b) Configuration for a radial imbibition, V and A represent volume and free surface area of the liquid drop on a rough surface

Appendix B

No reaction between Cu_6Sn_5 and PbSn solder

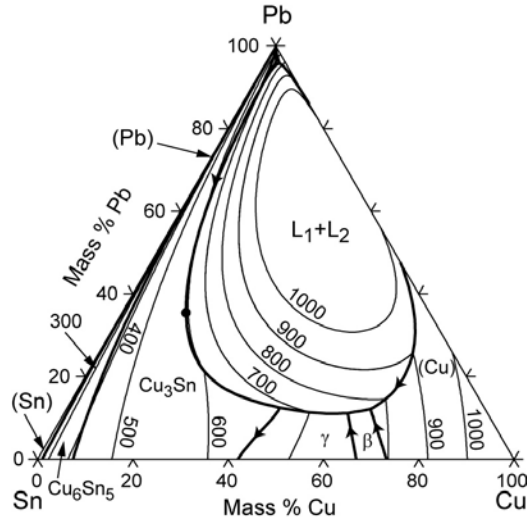


Figure B1: Sn-Pb-Cu ternary phase diagram (Bolcavage et al., 1995; Shim et al., 1996; Fecht et al., 1989; NIST, 2012).

Figure B1 provides a ternary phase diagram for Sn-Pb-Cu ternary system (Bolcavage et al., 1995; Shim et al., 1996; Fecht et al., 1989; NIST, 2012). Table B1 offers chemical reactions associated with Figure B1.

As the tests studied in Chapter 4 and 5 were conducted within a temperature range which is below $\sim 240^\circ\text{C}$, reactions 1-10 and 12 listed in Table B1 are not possible. Only reactions 11 and 13 are possible for our tests described in this dissertation. Cu_6Sn_5 is one of the products in reaction 13 but not the reactant, and the associated temperature is below the melting point of the eutectic Sn-Pb solder. Reaction 11 are possible for a liquid phase with a composition of 61Sn-39Pb which is different from solder materials used in this study.

Table B1: Reactions associated with Sn-Pb-Cu ternary system (Bolcavage et al., 1995; Shim et al., 1996; Fecht et al., 1989; NIST, 2012).

Reaction No.: Reaction	Phase	Mass % Cu	Mass % Pb	Mass % Sn
1: $L_1 + (Cu) \rightarrow L_2 + \text{beta}$ 760.2 °C	Liquid	63.80	12.15	24.05
	(Cu)	85.38	0	14.62
	Liquid	2.93	95.71	1.36
	(beta)	78.43	0	21.57
2: $L_1 + \text{beta} \rightarrow L_2 + \text{gamma}$ 732.0 °C	Liquid	59.50	11.14	29.36
	beta	75.15	0	24.85
	Liquid	2.34	95.32	2.34
	gamma	72.95	0	27.05
3: $L_1 + L_2 + \text{gamma} \rightarrow \text{Cu}_3\text{Sn}$ 675.5 °C	Liquid	44.59	12.47	42.94
	Liquid	1.98	88.56	9.46
	gamma	60.78	0	39.22
	Cu_3Sn	61.63	0	38.37
4: $L_2 + \text{gamma} + \text{Cu}_3\text{Sn} \rightarrow \text{Cu}_{10}\text{Sn}_3$ 640.1 °C	Liquid	1.10	96.05	2.85
	gamma	65.95	0	34.05
	Cu_3Sn	61.63	0	38.37
	$\text{Cu}_{10}\text{Sn}_3$	64.06	0	35.94
5: $L_2 + \text{gamma} + \text{Cu}_{10}\text{Sn}_3 \rightarrow \text{Cu}_{41}\text{Sn}_{11}$ 590.0 °C	Liquid	0.74	97.96	1.30
	gamma	68.56	0	31.44
	$\text{Cu}_{10}\text{Sn}_3$	64.06	0	35.94
	$\text{Cu}_{41}\text{Sn}_{11}$	66.56	0	33.44
6: $L_2 + \text{beta} \rightarrow (Cu) + \text{gamma}$ 585.9 °C	Liquid	0.80	98.60	0.60
	beta	76.12	0	23.88
	(Cu)	84.56	0	15.44
	gamma	73.94	0	26.06
7: $L_2 + \text{Cu}_{10}\text{Sn}_3 \rightarrow \text{Cu}_3\text{Sn} + \text{Cu}_{41}\text{Sn}_{11}$ 582.5 °C	Liquid	0.69	98.07	1.24
	$\text{Cu}_{10}\text{Sn}_3$	64.06	0	35.94
	Cu_3Sn	61.63	0	38.37
	$\text{Cu}_{41}\text{Sn}_{11}$	66.56	0	33.44
8: $L_2 + \text{gamma} \rightarrow (Cu) + \text{Cu}_{41}\text{Sn}_{11}$ 518.7 °C	Liquid	0.45	99.16	0.39
	gamma	72.71	0	27.29
	(Cu)	85.15	0	14.85
	$\text{Cu}_{41}\text{Sn}_{11}$	66.56	0	33.44
9: $L_2 + \text{Cu}_{41}\text{Sn}_{11} \rightarrow (Cu) + \text{Cu}_3\text{Sn}$ 348.1 °C	Liquid	0.08	99.87	0.05
	$\text{Cu}_{41}\text{Sn}_{11}$	66.56	0	33.44
	(Cu)	90.36	0	9.64
	Cu_3Sn	61.63	0	38.37
10: $L_2 + (Cu) \rightarrow \text{Cu}_3\text{Sn} + (\text{Pb})$ 326.2 °C	Liquid	0.06	99.90	0.04
	(Cu)	91.04	0	8.96
	Cu_3Sn	61.63	0	38.37
	(Pb)	0	99.97	0.03
11: $L_2 + \text{Cu}_6\text{Sn}_5 \rightarrow (\text{Pb}) + \text{Cu}_6\text{Sn}_5'$ 187.5 °C	Liquid	0.09	39.22	60.69
	Cu_6Sn_5	39.07	0	60.93
	(Pb)	0	81.72	18.28
	$\text{Cu}_6\text{Sn}_5'$	39.07	0	60.93
12: $L_2 + \text{Cu}_3\text{Sn} \rightarrow (\text{Pb}) + \text{Cu}_6\text{Sn}_5$ 277.9 °C	Liquid	0.04	80.83	19.13
	Cu_3Sn	61.63	0	38.37
	(Pb)	0	90.28	9.72
	$\text{Cu}_6\text{Sn}_5'$	39.07	0	60.93
13: $L_2 \rightarrow (\text{Pb}) + (\text{Sn}) + \text{Cu}_6\text{Sn}_5'$ 181.7 °C	Liquid	0.09	37.27	62.64
	(Pb)	0	81.23	18.77
	(Sn)	0	3.39	96.61
	$\text{Cu}_6\text{Sn}_5'$	39.07	0	60.93

Appendix C

Measurement of Cu_6Sn_5 Grains size and determination of groove angle β for IMC1

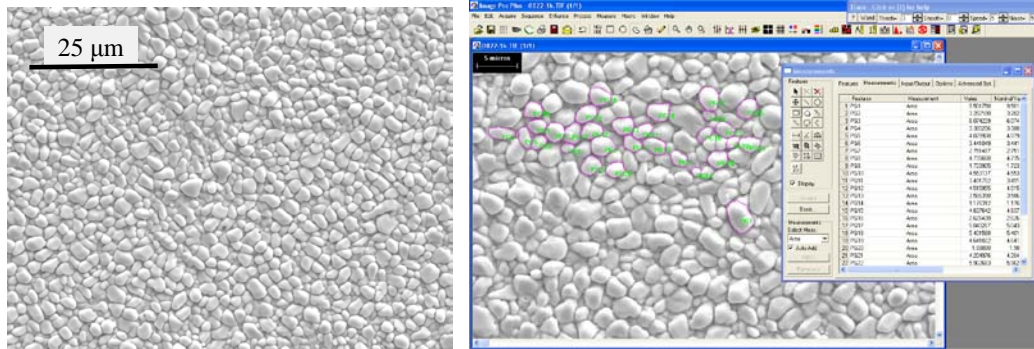


Figure C1: A SEM image indicating topographical features of IMC1 (left) and measuring process with Image Pro Plus software

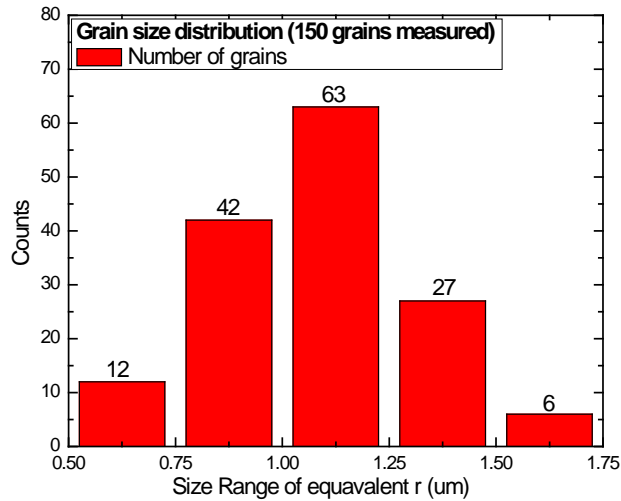


Figure C2: Grain size distribution for IMC1 according to measurement

Measurement was conducted at 5 different locations, with total 150 grains measured, on a SEM image (with magnification of $\times 1000$) of IMC1 surface. The image on which the measurement was conducted is with the size of about $115 \mu\text{m} \times 84 \mu\text{m}$. For each of those five locations 30 grains were measured. The average equivalent radius of

the grains is 1.09 μm with a standard deviation of 0.234 μm . Equivalent radius of 70% of measured grains falls in the range of 0.75 μm to 1.25 μm .

Table C1: Measured data for two IMC1 surfaces

	Measurement-1 (surface-1)	Measurement-2 (surface-2)
1	49 ^o	63 ^o
2	47 ^o	56 ^o
3	39 ^o	51 ^o
4	71 ^o	65 ^o
5	70 ^o	70 ^o
6	52 ^o	56 ^o
7	76 ^o	54 ^o
8	64 ^o	38 ^o
9	59 ^o	52 ^o
10	74 ^o	30 ^o
Average (each)	60 ^o	54 ^o
Average (all)	57 ^o \pm 12 ^o	

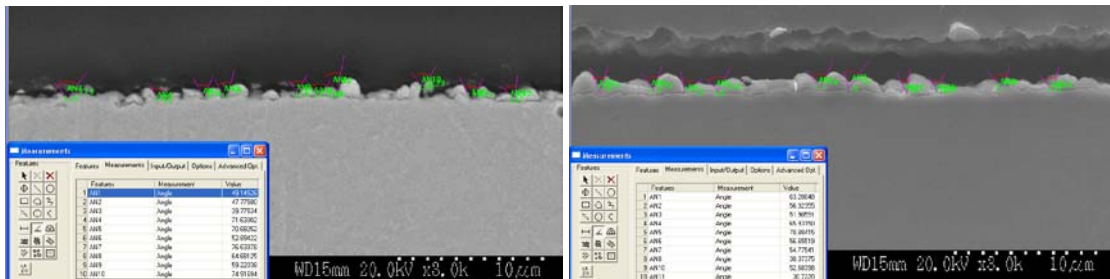


Figure C3: Measured data for IMC1 surface: measurement-1 for surface-1 (right) and measurement-2 for surface-2 (left)

The measurement of the groove angle is conducted to two IMC1 surfaces. The SEM pictures used for measurement are both with the magnification of $\times 3000$. The software used for measure is Image Pro Plus. For each pictures, 10 random cross sections of grooves will be measured. Therefore there are 20 measured values totally. Then the average of those 20 values will be the groove angle used for all IMC1 surfaces.

Appendix D

Non-Isothermal Spreading (Properties of liquid metals vs. Temperature Change)

Spreading process is associated with a temperature range of 30 °C:

For 63Sn37Pb: ~183 °C - ~213 °C

For 80Sn20Pb: ~200 °C - ~235 °C

For a Temperature range of ~195 °C to ~570 °C, Surface tension of SnPb alloy can be estimated as (Schwaneke et al., 1978; Howie and Hondros, 1982

$$\gamma = [\sim 510 - \sim 5 \times 10^{-2} T] \text{ mN / m} \quad (\text{D1})$$

So a change of temperature within a range of 30 °C may cause a change of around 0.3%, which can be negligible.

Density change for a 30 °C range is roughly approximated to be less than 1% (Schwaneke et al., 1978)

Viscosity change for a 30 °C range is also roughly estimated to be less than 5% based on the data reported by Thresh et al. (Thresh et al., 1970)

Appendix E

Definitions of Geometrical Parameters for Surface Roughness Characterization

Table E1, E2 and E3 summarize geometric parameters of the patterned surface (schematically presented in or related to Figures 4.7 and 4.8). Note that the fluid contact angle formed between liquid and the groove walls, and the curve of free liquid surface caused by surface tension are included in the calculation of the area and volume of molten metal present in an open triangular groove as indicated in Figure 4.8 (that impact is not considered in case of an individual merging zone).

It is assumed that there are M hexagons (M rows) in vertical direction and N hexagons (N columns) in horizontal direction, as indicated in Figure E1. Therefore the number of total number of hexagons on an IMC1 surface can be determined, as indicated in Table E1.

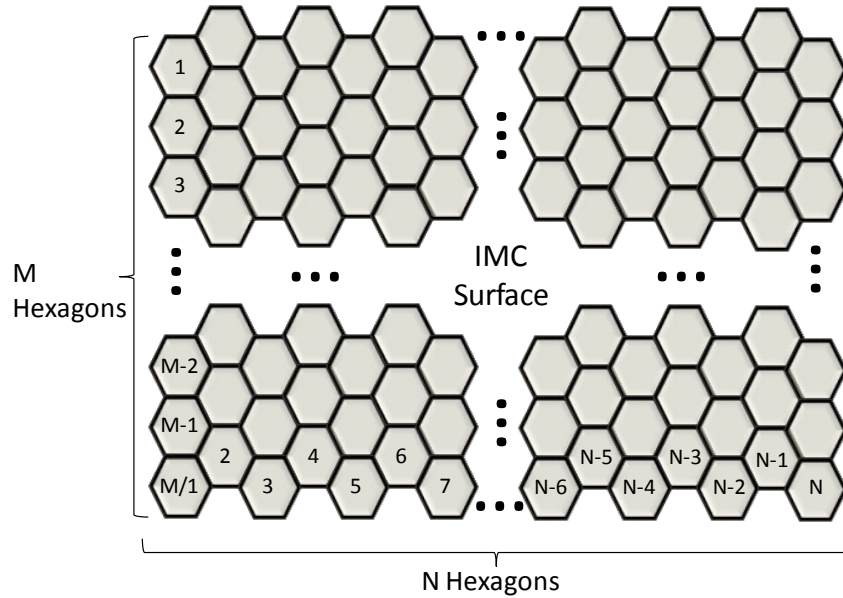


Figure E1: Configuration of IMC1 surface composed of regular hexagons

Table E1: Geometric length parameters for a simplified IMC1 surface

Geometric Parameter	Definition	Description
a	$a = 10^{-6} \text{ m}$	Length of the bottom edge of a hexagonal element
l_0	$l_0 = a(1 - (2\sqrt{3}/3)\sin(\beta/2))$	Length of the top edge of a hexagonal element
l_1	$l_1 = 10^{-6} \text{ m}$	Length of a lateral edge of a hexagonal element
l_2	$l_2 = 2l_1 \sin(\beta/2)$	Width of a single V-groove (top)
h_0	$h_0 = l_1 \cos(\beta/2)$	Height of a single V-groove
h	$h = \eta h_0$	Average height of molten solder in grooves (takes into account the filling factor)
L	$L = 10^{-2} \text{ m}$	Length of the side of IMC1 substrate
N_{hex}	$N_{hex} = M \times N \cong (L/\sqrt{3}) \times [L/(1.5a)]$	Total number of hexagonal elements on IMC1 substrate; M and N are number of rows and columns of hexagonal elements, see Figure E1.

Table E2: Geometric area parameters for a simplified IMC-1 surface

Geometric Parameter	Expression	Description
A_1	$A_1 = (3\sqrt{3}/2)l_0^2$	Area of the top surface of a hexagonal element
A_2	$A_2 = (a + l_0)l_1/2$	Area of one side of a hexagonal element

Table E3: Geometric volume parameters for a simplified IMC-1 surface

Geometric Parameter	Expression	Description
V_g	$V_g = (1/2)a^3 \sin \beta(1 - (4\sqrt{3}/9) \sin(\beta/2))$	Volume of a single v-groove
$V_{\eta g}$	$V_{\eta g} = A_\eta(\alpha, \theta)a(1 - 2\eta(\sqrt{3}/3) \sin(\beta/2)) + (\sqrt{3}/9)\eta^3 a^3 \sin \beta \sin(\beta/2)$	Actual volume of molten metal in a single v-groove if partially filled with average height ηh_0 (considering the influence of contact angle θ)
V_j	$V_j = (\sqrt{3}/3)l_1^3 (\sin(\beta/2))^2 \cos(\beta/2)$	Volume of a single joint; also the volume of molten metal in a single joint if it is fully filled (without considering the influence of contact angle θ)
$V_{\eta j}$	$V_{\eta j} = \eta^3 V_j$	Actual volume of molten metal in a single joint if partially filled with average height ηh_0 (without considering the influence of contact angle θ)
V_v	$V_v = N_g V_g + N_j V_j$ $N_g = (M - 1)N + (2M - 1)(N - 1)$ $N_j = 2(M - 1)(N - 1)$	Total volume of void space (porous part) on the IMC1 layer; M and N are defined in Figure E1
$V_{\eta v}$	$V_{\eta v} = N_g V_{\eta g} + N_j V_{\eta j}$	Total volume of molten metal on the IMC1 layer if all groove and joint zones are partially filled with height ηh_0
V_{imc}	$V_{imc} = A_s h_0$	Volume of the entire IMC1 surface as a porous medium
V_{mat}	$V_{mat} = A_i \delta_i$	Volume of initial source of material (volume of solid solder)

Appendix F

Analytical estimation of Permeability

A theoretical approach was reported by Hubbert (Hubbert, 1957). He considered that the permeability of a porous medium could be expressed as a function of the porosity, the surface area and volume of the porous domain. The experimental value will be verified a posteriori using Test-1 data and Equation (4.11) described in Chapter 4. Theoretically, the intrinsic permeability is to be calculated based only on topographic features of the IMC1 surface. We have used the method introduced in (Hubbert, 1957) assuming that the topographical features are represented by “hexagonal elements”. The expression of intrinsic permeability can be written as, (Hubbert, 1957)

$$k_{theor} = \frac{\varepsilon}{6} \left(\frac{2\varepsilon}{B} \right)^2 \quad (F1)$$

where ε is the porosity; B is the ratio of total surface area of voids throughout the porous medium to the total volume of the porous medium. With the specific geometric configuration of IMC1 the quantity B can be approximated as the ratio of the total surface area of hexagonal elements to the total volume of the IMC-1 layer which is V_{imc} as defined in Table E3, see Equation (F3) below.

Taking into account the geometric configuration as presented in Figure 4.8 (b) and (d), the total surface area of all hexagonal elements on IMC-1 surface, represented by A_t , can be expressed as

$$A_t = N_{hex} (A_1 + A_2) \quad (F2)$$

where N_{hex} is defined in Table A1; A_1 and A_2 are defined in Table D2.

Therefore B of Equation (F1) can be expressed as

$$B = A_t/V_{imc} \quad (F3)$$

The numerical value of B leads to the calculated value of theoretical intrinsic permeability as $k_{\text{theor}} = 1.364 \times 10^{-14} \text{ m}^2$ (see Table 3), with the porosity determined by Equation (F4), see below.

Brief Description of Tortuosity

IMC1 surface is simplified as having a regular topographic structure resulting in a axisymmetric 2-D porous medium. Based on a geometric simplification, the total available porous volume V_v throughout the IMC1 layer and the total volume of the IMC1 layer V_{imc} can be defined and calculated, as given in Table E3 in Appendix E. Therefore the surface porosity of IMC1 is defined as follows (De Wiest et al., 1969; Scheidegger, 1974).

$$\varepsilon = \frac{V_v}{V_{imc}} \quad (F4)$$

For the given geometry, $\varepsilon = 0.453$, note that the surface porosity represents a quantity based only on a specific topography of the surface (IMC1). The tortuosity τ of a porous medium can be determined as a function of porosity ε . The relation is derived by Boving and Grathwohl (Boving and Grathwohl, 2001).

$$\tau = \varepsilon^{-1.2} \quad (\text{F5})$$

The numerical value of tortuosity for the determined porosity is in this case $\tau = 2.590$. Note that the similar process assisted with AFM analysis was implemented to IMC0 and IMC3 in order to determine the porosity and tortuosity, see Chapter 3 and 5.

Equation (4.11) was used to verify the estimated permeability k from experimental data of Test 1 listed in Chapter 4. Note that intrinsic permeability is a constant property for the same type of porous medium, which means the permeability verified with data for Test 1 should be applicable as long as the substrate is not changed (i.e., IMC1).

With the estimated surface tension and viscosity shown in Table 4.5, data of Test 1 (Figure 4.1; time and corresponding spreading front locations) within the time span between 1 second and 26 seconds, Equation (4.11) leads to an average intrinsic permeability of $k_{\text{exp}}=1.497 \times 10^{-15} \text{ m}^2$ with a standard deviation of $2.381 \times 10^{-15} \text{ m}^2$. Note that the theoretically determined permeability and experimentally verified permeability are within the same order of magnitude, and differ only by a factor of ~ 1.1 .

Appendix G

Filling Conditions (A filling factor η)

The grooves may apparently be variably filled along the spreading radius, i.e., one may expect that the grooves near the source may be fully filled, and grooves further within the domain of spreading may be filled only partially. To assess the level of the filling of the grooves by liquid metal, an experimental observation was conducted.

The wetted surface of one of the samples examined by optical microscopy is studied in detail. Figure F1 shows that the complete domain of the rough portion of the surface is not completely flooded with molten solder, but all the surface alterations (i.e., grooves between the grains) are visited by liquid phase. That is, molten metal does not wet the rough surface completely. That is, certain regions of the free surface are not flooded (i.e., the high-spot islands' locations). This observation (verified to be present in other cases) proves that the geometric features (grooves and merging zones) are not necessarily fully filled with molten material throughout the wetted domain. Therefore, it is necessary to make an assumption that the grooves are only partially filled with an average height $h = \eta h_0$, where η is the filling factor, the ratio of (i) the average actual height of the molten material in the grooves and the merging zones, and (ii) the height of a groove and a merging zone.

Data taken from Test-1 were used for calculating the filling factor η . The residue at the source location at the end of the spreading is assumed to be small enough to be neglected. Therefore, the initial state of the molten metal to spread and its final state (within the surface alterations), as the spreading is without chemical reaction (Appendix B), must obey the conservation of mass principle.

$$\frac{A_f}{A_s} V_{\eta^v} = V_{mat} \quad (G1)$$

where A_f is the final spreading area of the source material, listed in Table 4.2; A_s is the total area of IMC1 substrate, listed in Table 4.2; V_{η^v} is the total available porous volume for molten solder on IMC1 substrate, see Table E3; V_{mat} is the initial volume of the source material, see Table E3.

With data/information from Table 4.1, the numerical value of filling factor can be calculated from Equation (G1), (Note that this equation involves η , see Appendix F) $\eta = 0.76$. The average mass of the molten material in all the grooves is assumed to be 76% of the mass needed to fill the grooves completely. This result is fully consistent with our observations. Note that axisymmetric intermediate circular features in Figure G1 represent the solidification artifacts not further considered within the scope of this work (i.e., only liquid phase of the process of spreading is considered).

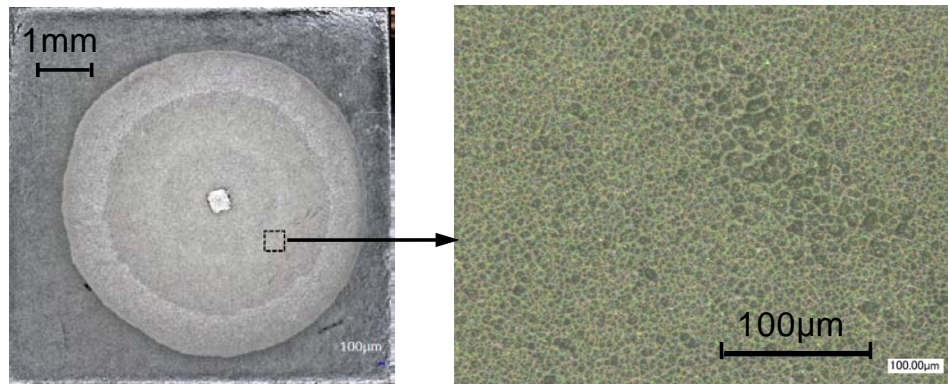


Figure G1: General view of Pb-Sn eutectic over IMC layer and details of emphasized spot with magnification of 1000×

Appendix H

Raw Kinetics Data for all Spreading Tests Studied in this Dissertation

Table H1 contains the raw kinetics data for capillary rise of organic liquids over IMC0 surface studied in Chapter 3. Note that the data sets included are associated with Figure 3.8 in Chapter 3. (Note that: 1. z represents the spreading distance of liquids; 2. no data value is presented if blank.)

Table H1: kinetics data for capillary rise of organic liquids over IMC0 surface

Methanol		Dodecane		Tetradecane		2-Propanol		2-Butanol	
Time (s)	z (mm)	Time (s)	z (mm)	Time (s)	z (mm)	Time (s)	z (mm)	Time (s)	z (mm)
0	0.00	0	0.00	0	0.00	0	0.00	0	0.00
0.5	1.20	1	0.95	1	0.61	0.5	0.60	0.5	0.32
1	1.65	2	1.47	2	1.00	1	0.92	1	0.60
1.5	1.90	3	1.84	3	1.33	1.5	1.14	1.5	0.70
2	2.25	4	2.21	4	1.61	2	1.35	2	0.81
2.5	2.40	5	2.47	5	1.89	2.5	1.46	3	1.03
3	2.80	8	3.21	6	2.06	3	1.62	4	1.19
3.5	2.95	11	3.63	7	2.17	3.5	1.73	5	1.30
4	3.15	15	4.16	8	2.44	4	1.78	6	1.41
4.5	3.35	20	4.79	10	2.83	4.5	2.00	7	1.57
5	3.55	25	5.35	12	3.06	5.5	2.27	8	1.68
5.5	3.70	35	6.26	14	3.33	6.5	2.43	10	1.89
6	3.90	45	7.16	16	3.50	7.5	2.60	12	2.11
6.5	4.05	55	7.63	18	3.72	8.5	2.65	14	2.32
7	4.25	65	8.58	20	3.94	9.5	2.81	16	2.43
7.5	4.35	75	8.95	25	4.33	10.5	3.08	18	2.65
8	4.45	85	9.37	30	4.83	12.5	3.14	20	2.76
8.5	4.55	100	10.21	35	5.06	14.5	3.51	23	2.97
9	4.70	115	10.95	45	5.67	16.5	3.78	26	3.08
9.5	4.90	130	11.74	55	6.33	18.5	3.89	30	3.35
10	4.95	145	12.32	65	6.89	20.5	4.11	34	3.57
10.5	5.00	160	12.74	75	7.33	22.5	4.22	38	3.68
11	5.20	175	13.21	85	7.83	25	4.43	42	3.89
11.5	5.25	190	13.53	100	8.28	27.5	4.76	46	4.05
12	5.35	205	14.16	115	8.89	31.5	4.81	50	4.27
12.5	5.50			130	9.22	35.5	5.24	54	4.49
13	5.65			145	9.61	40.5	5.41	60	4.76
13.5	5.70			165	10.22	45.5	5.68	66	4.81
14	5.85			185	10.89	50.5	6.00	72	4.92

Table H1: kinetics data for capillary rise of organic liquids over IMC0 surface (Continued)									
Time (s)	z (mm)	Time (s)	z (mm)	Time (s)	z (mm)	Time (s)	z (mm)	Time (s)	z (mm)
14.5	5.90			205	11.33	58.5	6.38	82	5.19
15	6.05			225	11.72	66.5	6.60	92	5.51
15.5	6.15			245	12.17	74.5	6.81	102	5.73
16	6.20			265	12.61	82.5	7.03	112	5.89
17	6.45					90.5	7.19	122	6.16
18	6.60								
19	6.85								
20	6.90								
21	7.00								
22	7.20								
23	7.30								
24	7.60								
25	7.70								
26	7.75								
27	7.98								
28	8.05								
29	8.10								
30	8.10								
31	8.25								
32	8.50								
33	8.55								
34	8.75								
35	8.75								
36	8.80								
37	9.00								
38	9.05								
39	9.20								
40	9.30								
41	9.35								
42	9.40								
43	9.45								
44	9.50								
45	9.55								
46	9.75								

Table H2 contains the raw kinetics data for imbibition of molten solders over IMC1 surface studied in Chapter 4. Note that the data sets included are associated with Figure 4.6 in Chapter 4. (Note that: 1. r represents the spreading radius; 2. no data value is presented if blank.)

Table H2: Raw kinetics data for imbibition of molten solders over IMC1 surface

63Sn-37Pb				80Sn-20Pb			
Test-1		Test-2		Test-3		Test-4	
Time (s)	<i>r</i> (mm)	Time (s)	<i>r</i> (mm)	Time (s)	<i>r</i> (mm)	Time (s)	<i>r</i> (mm)
0.00	0.19	0.00	0.20	0.00	0.27	0.00	0.30
0.18	0.24	0.46	0.62	0.23	0.28	0.23	0.32
0.23	0.28	0.92	0.92	0.46	0.34	0.46	0.39
0.28	0.34	1.38	1.12	0.69	0.41	0.69	0.50
0.32	0.37	1.83	1.29	0.92	0.53	0.92	0.60
0.37	0.43	2.29	1.45	1.15	0.66	1.15	0.73
0.41	0.49	2.75	1.57	1.38	0.77	1.38	0.85
0.46	0.54	3.21	1.67	1.60	0.91	1.60	0.95
0.50	0.60	3.67	1.76	1.83	1.02	1.83	1.04
0.55	0.64	4.13	1.87	2.06	1.14	2.06	1.13
0.60	0.69	4.58	1.95	2.29	1.26	2.29	1.22
0.64	0.77	5.50	2.10	2.52	1.34	2.52	1.31
0.69	0.80	6.42	2.23	2.75	1.44	2.75	1.37
0.73	0.84	7.33	2.37	2.98	1.52	2.98	1.45
0.78	0.88	8.25	2.47	3.21	1.60	3.21	1.53
0.83	0.91	9.17	2.57	3.44	1.67	3.44	1.59
0.87	0.93	10.08	2.66	3.67	1.73	3.67	1.65
0.92	0.97	11.00	2.73	3.90	1.80	3.90	1.71
0.96	0.99	11.92	2.80	4.13	1.87	4.13	1.76
1.01	1.02	12.83	2.86	4.35	1.92	4.35	1.82
1.05	1.06	13.75	2.90	4.58	1.98	4.58	1.87
1.10	1.08	14.67	2.94	4.81	2.02	4.81	1.92
1.15	1.10	15.58	2.98	5.04	2.07	5.04	1.96
1.19	1.13	16.50	3.01	5.27	2.12	5.27	2.01
1.24	1.15	17.42	3.03	5.50	2.16	5.50	2.04
1.28	1.17	18.33	3.05	5.73	2.20	5.73	2.09
1.33	1.19	19.25	3.06	5.96	2.24	5.96	2.13
1.38	1.21	20.17	3.07	6.19	2.28	6.19	2.16
1.42	1.25	21.08	3.09	6.42	2.31	6.42	2.20
1.47	1.26	22.00	3.10	6.65	2.35	6.65	2.24
1.51	1.28	22.92	3.11	6.88	2.39	6.88	2.27
1.56	1.29	23.83	3.11	7.10	2.42	7.10	2.30
1.60	1.31	24.75	3.13	7.33	2.45	7.33	2.33
1.65	1.33	25.67	3.12	7.56	2.48	7.56	2.36
1.70	1.34	26.58	3.13	7.79	2.51	7.79	2.39
1.74	1.37	27.50	3.13	8.02	2.54	8.02	2.42
1.79	1.39	28.42	3.14	8.25	2.56	8.25	2.45
1.83	1.40	29.33	3.15	8.48	2.59	8.48	2.47
1.88	1.42			8.71	2.61	8.71	2.50
1.93	1.43			8.94	2.64	8.94	2.53
1.97	1.44			9.17	2.66	9.17	2.55
2.02	1.46			9.40	2.68	9.40	2.58
2.06	1.47			9.63	2.70	9.63	2.60

Table H2: Raw kinetics data for imbibition of molten solders over IMC1 surface (continued)							
Time (s)	<i>r</i> (mm)	Time (s)	<i>r</i> (mm)	Time (s)	<i>r</i> (mm)	Time (s)	<i>r</i> (mm)
2.11	1.48			9.85	2.72	9.85	2.63
2.15	1.51			10.08	2.74	10.08	2.65
2.20	1.53			10.54	2.78	10.31	2.68
2.25	1.53			11.00	2.81	10.54	2.69
2.29	1.55			11.46	2.84	10.77	2.72
2.34	1.56			11.92	2.87	11.00	2.74
2.38	1.57			12.38	2.89	11.23	2.76
2.43	1.58			12.83	2.92	11.46	2.78
2.48	1.59			13.29	2.94	11.69	2.81
2.52	1.62			13.75	2.96	11.92	2.82
2.57	1.65			14.21	2.98	12.15	2.83
2.70	1.66			14.67	3.00	12.38	2.84
2.75	1.67			15.13	3.02	12.60	2.86
2.80	1.68			16.04	3.05	12.83	2.87
2.84	1.69			16.96	3.08	13.06	2.88
2.89	1.70			17.88	3.11	13.29	2.90
2.93	1.72			18.79	3.13	13.52	2.91
2.98	1.74			19.71	3.15	13.75	2.92
3.03	1.74			20.63	3.17	13.98	2.93
3.07	1.75			21.54	3.18	14.21	2.94
3.12	1.76			22.46	3.20	14.44	2.95
3.16	1.78			23.38	3.21	14.67	2.97
3.21	1.78			24.29	3.22	14.90	2.98
3.25	1.79			25.21	3.24	15.13	2.99
3.30	1.82			26.13	3.25	15.58	3.01
3.35	1.82			27.04	3.26	16.04	3.02
3.39	1.83			27.96	3.28	16.50	3.04
3.44	1.84			28.88	3.29	16.96	3.06
3.48	1.85			29.79	3.31	17.42	3.08
3.53	1.86					17.88	3.09
3.58	1.87					18.33	3.10
3.62	1.88					18.79	3.12
4.08	1.99					19.25	3.13
4.54	2.08					20.17	3.16
5.00	2.16					21.08	3.18
5.45	2.23					22.00	3.20
5.91	2.29					22.92	3.22
6.37	2.35					23.83	3.24
6.83	2.39					24.75	3.26
7.29	2.44					25.67	3.28
7.75	2.48					26.58	3.30
8.20	2.52					27.50	3.31
8.66	2.55					28.42	3.32
9.12	2.58					29.33	3.34
9.58	2.62					30.25	3.35
10.04	2.64						

Table H2: Raw kinetics data for imbibition of molten solders over IMC1 surface (continued)							
Time (s)	<i>r</i> (mm)	Time (s)	<i>r</i> (mm)	Time (s)	<i>r</i> (mm)	Time (s)	<i>r</i> (mm)
10.50	2.66						
10.95	2.69						
11.41	2.71						
11.87	2.73						
12.33	2.75						
12.79	2.78						
13.25	2.79						
13.70	2.81						
14.16	2.82						
14.62	2.83						
15.08	2.84						
15.54	2.86						
16.00	2.87						
16.45	2.86						
16.91	2.88						
17.37	2.88						
17.83	2.89						
18.29	2.90						
18.75	2.90						
19.66	2.90						
20.12	2.91						
20.58	2.92						
21.04	2.92						
21.50	2.92						
21.95	2.93						
22.41	2.93						
22.87	2.94						
23.33	2.95						
23.79	2.95						
24.25	2.95						
24.70	2.96						

Table H3 contains the raw kinetics data for imbibition of molten solders over IMC3 surface presented in Figure 5.9 in Chapter 5. (Note: 1. *x*, *y* represent the preferential and short-axis spreading radius, respectively; 2. no data presented if blank.)

Table H3: Raw kinetics data for imbibition of molten solders over IMC3 surface

63Sn-37Pb					
Test1			Test2		
Time (s)	x (mm)	y (mm)	Time (s)	x (mm)	y (mm)
0.00	0.26	0.22	0.00	0.18	0.14
0.51	0.94	0.73	0.51	0.78	0.52
1.01	1.37	0.95	1.01	1.12	0.69
1.51	1.68	1.13	1.51	1.37	0.83
2.02	1.86	1.22	2.02	1.50	0.98
2.52	2.08	1.32	2.52	1.64	1.03
3.03	2.23	1.42	3.03	1.75	1.08
3.53	2.32	1.45	3.53	1.83	1.12
4.03	2.42	1.55	4.03	1.88	1.15
4.54	2.50	1.60	4.54	1.96	1.26
5.04	2.54	1.62	5.04	2.00	1.28
6.05	2.69	1.73	6.05	2.09	1.31
7.06	2.74	1.80	7.06	2.18	1.35
8.07	2.86	1.88	8.07	2.27	1.41
9.08	2.96	1.92	9.08	2.30	1.46
10.08	3.02	1.96	10.08	2.34	1.50
11.09	3.09	2.01	11.09	2.40	1.55
13.11	3.18	2.09	12.10	2.46	1.59
15.13	3.28	2.14	14.12	2.57	1.64
17.14	3.37	2.22	16.13	2.61	1.69
19.16	3.42	2.27	18.15	2.71	1.78
23.19	3.55	2.36	20.17	2.75	1.86
27.18	3.63	2.44	24.16	2.84	1.94
31.12	3.71	2.52	28.14	2.93	2.00
35.11	3.77	2.55	32.13	3.00	2.09
39.10	3.87	2.64	36.12	3.10	2.15
47.12	3.99	2.71	40.11	3.12	2.18
55.14	4.05	2.76	44.09	3.15	2.24
63.16	4.05	2.80	48.08	3.19	2.30
71.18	4.06	2.86	54.09	3.25	2.34
79.18	4.06	2.86	60.09	3.25	2.34
87.20	4.07	2.86	66.09	3.27	2.36
			72.10	3.27	2.37
			78.10	3.27	2.38

Table H4 contains the raw kinetics data for reactive wetting of molten AgCuTi filler over polished and rough surfaces studied in Chapter 6. Data sets included are

associated with Figure 6.5 in Chapter 6. (Note that: 1. r represents the spreading radius;
 2. no data value is presented if blank.

Table H4: Raw kinetics data for reactive wetting of molten AgCuTi filler over polished
 and rough surfaces

Polished TiAl surface						Rough TiAl surface					
test1		test2		test3		test1		test2		test3	
Time (s)	r (mm)	Time (s)	r (mm)	Time (s)	r (mm)	Time (s)	r (mm)	Time (s)	r (mm)	Time (s)	r (mm)
0	0.92	0	0.93	0	0.90	0	0.91	0	0.93	0	0.91
15	0.92	20	0.93	15	0.90	15	0.92	10	0.93	10	0.91
25	0.92	40	0.91	25	0.90	25	0.92	20	0.93	20	0.91
35	0.92	50	0.89	30	0.90	30	0.91	30	0.93	30	0.91
40	0.92	60	0.89	35	0.89	35	0.92	40	0.93	40	0.91
45	0.92	70	0.89	40	0.90	40	0.91	50	0.92	50	0.91
50	0.91	80	0.88	45	0.89	45	0.91	60	0.92	60	0.90
55	0.91	85	0.90	50	0.89	50	0.92	70	0.91	70	0.90
65	0.91	90	0.92	55	0.88	55	0.92	80	0.91	80	0.90
75	0.91	95	0.96	60	0.88	60	0.91	90	0.90	90	0.89
85	0.89	100	1.00	65	0.88	65	0.91	95	0.94	95	0.91
90	0.88	105	1.05	70	0.88	75	0.92	100	0.97	100	0.94
92	0.91	110	1.09	75	0.88	85	0.92	105	1.00	105	0.96
94	0.93	115	1.13	80	0.88	95	0.91	107	1.03	107	0.98
95	0.96	120	1.17	85	0.87	100	0.91	110	1.05	112	1.00
97	0.97	125	1.21	90	0.87	105	0.90	112	1.07	115	1.01
100	1.00	130	1.25	95	0.86	110	0.93	115	1.10	117	1.03
102	1.01	135	1.27	100	0.87	115	0.97	117	1.12	120	1.05
105	1.05	140	1.27	103	0.88	120	0.99	120	1.14	123	1.07
107	1.07	145	1.28	105	0.90	123	1.02	123	1.18	125	1.10
110	1.10	150	1.28	108	0.93	125	1.06	125	1.21	130	1.12
112	1.12	155	1.28	110	0.94	128	1.08	130	1.23	135	1.15
115	1.14	160	1.28	113	0.99	130	1.11	135	1.24	140	1.18
117	1.15	170	1.29	115	1.02	135	1.14	140	1.26	145	1.21
120	1.18	180	1.30	118	1.05	140	1.17	145	1.27	150	1.22
122	1.20	190	1.30	120	1.08	142	1.18	150	1.28	160	1.23
125	1.21	200	1.30	125	1.11	145	1.21	160	1.29	170	1.24
127	1.23	210	1.30	128	1.15	148	1.23	170	1.30	180	1.26
130	1.25	220	1.30	130	1.17	150	1.26	180	1.30	190	1.27
132	1.26	230	1.30	133	1.19	155	1.27	190	1.30	200	1.28
135	1.27	240	1.30	135	1.22	160	1.28	200	1.30	210	1.28
140	1.28	250	1.30	138	1.24	165	1.29	210	1.30	220	1.28
145	1.28	260	1.30	140	1.25	170	1.30	220	1.30	230	1.28
155	1.29	270	1.30	145	1.26	175	1.30	230	1.30	240	1.29

Time (s)	r (mm)	Time (s)	r (mm)	Time (s)	r (mm)	Time (s)	r (mm)	Time (s)	r (mm)	Time (s)	r (mm)
165	1.30	280	1.30	150	1.26	185	1.31	240	1.30	250	1.29
180	1.31	290	1.30	155	1.27	195	1.31	250	1.30	270	1.29
185	1.31	300	1.30	160	1.27	205	1.31	270	1.31	290	1.29
190	1.31	310	1.30	165	1.27	215	1.31	290	1.31	310	1.29
195	1.31	320	1.30	170	1.27	225	1.31	310	1.31	330	1.29
205	1.32	330	1.30	175	1.27	235	1.31	330	1.31	350	1.29
215	1.32	340	1.30	195	1.27	245	1.31	350	1.31	360	1.29
225	1.32	350	1.30	215	1.27	255	1.32	360	1.31		
235	1.32			235	1.27	265	1.32				
245	1.32			255	1.28	275	1.32				
255	1.32			275	1.28	285	1.32				
265	1.32			295	1.28	295	1.32				
275	1.32			315	1.28	305	1.32				
285	1.32			335	1.28	285	1.32				
295	1.32			355	1.28	295	1.32				
305	1.32			365	1.28	305	1.32				
315	1.32			375	1.28						
325	1.32										
335	1.32										
345	1.32										

Table H5 contains the raw kinetics data for imbibition of molten solders over IMC2 surface presented in Figure 5.6 in Chapter 5. (Note: 1. x, y represent the preferential and short-axis spreading radius, respectively; 2. no data presented if blank.)

Table H5: Raw kinetics data for imbibition of molten solders over IMC2 surface

Time (s)	x (mm)	y (mm)	Time (s)	x (mm)	y (mm)	Time (s)	x (mm)	y (mm)
0.00	0.26	0.22	6.05	2.69	1.73	27.18	3.63	2.44
0.51	0.94	0.73	7.06	2.74	1.80	31.12	3.71	2.52
1.01	1.37	0.95	8.07	2.86	1.88	35.11	3.77	2.55
1.51	1.68	1.13	9.08	2.96	1.92	39.10	3.87	2.64
2.02	1.86	1.22	10.08	3.02	1.96	47.12	3.99	2.71
2.52	2.08	1.32	11.09	3.09	2.01	55.14	4.05	2.76
3.03	2.23	1.42	13.11	3.18	2.09	63.16	4.05	2.80
3.53	2.32	1.45	15.13	3.28	2.14	71.18	4.06	2.86
4.03	2.42	1.55	17.14	3.37	2.22	79.18	4.06	2.86
4.54	2.50	1.60	19.16	3.42	2.27	87.20	4.07	2.86
5.04	2.54	1.62	23.19	3.55	2.36			

Appendix I

Symbolism

Symbol	Description and unit	Symbol	Description and unit
a	molecule Size, [m]	α, β	groove angle, [deg]
A	area, [m ²] A ₁ , A ₂ , A _s , A _i , A _f , A _t are defined in Table 4.1 and Appendix E	γ	Surface Tension subscripts SG, SL, LG are defined in Figure 2.3
$A^*(\alpha, \theta)$	geometrical parameter, [-]	δ	distance, [m]
B_o	Bond number, [-]	ε	porosity, [-]
E	surface energy, [J]	η	filling factor, [-]
F	force, [N] Subscript γ, μ are defined in the text	θ	contact Angle, [deg] superscript *, subscripts E, SG, SL, LG, 1, 2, C, A, P and F are defined in the text
f	fractional area, [-] subscript 1 and 2 are defined in the text	κ^{-1}	capillary length, [m]
g	gravity acceleration, [m/s ²]	μ	Viscosity [kg/s·m]
$G(\alpha, \theta)$	geometrical parameter, [-]	π	mathematical constant
		ρ	mass density, [kg/m ³]
	specific height, [m] subscript 0, 1, 2 and m are defined in text	τ	tortuosity, [-]
h		φ	slip coefficient [-]
	permeability scalar, [m ²]; constant, [-]		
k		Φ	true contact angle, [deg] subscript 1, 2 and 3 are defined in the text
$k(T)$	thermal Energy, [eV]		
$K(\alpha, \theta)$	geometrical parameter, [-]		
\mathbf{K}	permeability tensor, [m ²]		
l	specific length subscript c, s, 0 are defined in text		
P	Pressure Subscripts h, A,		
r	surface roughness, [-]; circular radius, [m]; spreading distance, [m]		
R	spreading distance, [m]; with subscript “ds”, spreading ratio, [-]		
R_a	surface roughness		
R_c	radius of curvature, [m]		
t	time, [s]		
U	cohesion Energy, [eV]; Velocity [m/s]		
u, v	specific velocity scalar, [m/s]		
\mathbf{v}	specific velocity vector, [m/s]		
V	Volume, [m ³] V _g , V _{ηg} , V _j , V _{ηj} , V _v , V _{ηv} , V _{imc} , V _{mat} are defined in Table E3.		
x, y, z, ξ	rectangular coordinates, [m]		

REFERENCES

- Apel-Paz, M. and Marmur, A. (1999). "Spreading of liquids on rough surfaces." *Colloids and Surfaces a-Physicochemical and Engineering Aspects* 146(1-3): 273-279.
- Appel, F., Paul, J. D. H. and Oehring, M. (2011). *Gamma titanium aluminide alloys : science and technology*. Weinheim, Germany, Wiley-VCH.
- Barnes, G. and Gentle, I. (2011). *Interfacial science : an introduction*. Oxford ; New York, Oxford University Press.
- Bejan, A. (2004). *Convection heat transfer*. Hoboken, N.J. ; [Chichester], Wiley.
- Benhassine, M., Saiz, E., Tomsia, A. P. and De Coninck, J. (2010). "Role of substrate commensurability on non-reactive wetting kinetics of liquid metals." *Acta Materialia* 58(6): 2068-2078.
- Biance, A. L., Clanet, C. and Quere, D. (2004). "First steps in the spreading of a liquid droplet." *Physical Review E* 69(1).
- Bico, J., Thiele, U. and Quere, D. (2002). "Wetting of textured surfaces." *Colloids and Surfaces a-Physicochemical and Engineering Aspects* 206(1-3): 41-46.
- Bico, J., Tordeux, C. and Quere, D. (2001). "Rough wetting." *Europhysics Letters* 55(2): 214-220.
- Bircumshaw, L. L. (1931). "The surface tension of liquid metals. Part IV. The surface tension of mercury." *Philosophical Magazine* 12(77): 596-602.
- Blow, M. L., Kusumaatmaja, H. and Yeomans, J. M. (2009). "Imbibition through an array of triangular posts." *Journal of Physics-Condensed Matter* 21(46).
- Bolcavage, C.R. Kao, S.-L. Chen and Y.A. Chang, "Thermodynamic Calculation of Phase Stability Between Copper and Lead-Indium Solder", *Applications of Thermodynamics in Synthesis and Processing of Materials*, Eds. P. Nash and B. Sundman, TMS, Warrendale, PA, 1995, 102-140
- Bonn, D., Eggers, J., Indekeu, J., Meunier, J. and Rolley, E. (2009). "Wetting and spreading." *Reviews of Modern Physics* 81(2): 739-805.
- Bonn, D. and Ross, D. (2001). "Wetting transitions." *Reports on Progress in Physics* 64(9): 1085-1163.
- Bouche, K., Barbier, F. and Coulet, A. (1998). "Intermetallic compound layer growth between solid iron and molten aluminium." *Materials Science and Engineering a-Structural Materials Properties Microstructure and Processing* 249(1-2): 167-175.
- Boving, T. B. and Grathwohl, P. (2001). "Tracer diffusion coefficients in sedimentary rocks: correlation to porosity and hydraulic conductivity." *Journal of Contaminant Hydrology* 53(1-2): 85-100.
- Braun, R. J., Murray, B. T., Boettinger, W. J. and Mcfadden, G. B. (1995). "Lubrication Theory for Reactive Spreading of a Thin Drop." *Physics of Fluids* 7(8): 1797-1810.
- Brazing handbook. (1991). Miami, Fla., American Welding Society.
- Brochardwyart, F., Hervet, H., Redon, C. and Rondelez, F. (1991). "Spreading of Heavy Droplets .1. Theory." *Journal of Colloid and Interface Science* 142(2): 518-527.
- Calderon, N. R., Voytovych, R., Narciso, J. and Eustathopoulos, N. (2009). "Wetting dynamics versus interfacial reactivity of AlSi alloys on carbon", *Journal of Materials Science*. 45: 2150-2156

- Campbell, C. E. and Boettinger, W. J. (2000). "Transient liquid-phase bonding in the Ni-Al-B system." *Metallurgical and Materials Transactions a-Physical Metallurgy and Materials Science* 31(11): 2835-2847.
- Cassie, A. B. D. and Baxter, S. (1944). "Wettability of porous surfaces." *Transactions of the Faraday Society* 40: 0546-0550.
- Cazabat, A. M. and Stuart, M. A. C. (1986). "Dynamics of Wetting - Effects of Surface-Roughness." *Journal of Physical Chemistry* 90(22): 5845-5849.
- Chada, S., Laub, W., Fournelle, R. A. and Shangguan, D. (1999). "An improved numerical method for predicting intermetallic layer thickness developed during the formation of solder joints on Cu substrates." *Journal of Electronic Materials* 28(11): 1194-1202.
- Chandra, D., Yang, S., Soshinsky, A. A. and Gambogi, R. J. (2009). "Biomimetic Ultrathin Whitening by Capillary-Force-Induced Random Clustering of Hydrogel Micropillar Arrays." *Acs Applied Materials & Interfaces* 1(8): 1698-1704.
- Chen, Y. K., Melvin, L. S., Rodriguez, S., Bell, D. and Weislogel, M. M. (2009). "Capillary driven flow in micro scale surface structures." *Microelectronic Engineering* 86(4-6): 1317-1320.
- Clarke, A. N., Megehee, M. M. and Wilson, D. J. (1993). "Soil Clean up by Insitu Aeration .12. Effect of Departures from Darcys-Law on Soil Vapor Extraction." *Separation Science and Technology* 28(9): 1671-1690.
- Clemens, H. and Kestler, H. (2000). "Processing and applications of intermetallic gamma-TiAl-based alloys." *Advanced Engineering Materials* 2(9): 551-570.
- Courbin, L., Bird, J. C., Reyssat, M. and Stone, H. A. (2009). "Dynamics of wetting: from inertial spreading to viscous imbibition." *Journal of Physics-Condensed Matter* 21(46).
- Courbin, L., Bird, J. C., Reyssat, M. and Stone, H. A. (2009). "Dynamics of wetting: from inertial spreading to viscous imbibition." *Journal of Physics-Condensed Matter* 21(46).
- Courbin, L., Denieul, E., Dressaire, E., Roper, M., Ajdari, A. and Stone, H. A. (2007). "Imbibition by polygonal spreading on microdecorated surfaces." *Nature Materials* 6(9): 661-664.
- De Wiest, R. J. M., Bear, J. and Institute in Hydrology for College Teachers Princeton University 1965. (1969). *Flow through porous media*. New York,, Academic Press.
- Defay, R. and Prigogine, I. (1966). *Surface tension and adsorption*. New York,, Wiley.
- Degennes, P. G. (1985). "Wetting - Statics and Dynamics." *Reviews of Modern Physics* 57(3): 827-863.
- Dezellus, O., Hodaj, F. and Eustathopoulos, N. (2002). "Chemical reaction-limited spreading: the triple line velocity versus contact angle relation." *Acta Materialia* 50(19): 4741-4753.
- Dezellus, O., Hodaj, F. and Eustathopoulos, N. (2003). "Progress in modelling of chemical-reaction limited wetting." *Journal of the European Ceramic Society* 23(15): 2797-2803.
- Dodge, F. T. (1988). "The Spreading of Liquid Droplets on Solid-Surfaces." *Journal of Colloid and Interface Science* 121(1): 154-160.

- Drevet, B., Landry, K., Vikner, P. and Eustathopoulos, N. (1996). "Influence of substrate orientation on wetting kinetics in reactive metal/ceramic systems." *Scripta Materialia* 35(11): 1265-1270.
- Durian, D. J. and Franck, C. (1987). "Continued Exploration of the Wetting Phase-Diagram." *Physical Review B* 36(13): 7307-7310.
- Durian, D. J. and Franck, C. (1987). "Wetting Phenomena of Binary-Liquid Mixtures on Chemically Altered Substrates." *Physical Review Letters* 59(5): 555-558.
- Dussan, E. B. and Davis, S. H. (1974). "Motion of a Fluid-Fluid Interface Along a Solid-Surface." *Journal of Fluid Mechanics* 65(Aug12): 71-&.
- Dussan, V. E. B. (1976). "Difference between a Bounding Surface and a Material Surface." *Journal of Fluid Mechanics* 75(Jun25): 609-623.
- Dussaud, A. D., Adler, P. M. and Lips, A. (2003). "Liquid transport in the networked microchannels of the skin surface." *Langmuir* 19(18): 7341-7345.
- Ejima, T., Sato, Y., Yamamura, T., Hayashi, A. and Yamazaki, T. (1990). "Viscosity Measurement of Pb-Sn Binary Melts and the Effect of Melting and Solidification on the Measurement." *Journal of the Japan Institute of Metals* 54(9): 1005-1012.
- Epstein, N. (1989). "On Tortuosity and the Tortuosity Factor in Flow and Diffusion through Porous-Media." *Chemical Engineering Science* 44(3): 777-779.
- Espie, L., Drevet, B. and Eustathopoulos, N. (1994). "Experimental-Study of the Influence of Interfacial Energies and Reactivity on Wetting in Metal-Oxide Systems." *Metallurgical and Materials Transactions a-Physical Metallurgy and Materials Science* 25(3): 599-605.
- Espie, L., Drevet, B. and Eustathopoulos, N. (1994). "Experimental-Study of the Influence of Interfacial Energies and Reactivity on Wetting in Metal-Oxide Systems." *Metallurgical and Materials Transactions a-Physical Metallurgy and Materials Science* 25(3): 599-605.
- Eustathopoulos, N. (1998). "Dynamics of wetting in reactive metal ceramic systems." *Acta Materialia* 46(7): 2319-2327.
- Eustathopoulos, N. (2005). "Progress in understanding and modeling reactive wetting of metals on ceramics." *Current Opinion in Solid State & Materials Science* 9(4-5): 152-160.
- Eustathopoulos, N., Garandet, J. P. and Drevet, B. (1998). "Influence of reactive solute transport on spreading kinetics of alloy droplets on ceramic surfaces." *Philosophical Transactions of the Royal Society of London Series a-Mathematical Physical and Engineering Sciences* 356(1739): 871-884.
- Eustathopoulos, N., Nicholas, M. G. and Drevet, B. a. (1999). *Wettability at high temperatures*. Amsterdam ; Oxford, Pergamon.
- Fecht, H. J., Zhang, M. X., Chang, Y. A. and Perepezko, J. H. (1989). "Metastable Phase-Equilibria in the Lead-Tin Alloy System .2. Thermodynamic Modeling." *Metallurgical Transactions a-Physical Metallurgy and Materials Science* 20(5): 795-803.
- Fetter, C. W. (1994). *Applied hydrogeology*. New York, Macmillan College ; New York ; Oxford : Maxwell Macmillan International.
- Gale, W. F., Shen, Y., Fergus, J. W. and Wen, X. (1999). "Anomalous wetting of Ti-48 at.% Al-2 at.% Cr-2 at.% Nb substrates by liquid copper." *Journal of Materials Research* 14(10): 3889-3894.

- Gennes, P.-G. d., Brochard-Wyart, F. and Quéré, D. (2004). *Capillarity and wetting phenomena : drops, bubbles, pearls, waves*. New York, Springer.
- Hay, K. M., Dragila, M. I. and Liburdy, J. (2008). "Theoretical model for the wetting of a rough surface." *Journal of Colloid and Interface Science* 325(2): 472-477.
- Horcas, I., Fernandez, R., Gomez-Rodriguez, J. M., Colchero, J., Gomez-Herrero, J. and Baro, A. M. (2007). "WSXM: A software for scanning probe microscopy and a tool for nanotechnology." *Review of Scientific Instruments* 78(1).
- Howie, F. H. and Hondros, E. D. (1982). "The Surface-Tension of Tin Lead Alloys in Contact with Fluxes." *Journal of Materials Science* 17(5): 1434-1440.
- Hubbert, M. K. and Willis, D. G. (1957). "Mechanics of Hydraulic Fracturing." *Transactions of the American Institute of Mining and Metallurgical Engineers* 210(6): 153-163.
- Huh, C. and Scriven, L. E. (1971). "Hydrodynamic Model of Steady Movement of a Solid/Liquid/Fluid Contact Line." *Journal of Colloid and Interface Science* 35(1): 85-&.
- Ishino, C., Okumura, K. and Quere, D. (2004). "Wetting transitions on rough surfaces." *Europhysics Letters* 68(3): 419-425.
- Ishino, C., Reyssat, M., Reyssat, E., Okumura, K. and Quere, D. (2007). "Wicking within forests of micropillars." *Epl* 79(5).
- Johnson, R. E. and Dettre, R. H. (1964). "Contact Angle Hysteresis .3. Study of an Idealized Heterogeneous Surface." *Journal of Physical Chemistry* 68(7): 1744-&.
- Kernaghan, M. (1931). "Surface tension of mercury." *Physical Review* 37(8): 990-997.
- Kumar, G. and Prabhu, K. N. (2007). "Review of non-reactive and reactive wetting of liquids on surfaces." *Advances in Colloid and Interface Science* 133(2): 61-89.
- Kumar, G. and Prabhu, K. N. (2007). "Review of non-reactive and reactive wetting of liquids on surfaces." *Advances in Colloid and Interface Science* 133(2): 61-89.
- Lafuma, A. and Quere, D. (2003). "Superhydrophobic states." *Nature Materials* 2(7): 457-460.
- Landesberg, J. (2004). "Dean's Handbook of Organic Chemistry. 2nd ed. (Book)." *Choice: Current Reviews for Academic Libraries* 41(8): 1503-1503.
- Landry, K. and Eustathopoulos, N. (1996). "Dynamics of wetting in reactive metal/ceramic systems: Linear spreading." *Acta Materialia* 44(10): 3923-3932.
- Landry, K., Kalogeropoulou, S., Eustathopoulos, N., Naidich, Y. and Krasovsky, V. (1996). "Characteristic contact angles in the aluminium/vitreous carbon system." *Scripta Materialia* 34(6): 841-846.
- Laplace, P. S. (1805). "Traité de Mécanique céleste", Volume 4, Book 8, Courcier, Paris
- Lee, S. J., Wu, S. K. and Lin, R. Y. (1998). "Infrared joining of TiAl intermetallics using Ti-15Cu-15Ni foil - I. The microstructure morphologies of joint interfaces." *Acta Materialia* 46(4): 1283-1295.
- Li, Y. L., He, P. and Feng, J. C. (2006). "Interface structure and mechanical properties of the TiAl/42CrMo steel joint vacuum brazed with Ag-Cu/Ti/Ag-Cu filler metal." *Scripta Materialia* 55(2): 171-174.
- Li, Y. L., Liu, W., He, P. and Sekulic, D.P. (2012). "Reactive wetting of AgCuTi filler metal on the TiAl-based alloy substrate.", *Applied Surface Science*, 259: 343-348
- Liu, W., Li, Y. L., Cai, Y. G. and Sekulic, D. P. (2011). "Capillary Rise of Liquids over a Microstructured Solid Surface." *Langmuir* 27(23): 14260-14266.

- Liu, W., Lu, L. B., Li, Y. L., Cai, Y. G. and Sekulic, D. P. (2012). "Preferential spreading of molten metal over an anisotropically microstructured surface." *Epl* 97(4).
- Liu, W. and Sekulic, D. P. (2011). "Capillary Driven Molten Metal Flow over Topographically Complex Substrates." *Langmuir* 27(11): 6720-6730.
- Liu, W. and Sekulic, D. P. (2011). "Anisotropic spreading of liquid metal on an intermetallic surface." *Theoretical and Applied Mechanics*, 38(4): 365-377.
- Lopez, J., Miller, C. A. and Ruckenstein, E. (1976). "Spreading Kinetics of Liquid-Drops on Solids." *Journal of Colloid and Interface Science* 56(3): 460-468.
- Lucas, R. (1918). "The time law of the capillary rise of liquids." *Kolloid-Zeitschrift* 23(1): 15-22.
- Mann, J. A., Romero, L., Rye, R. R. and Yost, F. G. (1995). "Flow of Simple Liquids down Narrow-V Grooves." *Physical Review E* 52(4): 3967-3972.
- Middleman, S. (1995). *Modeling axisymmetric flows : dynamics of films, jets, and drops.* San Diego, Academic Press.
- Moon, K. W., BOettinger, W. J., Williams, M. E., Josell, D., Murray, B. T., Carter, W. C. and Handwerker, C. A. (1996). "Dynamic aspects of wetting balance tests." *Journal of Electronic Packaging* 118(3): 174-183.
- Moser, Z., Gasior, W., Pstrus, J. and Debski, A. (2008). "Wettability Studies of Pb-Free Soldering Materials." *International Journal of Thermophysics* 29(6): 1974-1986.
- Nalwa, H. S. (2001). *Advances in surface science.* San Diego, Academic Press.
- Nguyen, J., Geiger, D., Rooney, D. and Shanguan, D. (2008). "Solder joint characteristics and reliability of lead-free area array packages assembled at various tin-lead soldering process conditions." *Ieee Transactions on Electronics Packaging Manufacturing* 31(3): 227-239.
- NIST, <http://www.metallurgy.nist.gov/phase/>, August, 10th, 2012
- Noda, T. (1998). "Application of cast gamma TiAl for automobiles." *Intermetallics* 6(7-8): 709-713.
- Ogihara, H., Xie, J., Okagaki, J. and Saji, T. (2012). "Simple Method for Preparing Superhydrophobic Paper: Spray-Deposited Hydrophobic Silica Nanoparticle Coatings Exhibit High Water-Repellency and Transparency." *Langmuir* 28(10): 4605-4608.
- Prakash, M., Quere, D. and Bush, J. W. M. (2008). "Surface tension transport of prey by feeding shorebirds: The capillary ratchet." *Science* 320(5878): 931-934.
- Quere, D. (2002). "Rough ideas on wetting." *Physica a-Statistical Mechanics and Its Applications* 313(1-2): 32-46.
- Quere, D. (2008). "Wetting and roughness." *Annual Review of Materials Research* 38: 71-99.
- Quere, D. and Reyssat, M. (2008). "Non-adhesive lotus and other hydrophobic materials." *Philosophical Transactions of the Royal Society a-Mathematical Physical and Engineering Sciences* 366(1870): 1539-1556.
- Rico-Guevara, A. and Rubega, M. A. (2011). "The hummingbird tongue is a fluid trap, not a capillary tube." *Proceedings of the National Academy of Sciences of the United States of America* 108(23): 9356-9360.
- Romero, L. A. and Yost, F. G. (1996). "Flow in an open channel capillary." *Journal of Fluid Mechanics* 322: 109-129.

- Roulin, M., Luster, J. W., Karadeniz, G. and Mortensen, A. (1999). "Strength and structure of furnace-brazed joints between aluminum and stainless steel." *Welding Journal* 78(5): 151s-155s.
- Rowlinson, J. S. and Widom, B. (1982). *Molecular theory of capillarity*, Clarendon.
- Rye, R. R., Mann, J. A. and Yost, F. G. (1996). "The flow of liquids in surface grooves." *Langmuir* 12(2): 555-565.
- Rye, R. R., Yost, F. G. and O'Toole, E. J. (1998). "Capillary flow in irregular surface grooves." *Langmuir* 14(14): 3937-3943.
- Saiz, E., Cannon, R. M. and Tomsia, A. P. (2000). "Reactive spreading: Adsorption, ridging and compound formation." *Acta Materialia* 48(18-19): 4449-4462.
- Scheidegger, A. E. (1974). *The physics of flow through porous media*. Toronto ; Buffalo N.Y., University of Toronto Press.
- Schmiedgen, M., Graat, P. C. J., Baretzky, B. and Mittemeijer, E. J. (2002). "The initial stages of oxidation of gamma-TiAl: an X-ray photoelectron study." *Thin Solid Films* 415(1-2): 114-122.
- Seveno, D., Vaillant, A., Rioboo, R., Adao, H., Conti, J. and De Coninck, J. (2009). "Dynamics of Wetting Revisited." *Langmuir* 25(22): 13034-13044.
- Shapiro, A. E. and Sekulic, D. P. (2008). "A new approach to quantitative evaluation of a design for brazed structures." *Welding Journal* 87(1): 1S-10S.
- Shen, Y., Gale, W. F., Fergus, J. W. and Wen, X. (2001). "Wettability of preoxidised TiAl substrates by liquid aluminium, copper, and silver." *Materials Science and Technology* 17(10): 1293-1298.
- Shibuichi, S., Onda, T., Satoh, N. and Tsujii, K. (1996). "Super water-repellent surfaces resulting from fractal structure." *Journal of Physical Chemistry* 100(50): 19512-19517.
- Shim, J. H., Oh, C. S., Lee, B. J. and Lee, D. N. (1996). "Thermodynamic assessment of the Cu-Sn system." *Zeitschrift Fur Metallkunde* 87(3): 205-212.
- Shiue, R. K., Wu, S. K. and Chen, S. Y. (2003). "Infrared brazing of TiAl intermetallic using BA9-8 braze alloy." *Acta Materialia* 51(7): 1991-2004.
- Shiue, R. K., Wu, S. K. and Chen, S. Y. (2004). "Infrared brazing of TiAl intermetallic using pure silver." *Intermetallics* 12(7-9): 929-936.
- Smith, C. S. (1948). "Grains, Phases, and Interfaces - an Interpretation of Microstructure." *Transactions of the American Institute of Mining and Metallurgical Engineers* 175: 15-51.
- Steel, R. G. D. and Torrie, J. H. (1960). *Principles and procedures of statistics, with special reference to the biological sciences*. New York, McGraw-Hill.
- Suh, J. O., Tu, K. N., Lutsenko, G. V. and Gusak, A. M. (2008). "Size distribution and morphology of Cu₆Sn₅ scallops in wetting reaction between molten solder and copper." *Acta Materialia* 56(5): 1075-1083.
- Suh, J. O., Tu, K. N., Lutsenko, G. V. and Gusak, A. M. (2008). "Size distribution and morphology of Cu₆Sn₅ scallops in wetting reaction between molten solder and copper." *Acta Materialia* 56(5): 1075-1083.
- Suh, J. O., Tu, K. N. and Tamura, N. (2007). "Preferred orientation relationship between Cu₆Sn₅ scallop-type grains and Cu substrate in reactions between molten Sn-based solders and Cu." *Journal of Applied Physics* 102(6).

- Suh, K., Shin, J. H., Seo, S. J. and Bae, B. S. (2008). "Er(3+) luminescence and cooperative upconversion in Er(x)Y(2-x)SiO(5) nanocrystal aggregates fabricated using Si nanowires." *Applied Physics Letters* 92(12).
- Tanner, L. H. (1979). "Spreading of Silicone Oil Drops on Horizontal Surfaces." *Journal of Physics D-Applied Physics* 12(9): 1473-&.
- Tu, K. N. (2007). *Solder joint technology : materials, properties, and reliability*. New York, Springer.
- Tuteja, A., Choi, W., Ma, M. L., Mabry, J. M., Mazzella, S. A., Rutledge, G. C., McKinley, G. H. and Cohen, R. E. (2007). "Designing superoleophobic surfaces." *Science* 318(5856): 1618-1622.
- Vianco, P. T., American Welding Society. and American Welding Society. Committee on Brazing and Soldering. (1999). *Soldering handbook*. Miami, Fla., American Welding Society.
- Villars, P., Prince, A. and Okamoto, H. (1995). *Handbook of ternary alloy phase diagrams*. [Materials Park, Ohio], ASM International.
- Vrij, A. (1966). "Possible Mechanism for Spontaneous Rupture of Thin Free Liquid Films." *Discussions of the Faraday Society*(42): 23-&.
- Wang, H. Q., Gao, F., Ma, X. and Qian, Y. Y. (2006). "Reactive wetting of solders on Cu and Cu₆Sn₅/Cu₃Sn/Cu substrates using wetting balance." *Scripta Materialia* 55(9): 823-826.
- Wang, L. L., Zhang, X. T., Li, B., Sun, P. P., Yang, J. K., Xu, H. Y. and Liu, Y. C. (2011). "Superhydrophobic and Ultraviolet-Blocking Cotton Textiles." *ACS Applied Materials & Interfaces* 3(4): 1277-1281.
- Warren, J. A., Boettinger, W. J. and Roosen, A. R. (1998). "Modeling reactive wetting." *Acta Materialia* 46(9): 3247-3264.
- Washburn, E. W. (1921). "The dynamics of capillary flow." *Physical Review* 17(3): 273-283.
- Webb, E. B., Hoyt, J. J. and Grest, G. S. (2005). "High temperature-wetting: Insights from atomistic simulations." *Current Opinion in Solid State & Materials Science* 9(4-5): 174-180.
- Webb, W. B. and Grest, G. S. (2002). "Molecular dynamics simulations of reactive wetting." *Scripta Materialia* 47(6): 393-398.
- Weislogel, M. M. and Lichter, S. (1996). "A spreading drop in an interior corner: Theory and experiment." *Microgravity Science and Technology* 9(3): 175-184.
- Weislogel, M. M. and Lichter, S. (1998). "Capillary flow in an interior corner." *Journal of Fluid Mechanics* 373: 349-378.
- Wenzel, R. N. (1936). "Resistance of solid surfaces to wetting by water." *Industrial and Engineering Chemistry* 28: 988-994.
- White, D. W. G. (1971). "Surface Tension and Solidification Behaviour of Zinc and Cadmium." *Journal of the Institute of Metals* 99(Nsep): 287-&.
- Yamaguchi, M., Inui, H. and Ito, K. (2000). "High-temperature structural intermetallics." *Acta Materialia* 48(1): 307-322.
- Yang, S. H., Tian, Y. H. and Wang, C. Q. (2010). "Investigation on Sn grain number and crystal orientation in the Sn-Ag-Cu/Cu solder joints of different sizes." *Journal of Materials Science-Materials in Electronics* 21(11): 1174-1180.

- Yin, L., Murray, B. T. and Singler, T. J. (2006). "Dissolutive wetting in the Bi-Sn system." *Acta Materialia* 54(13): 3561-3574.
- Yost, F. G., Rye, R. R. and Mann, J. A. (1997). "Solder wetting kinetics in narrow V-grooves." *Acta Materialia* 45(12): 5337-5345.
- Zhao, H. (2005). "Transport phenomena involving molten clad during aluminum brazing process." PhD Dissertation, Mechanical Engineering, University of Kentucky.
- Zhao, H. and Sekulic, D. P. (2008). "Wetting kinetics of a hypo-eutectic Al-Si system." *Materials Letters* 62(16): 2241-2244.
- Zhao, H., Wang, H. Q., Sekulic, D. P. and Qian, Y. Y. (2009). "Spreading Kinetics of Liquid Solders over an Intermetallic Solid Surface. Part 1: Eutectic Lead Solder." *Journal of Electronic Materials* 38(9): 1838-1845.
- Zhao, H., Wang, H. Q., Sekulic, D. P. and Qian, Y. Y. (2009). "Spreading Kinetics of Liquid Solders over an Intermetallic Solid Surface. Part 2: Lead-Free Solders." *Journal of Electronic Materials* 38(9): 1846-1854.
- Zou, H. F., Yang, H. J. and Zhang, Z. F. (2008). "Morphologies, orientation relationships and evolution of Cu_6Sn_5 grains formed between molten Sn and Cu single crystals." *Acta Materialia* 56(11): 2649-2662.
- Zuruzi, A. S., Chiu, C. H., Lahiri, S. K. and Tu, K. N. (1999). "Roughness evolution of Cu_6Sn_5 intermetallic during soldering." *Journal of Applied Physics* 86(9): 4916-4921.

VITA

Name

Wen Liu

Date and Place of Birth

June 15th, 1984
Wuhan, Hubei, China

Education

B.S. in Mechanical Science and Engineering (09/2003 – 07/2007), Huazhong University of Science and Technology, Wuhan, Hubei, China

Experience

- Research Assistant (08/2007 – 12/2012), Brazing Research Laboratory, Institute for Sustainable Manufacturing, University of Kentucky
- Teaching Assistant (08/2007 – 05/2010), Department of Mechanical Engineering, University of Kentucky

Award

Outstanding Graduate Student in Mechanical Engineering, University of Kentucky, 2012

Peer-Reviewed Journal Publications

1. Wen Liu and Dusan P. Sekulic, Capillary Driven Molten Metal Flow over Topographically Complex Surface, *Langmuir*, 27(11), pp 6720-6730, (2011)
2. Wen Liu, Yulong Li, Yuguang Cai and Dusan P. Sekulic, Capillary Rise of Liquids over a Microstructured Solid Surface, *Langmuir*, 27(23), pp 14260-14266, (2011)
3. Wen Liu and Dusan P. Sekulic, Anisotropic Spreading of Liquid Metal on an Intermetallic Surface, *Theoretical and Applied Mechanics*, 38(4), pp 365-377, (2011) (Invited paper)
4. Wen Liu, Lingbo Lu, Yulong Li, Yuguang Cai and Dusan P. Sekulic, Preferential Spreading of Molten Metal on an Anisotropic Microstructured Surface, *EPL*, 97, 46003, (2012)
5. Yulong Li, Wen Liu, Yang Jin, Hua Zhang, Yan Feng, Ultrasonic embedding of nickel-coated fiber Bragg grating in aluminum and associated sensing characteristics, *Optical Fiber Technology*, 18, pp 7-13 (2012)
6. Yulong Li, Wen Liu, Peng He and Dusan P. Sekulic, Reactive wetting of AgCuTi filler metal on the TiAl-based alloy substrate, *Applied Surface Science*, 259, pp 343-348, (2012)
7. Yulong Li, Wen Liu, Peng He and Dusan P. Sekulic, Dissolution of TiAl alloy during a high temperature brazing, submitted to *Scripta Materialia*, (2012)

Peer-Reviewed Conference Proceedings

1. W. Liu and D. P. Sekulic (2012) Controlled Imbibition of Molten Metal on a Micro Structured Rough surface, 9th International Conference on Heat Transfer, Fluid Mechanics and Thermodynamics, Malta, 2012
2. W. Liu, D. Busbaher, Y. Li, D. P. Sekulic (2012) Homogeneous and heterogeneous Mo-Ni fillers doped with nanoparticles, International Brazing and Soldering Conference, Las Vegas, 2012
3. D. Busbaher, W. Liu and D.P. Sekulic (2012) Mechanical Properties of Nanoparticles Reinforced Mo-Ni Braze for a Dispenser Cathode Application, 2012 IEEE International Vacuum Electronics Conference, IVEC 2012, 2012
4. Y. Li, W. Liu, D. P. Sekulic (2012) Mechanical Response and Fracture Behavior of the TiAl/Steel Brazed Joint, International Brazing and Soldering Conference, Las Vegas, 2012
5. C-N Yu, D. Hawksworth, W. Liu, D. P. Sekulic (2012) Al brazing under severe alterations of the background atmosphere: A new vs. traditional brazing sheet, International Brazing and Soldering Conference, Las Vegas, 2012
6. M. Chen, H. Zhao, W. Liu, D. P. Sekulic (2012) Wettability of a Cu-nanoparticle-reinforced solder matrix paste composite, International Brazing and Soldering Conference, Las Vegas, 2012
7. D. Busbaher, W. Liu, David Mocher, D.P. Sekulic (2011) High Temperature Brazing of Porous Tungsten with Nano Structured Mo-Ni for a Dispenser Cathode Application, 2011 IEEE International Vacuum Electronics Conference, IVEC-2011, p 323-324, 2011
8. D. Busbaher, W. Liu and D.P. Sekulic (2010) High Temperature Brazing Using Nano-Particles Doped Filler Metal for Dispenser Cathode Applications, 2010 IEEE International Vacuum Electronics Conference, IVEC 2010, p 151-152, 2010
9. D. Busbaher, W. Liu and D.P. Sekulic (2010) High Temperature Brazing of Mo/Mo-Re with a Nano-Composite Mo-Ni Filler, DVS-Berichte, Vol 263, pp 211-214, ISMN 978-3-87155-589-3.
10. M. Chen, H. Zhao, W. Liu and D.P. Sekulic, (2009) Spreading of Nano Composites of Liquid Metals, 2nd. Int. Congress of the SS of Mechanics, Palic, Edited by T. Atanackovic, D. Spasic, and S. Simic, CD Proceedings (ISBN 978-86-7892-173-5).
11. D.P. Sekulic, Y. M. Dakhoul, H. Zhao, W. Liu (2009) Aluminum Foam Compact Heat Exchanger: Brazing Technology Development vs. Thermal Performance, Cellular Metals for Structural and Functional Applications, Edited by G. Stephani and B. Kieback, CELMET 2008, Fraunhofer, IFAM Dresden, 2009.
12. Sekulic, D.P. Zhao, H., W. Liu (2008) A Thermodynamic Metric for Process Quality Assessment in Manufacturing: Pb vs. Pb-free Solders Spreading Case Study, IEEE International Symposium on Electronics and the Environment, 2008, ISEE